Riccardo Matera

Novel Ultrasound Doppler Methods for Blood Flow Characterization

UNIVERSITÀ DEGLI STUDI FIRENZE

DINFO
DIPARTIMENTO DI INGEGNERIA DELL'INFORMAZIONE

DOTTORATO DI RICERCA IN

Tecnologie Elettroniche per l'Ingegneria dell'Informazione

CICLO XXVIII

COORDINATORE Prof. Piero Tortoli

Novel Ultrasound Doppler Methods for Blood Flow Characterization

ING-INF/01 Elettronica

<table>
<tr><td>**Dottorando**</td><td>**Tutor**</td></tr>
<tr><td>Dott. Matera Riccardo</td><td>Prof. Ricci Stefano</td></tr>
</table>

Anni 2012/2015

UNIVERSITÀ DEGLI STUDI FIRENZE

DOTTORATO DI RICERCA IN

Tecnologie Elettroniche per l'Ingegneria dell'Informazione

CICLO XXVIII

COORDINATORE Prof. Piero Tortoli

Novel Ultrasound Doppler Methods for Blood Flow Characterization

ING-INF/01 Elettronica

Dottorando	**Tutore**
Dott. Matera Riccardo	Prof. Ricci Stefano

_____   _____

Coordinatore
Prof. Tortoli Piero

_____

Anni 2012/2015

CONTENTS

Chapter 5
Novel Method Extension

Chapter 6
Peak Velocity Detection through Vector Doppler

INTRODUZIONE

Le patologie a carico dell'apparato cardiovascolare sono da annoverare tra le principali cause di decesso in Europa ed in Nord America. In molti casi tali malattie progrediscono in maniera asintomatica fino al verificarsi di fenomeni di particolare gravità, quali ictus o infarti, che possono risultare invalidanti, o addirittura mortali. In quest'ottica, la diagnosi precoce riveste un'importanza fondamentale nella prevenzione delle suddette patologie.

Un ruolo di primo ordine nel panorama degli strumenti diagnostici per la caratterizzazione del flusso sanguigno nei diversi distretti dell'apparato cardiocircolatorio è sicuramente svolto dalle tecniche Doppler ad ultrasuoni. Lo sviluppo e la diffusione in ambito clinico-medico che tali tecniche hanno subito nel corso dei decenni sono stati tali da farle diventare uno standard nel campo della medicina cardiovascolare. Il loro successo deriva dalla possibilità di ottenere, in modo non invasivo, affidabile ed economico, la diagnosi precoce di diverse malattie a carico dell'apparato cardiovascolare, quali insufficienza cardiaca, stenosi e deformazioni dei vasi sanguigni.

È questo il contesto in cui si inserisce la presente tesi di dottorato, il cui obiettivo è stato quello di sviluppare nuovi metodi Doppler ad ultrasuoni per la caratterizzazione del flusso sanguigno ai fini diagnostici. Le fasi sperimentali hanno previsto l'utilizzo dello scanner ad ultrasuoni ULA-OP, sistema di ricerca avanzato che offre agli sviluppatori grande libertà in termini di gestione e controllo di ogni sua parte, dalla trasmissione dei segnali all'elaborazione degli echi ricevuti. Il lavoro, che è stato svolto all'interno dell'MSD Lab (*Microelectronic System Design Laboratory*) situato presso il Dipartimento di Ingegneria dell'Informazione (DINFO) dell'Università degli Studi di Firenze, si è articolato su quattro fasi distinte.

Uno dei parametri che caratterizzano il flusso ematico è la portata volumetrica, che per la sua valutazione richiede la conoscenza sia della distribuzione di velocità all'interno di una sezione di vaso sia dell'area

della stessa sezione. Un'accurata valutazione di entrambe non può prescindere dal considerare i movimenti delle pareti arteriose e le complesse configurazioni di flusso che si instaurano all'interno delle stesse arterie. Poiché l'utilizzo delle tecniche di indagine ad ultrasuoni standard difficilmente fornisce tali informazioni, in questa tesi viene presentato un nuovo metodo per la misura della portata volumetrica, basato sulla misura simultanea del profilo di velocità e della posizione delle pareti del vaso. Il profilo di velocità è ottenuto attraverso un'analisi spettrale del segnale retroddifuso dai globuli rossi basata su una tecnica *multigate*, secondo la quale si misura il segnale Doppler in centinaia di posizioni consecutive allineate lungo la linea di indagine. La posizione delle pareti è invece individuata sull'immagine B-Mode attraverso un algoritmo di *wall-tracking* che sfrutta un *edge-detector* basato sull'operatore statistico *First Order Absolute Moment* (FOAM). Questi argomenti sono descritti all'interno del Capitolo 2.

In seconda battuta è stato considerato uno strumento largamente utilizzato nella pratica diagnostica: il sonogramma, che descrive l'andamento temporale del flusso ad una determinata profondità nel vaso, ottenuto attraverso un'analisi spettrale analoga a quella che porta alla realizzazione del profilo di velocità. L'informazione sul flusso fornita dal sonogramma è solitamente combinata con quella morfologica, secondo una modalità di presentazione di tipo duplex (B-Mode e analisi spettrale). Tuttavia, questa strategia d'indagine presenta lo svantaggio di essere caratterizzata da un frame rate di poche decine di immagini per secondo. Considerando l'elevata accelerazione che il cuore imprime al sangue nel picco sistolico (la velocità sanguigna all'interno della carotide comune può variare da 0 a 1m/s anche in meno di 20ms) la risoluzione temporale della modalità duplex risulta insufficiente ad una descrizione completa del flusso.

Al fine di migliorare la risoluzione temporale è stato quindi studiato l'utilizzo di stimatori spettrali non convenzionali che producono la stima della densità spettrale di potenza utilizzando un numero di campioni notevolmente inferiore rispetto a quelli necessari alla classica FFT. Tale studio ha portato all'implementazione dell'algoritmo di analisi spettrale

basato su questi stimatori su un DSP fixed-point TMS320C6455-EP™ presente a bordo dello scanner ad ultrasuoni ULA-OP. Questa parte del lavoro è contenuta all'interno del Capitolo 3.

Un altro parametro caratterizzante il flusso ematico è la sua massima velocità, usata dai medici per diagnosticare il grado di stenosi all'interno di un vaso e decidere sull'opportunità o meno di intervenire chirurgicamente. La misura della velocità di picco del sangue è però caratterizzata dall'incertezza su quale sia la frequenza appartenente allo spettro Doppler che ad essa corrisponde. Nel corso degli anni sono stati diversi e vari i metodi proposti per determinare questa frequenza, ma spesso si tratta di tecniche euristiche che non si basano su modelli fisico/matematici e che pertanto producono una stima di questa frequenza che risulta essere dipendente dal rumore del segnale Doppler e dal *broadening* spettrale.

In questo lavoro di tesi è presentato un modello matematico per lo spettro del segnale Doppler retrodiffuso dai globuli rossi che fornisce un valore preciso per la frequenza Doppler relativa alla velocità di picco del flusso ematico. La sperimentazione effettuata ha messo in evidenza i buoni risultati che il metodo produce considerando delle ipotesi di lavoro ideali quali la completa illuminazione di flussi parabolici. La ricerca si è comunque mossa verso la generalizzazione di tale modello, considerando flussi non parabolici e non completamente illuminati, in modo tale da riprodurre delle condizioni di lavoro più realistiche. Il nuovo approccio è stato implementato in un set-up sperimentale basato sulla trasmissione di onde piane, usando una sonda ad *array* lineare. I capitoli 4 e 5 riportano tali argomenti di ricerca.

L'estensione del modello, pur fornendo uno strumento deterministico per l'individuazione della frequenza Doppler relativa alla velocità di picco del flusso ematico, non consente ancora di superare il problema della conoscenza dell'angolo Doppler, una delle maggiori cause d'errore nelle stime di velocità con tecniche Doppler ad ultrasuoni. Infatti, quando l'angolo Doppler non è noto, può essere valutata la sola proiezione del vettore velocità lungo la direzione del fascio acustico. Inoltre, una poco

accurata determinazione dell'angolo Doppler produce un errore il cui effetto è maggiore per angoli prossimi a 90°. Questa condizione tipicamente si verifica nelle indagini sulla carotide, dove la sonda è posizionata parallelamente al vaso e l'angolo Doppler è determinato dalle limitate capacità di *steering* della sonda. L'implementazione in una configurazione di tipo vettoriale del metodo esteso fornisce invece misure di velocità di picco che risultano indipendenti dalla conoscenza dell'angolo Doppler. In particolare lo scanner ULA-OP è stato configurato in maniera tale che un'apertura centrale di una sonda ad *array* lineare trasmetta un'onda piana mentre due aperture laterali, simmetricamente posizionate rispetto al centro della sonda, ricevano il segnale retrodiffuso dai globuli rossi lungo due diverse direzioni. L'implementazione e la sperimentazione di questa tecnica è argomentata all'interno del Capitolo 6.

INTRODUCTION

Cardiovascular diseases are among the leading causes of death in Europe and North America. In many cases, these diseases progress without symptoms until the occurrence of phenomena of particular seriousness, such as stroke or heart attack, which can be disabling, or even fatal. From this perspective, early diagnosis is crucial in the prevention of these diseases.

Doppler ultrasound techniques play a leading role in the panorama of diagnostic tools for the characterization of blood flow in different districts of the cardiovascular system. The development and proliferation in clinical-medical usage that these techniques have undergone in recent decades have made them standard tools in the field of cardiovascular medicine. Their success derives from the possibility of obtaining, in a non-invasive, cheap, and reliable way, early diagnosis of various diseases affecting the cardiovascular apparatus, such as heart failure, stenosis and deformation of blood vessels.

This is the context in which this PhD thesis moves. The goal was to develop new ultrasound Doppler methods for blood flow characterization for diagnostic purposes. The experimental phases have included the use of the ULA-OP scanner, an advanced ultrasound research system that offers to developers great freedom in terms of management and control of every part, from the signal transmission to the processing of the received echoes. The work, conducted within the MSD Lab (Microelectronic System Design Laboratory) located at the Department of Information Engineering (DINFO) of the University of Florence, was divided in four distinct stages.

Volume flow is one of the parameters that characterize blood flow. For its evaluation it requires knowing both the velocity distribution within a vessel section and of the area of the section itself. For a thorough evaluation of both, the movements of the artery walls and the complex flow patterns within the artery must be considered. Since the use of standard ultrasound investigation techniques hardly provides such information, in this thesis it is presented a new method for measuring the

volume flow, based on the simultaneous measurement of the velocity profile and the position of the vessel walls. The velocity profile is obtained through a spectral analysis of the signal backscattered from red blood cells based on a multigate technique, according to which the Doppler signal is measured into hundreds of consecutive positions aligned along the investigation line. The walls position is instead detected on the B-Mode image through a wall-tracking algorithm that uses an edge-detector based on the First Order Absolute Moment (FOAM) statistical operator. These topics are described in Chapter 2.

Secondly, an instrument widely used in diagnostic practice was considered: the sonogram, which describes the dynamics of the flow related to a certain depth in the vessel, obtained through a spectral analysis similar to that which leads to the realization of the velocity profile. The flow information provided by the sonogram is usually combined with the morphological one, according to a duplex mode presentation (B-Mode and spectral analysis). However, this approach shows the disadvantage of being characterized by a frame rate of a few tens of images per second. Considering the high acceleration that the heart gives to the blood in the systolic peak (the blood velocity within the common carotid artery can vary from 0 to 1m/s in less than 20ms) the temporal resolution of duplex mode is insufficient for a complete description of the flow.

In order to improve the temporal resolution we have therefore studied the use of non-conventional spectral estimators that produce a power spectral density estimate using a number of samples considerably lower than those necessary to the classical FFT. This study has led to the implementation of the spectral analysis algorithm based on these estimators on the TMS320C6455-EP™ fixed-point DSP present on-board of ULA-OP scanner. This part of the work is detailed in Chapter 3.

Another parameter characterizing the blood flow is its peak velocity, used by physicians to diagnose the degree of a stenosis within a vessel and to decide whether or not to intervene surgically. However, the blood peak velocity measurement is characterized by uncertainty about the Doppler frequency to which it is related. Over the years different and various

methods have been proposed to determine this frequency, but these techniques are often heuristic that do not rely on physical/mathematical models and therefore produce an estimate of this frequency dependent on both the signal noise and spectral broadening.

In this thesis is presented a mathematical model for the spectrum of the Doppler signal backscattered from the red blood cells that provides an accurate value for the Doppler frequency related to the blood flow peak velocity. The testing carried out has highlighted the good results that the method produces considering ideal working hypotheses such as full illumination of parabolic flows. In any case, the research has moved towards the generalization of this model, where non-parabolic flows and not completely illuminated are considered to reproduce more realistic working conditions. The new approach has been implemented in an experimental set-up based on the transmission of plane waves, using a linear array probe. Chapters 4 and 5 contain the description of this research topic.

The extension of the model, while providing a deterministic tool for the detection of the Doppler frequency related to the blood flow peak velocity, does not yet allow to overcome the problem of the Doppler angle knowledge, one of the major sources of error in velocity estimates with ultrasound Doppler techniques. In fact, when the Doppler angle is not known, it can be assessed only projection of the velocity vector along the direction of the acoustic beam. In addition, a low accurate determination of the Doppler angle produces an error whose effect is greater for angles close to 90°. This condition typically occurs in the investigations on the carotid artery, where the probe is placed parallel to the vessel and the Doppler angle is determined by the limited steering capacity of the probe. On the other hand, the implementation of the extended method in a vector configuration provides peak velocity measures that are independent from the Doppler angle. In particular the ULA-OP scanner has been configured in such a manner that a central aperture of a linear array probe transmits a plane wave while two lateral apertures, symmetrically positioned with respect to the probe centre, receive the backscattered signal from the red

cells along two different directions. The implementation and testing of this technique is argued in Chapter 6.

Chapter 1. ULTRASOUND DOPPLER TECHNIQUES

In this chapter the ultrasound physical principles and the basis of the ultrasound techniques are illustrated. Moreover, some fluid dynamic notions are described. The chapter constitutes the fundamental for a full comprehension of the topics discussed in the thesis.

1.1. Ultrasound Basics

The sound is a physical phenomenon described by the propagation of a mechanical wave from a vibrating source through a physical medium such as air, water, human tissues, etc. The perturbation propagates through the alteration of the medium particles, which moves around the equilibrium position. Among acoustic waves (Figure 1.1), ultrasound are those not audible by the human hearing, i.e. those whose frequency is higher than 20kHz. In particular ultrasound propagates through longitudinal waves where the particles oscillate in a direction parallel to the wave propagation.
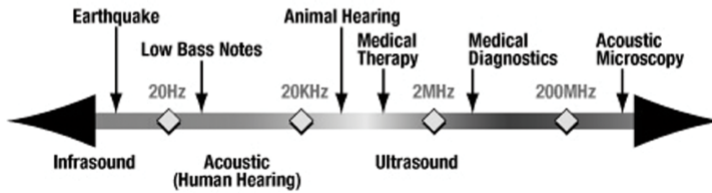
Figure 1.1: Acoustic waves spectrum.

The ultrasound wave propagation along the axial direction (*z*) is described by a second-order linear partial differential equation [1]:

$$\frac{\partial^2 T}{\partial z^2} = \frac{\rho}{\beta} \cdot \frac{\partial^2 T}{\partial t^2} \tag{1.1}$$

where T [N/m^2] is the stress, β [N/m^2] is the elastic constant of the medium and ρ [kg/m^3] is the volumetric medium density. The solution of equation (1.1) is the well-known *plane wave function*:

$$T(z,t) = T_0 \cdot e^{j(\omega t \pm kz)} \tag{1.2}$$

where the wave number k and the pulsation ω are defined as

$$k = \frac{\omega}{c}, \qquad \omega = 2\pi f \tag{1.3}$$

The frequency f [Hz] and the speed of sound in the medium c [m/s] are related via the *wavelength equation*:

$$\lambda = \frac{c}{f} \qquad (1.4)$$

The wavelength λ [m] is defined as the distance between two points along the z-axis presenting the same stress value.

1.1.1. Speed of sound and acoustic impedance

The propagation speed of acoustic waves is strictly dependent on the elastic properties and the density of the medium and it can be expressed as:

$$c = \sqrt{\beta/\rho} \qquad (1.5)$$

For a perfectly elastic medium, in steady temperature and pressure conditions, the speed of sound can be considered constant, since the elastic constant of the medium and the volumetric medium density are so.

Another important property of a medium, used for the characterization of the medium itself, is the *acoustic impedance Z*. For a propagating plane wave, or for a spherical wave far away from the vibrating source, the acoustic impedance is expressed as follows:

$$Z = \rho \cdot c \qquad (1.6)$$

measured in *Rayl* (1 Rayl=1 kg/(m^2 s)).

1.1.2. Scattering, reflection, refraction and attenuation

Similarly to other waves, the ultrasound wave propagation is governed by several phenomena.

The ultrasound wave in a homogeneous medium, i.e. characterized by physical and chemical properties independent from space and time, proceeds along a straight line. If the medium is not homogeneous, the wave front could meet an acoustic impedance discontinuity (interface that produces an echo). In the case the interface roughness is smaller or comparable to the wavelength, part of the acoustic energy is transmitted through the interface and part is spread isotropically in all directions. This phenomenon, referred to as *Rayleigh scattering*, is quantified by the *scattering cross section* (σ), defined as the ratio between the *total spread power* (S) and the *intensity of the incident wave* (I):

$$\sigma = S/I \tag{1.7}$$

Particularly important in ultrasound echography is the *backscattering cross-section*, defined as the ratio between the scattered power per solid angle, in the opposite direction to the source, and the incident intensity. For an imaging system this parameter describes the effective power of the echo signal available.

When the interface roughness is larger than the wavelength of the incident wave (smooth interface) reflection and refraction phenomena occur. In such case, a part of the energy is transmitted through the second medium and a part is reflected. Let's consider the case in which the wave front proceeds, with c_1 speed, from a medium characterized by the acoustic impedance Z_1 to a medium of acoustic impedance Z_2 in which the propagating speed is c_2. According to the *Snell's law*:

$$\frac{\sin \theta_i}{\sin \theta_t} = \frac{c_1}{c_2} \tag{1.8}$$

where θ_i and θ_t are the direction angle of the incident wave and the direction angle of the refracted wave, respectively.
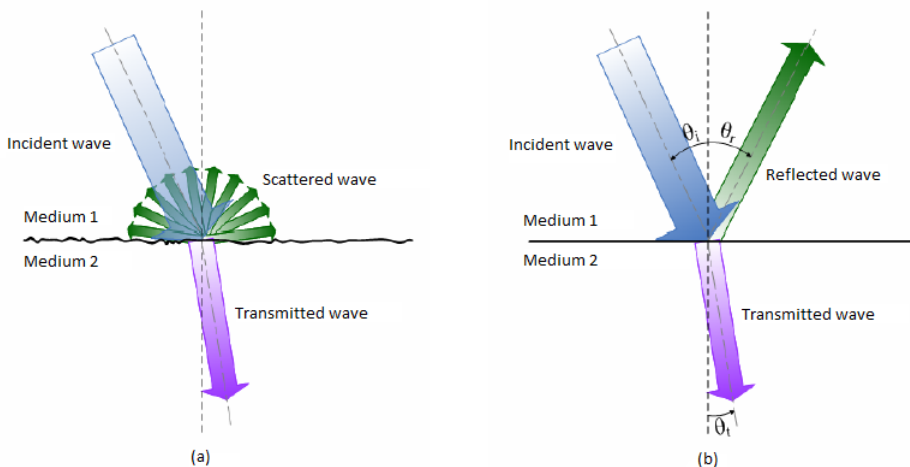

Figure 1.2: Scattering (a) and reflection (b) of a wave at the interface between two media.

The reflection, R, and the transmission, T, coefficients can be defined as follows:

$$R = \frac{(Z_2 \cos \theta_i - Z_1 \cos \theta_t)^2}{(Z_1 \cos \theta_t + Z_2 \cos \theta_i)^2}$$

$$T = 1 - R = \frac{(4Z_1 Z_2 \cos \theta_i \cos \theta_t)^2}{(Z_1 \cos \theta_t + Z_2 \cos \theta_i)^2} \tag{1.9}$$

At the interface, the reflected and the transmitted energies are proportional to the reflection and transmission coefficients, respectively.

Reflection, refraction and scattering occur during the wave propagation and produce an energy dispersion, named *attenuation*. This term refers to any phenomenon that cause a reduction of the wave intensity. Among them, *absorption* and *dispersion* are the most significant. The former process consists into the conversion of part of the mechanical energy into heat energy, by compression, expansion (*thermo-elastic effect*) and sliding of the particles (*viscous effect*). On the other hand, the dispersion process is due to the discontinuity of the medium and thus to all phenomena of scattering, reflection and refraction. The intensity of the acoustic signal decreases exponentially, as described by the attenuation coefficient:

$$I = I_0 e^{-2\alpha_A z} \tag{1.10}$$

where I_0 is the initial intensity. Typically, the attenuation coefficient is expressed as:

$$\alpha_{AdB} = \frac{10}{x} \log \frac{I}{I_0} \tag{1.11}$$

that is the attenuation in dB/(cm·MHz), where x is the thickness of tissue expressed in cm. Table 1.1 shows the values of the parameters previously described for some medium of interest in echography.

Medium	c [m/s]	ρ [kg/m³]	α_{AdB} [dB/(cm MHz)]	Z [MRayl]
Air	330	1.2	-	0.0004
Blood	1584	1060	0.2	1.68
Bone, Cortical	3476	1975	6.9	7.38
Bone, Trabecular	1886	1055	9.94	1.45
Brain	1560	1040	0.6	1.62
Breast	1510	1020	0.75	1.54
Cardiac	1576	1060	0.52	1.67
Connective Tissue	1613	1120	1.57	1.81
Fat	1478	950	0.48	1.40
Liver	1595	1060	0.5	1.69
Marrow	1435	-	0.5	-
Muscle	1547	1050	1.09	1.62
Tendon	1670	1100	4.7	1.84
Soft tissue	1561	1043	0.54	1.63
Water	1480	1000	0.0022	1.48

Table 1.1: The acoustic properties of some tissue of interest, where c is the speed of sound, ρ is the density, α_{AdB} is the attenuation coefficient and Z is the acoustic impedance.

1.2.   Transducers and Probes

1.2.1. Piezoelectric effect

Ultrasound are typically generated and detected exploiting the properties of some materials which, excited by a voltage, modify their dimensions, generating pressure waves. At the same time, when such materials are subjected to an external pressure that cause them a modification in their size, a voltage is generated. Such an effect is known as the piezoelectric effect (Figure 1.3).

An ultrasound transducer is a piezoelectric crystal which is excited by an electric signal at the desired frequency. The most common used material is the *lead zirconate titanate*, known as PZT. However, at present, other materials, presenting acoustic properties similar to those of biological tissues, e.g. *polyvinylidene fluoride* (PVDF), are used as well.
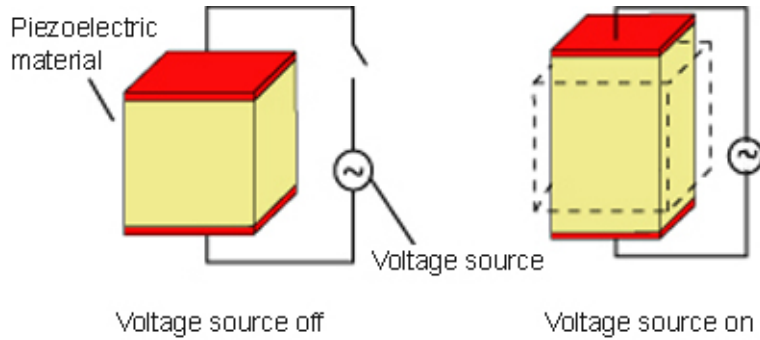
Figure 1.3: Piezoelectric effect.

1.2.2. Piezoelectric transducer basic structure

Figure 1.4 shows the basic structure of a piezoelectric transducer. As shown, a layer of a acoustically absorbent material is placed on the crystal side which is not in contact with the patient skin. Function of this layer, called *backing*, is to fade the crystal oscillation and to absorb the waves reflected from the transducer-skin interface. In effect, designing a transducer necessarily involves solving two main problems. First of all, the acoustic impedance of the transducer must be considered. For example the PZT's acoustic impedance is equal to 29MRayls, which is too high if compared to that of biological tissues. Thus, if the transducer is in direct contact with the skin a total reflection of the acoustic wave will occur. A second issue is the resonant behaviour of the piezoelectric crystal which resonance frequency is:

$$f_{res} = \frac{c_{piezo}}{2A} \qquad (1.12)$$

where c_{piezo} is the sound propagation speed inside the piezoelectric crystal and A is its stiffness. The crystal can oscillate only for a limited and narrow frequency band, limiting the use of short *burst* signals and

producing long oscillation after the excitation is removed (ringing), which affects the imaging system's resolution. The insertion of the *backing* layer reduces the efficiency of the system but, at the same time, increases the transducer fractional bandwidth, i.e. the bandwidth normalized to the centre frequency:

$$\Delta B_\% = 100 \cdot \frac{f_2 - f_1}{f_{res}}$$ (1.13)

where f_1 and f_2 are the lower and upper frequencies at which the response amplitude is decreased by 3dB with respect to f_{res}.

To reduce the reflection coefficient of the transducer-tissue interface, one or more layers having an intermediate acoustic impedance are inserted between the low impedance tissue and the piezoelectric crystal. This technical expedient produces an impedance matching, facilitating the energy transfer from the transducer to the tissue. These layers are referenced to as *matching layers* and their thickness and impedance have to be carefully designed in order to optimize the energy transfer.

The transducer is completed with a metal outer casing, properly grounded, that act as a shield against electrical noise.
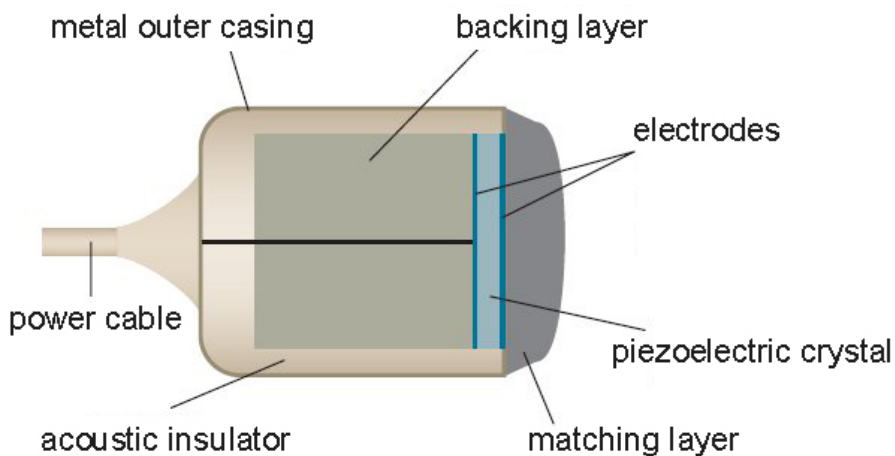
Figure 1.4: Basic piezoelectric transducer structure.

1.2.3. Array transducers

Modern systems make use of more complex structured transducers compared to those described so far. Referred to as *arrays*, they are made of several little radiating elements placed one close to the other, with a periodicity known as *pitch*. As for single-element transducer, an acoustic lens defines a focal distance on the elevation plane. Figure 1.5 reports, as example, the basic structure of a linear array.
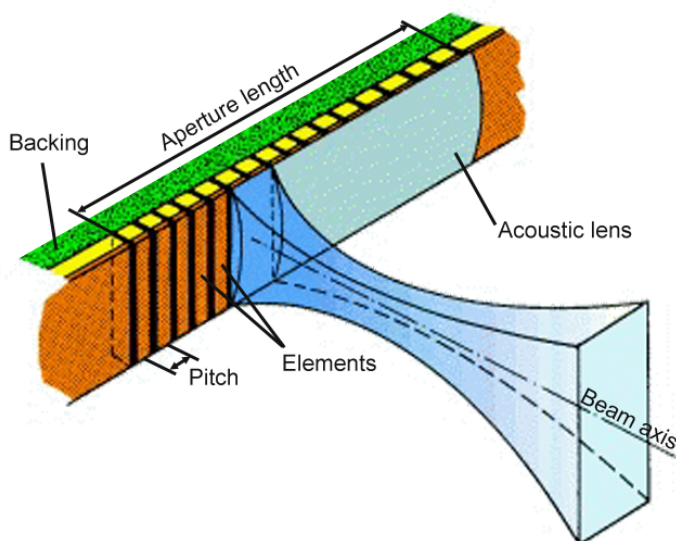
Figure 1.5: Structure of a linear array transducer.

The arrays guarantee high flexibility thanks to the individual control of each element. For example, the acoustic beam can be focused at different positions or steered toward different directions by exciting each element with properly delaying signals. This technique is referred as *electronic focusing*. Furthermore, it is possible to change the beam shape by changing the amplitude, the width and the shape of the *apodization*, i.e. the weight applied to each element. So, the major advantage of arrays is the possibility, by the only means of the electronics, of generating acoustic beams with different characteristics in terms of focusing, position and direction.

The advantages described so far can be exploited in reception as well. The echo signal reaches the elements of the probe at a time depending on

the distance that the echo signal travels. For example, in case of a target in front of the transducer, the central elements, which are closest to the target, receive the echo signal earlier than the lateral elements. The *reception beamforming* [2], [3] is a signal elaboration technique consisting in a coherent recombination of the echo signal received by each element. Each signal is properly delayed and then summed to the other. Furthermore, in digital systems, the possibility of the *reception dynamic focusing* allows a good focus along the entire axis of interest. Data related to the echo-signals received from a series of aligned points by each active element are stored in a memory, sketched as a matrix in Figure 1.6. Each element of the probe is associated to a corresponding row of the matrix memory shown in the figure. Such data should be read in such an order that the contributions of the echoes related to the same inspected item are added in-phase. Indeed, each target gives rise to an echo signal with a spherical wave front. The so-called *dynamic focusing* consists in reading, at each instant, the data from the memory to reconstruct the signal from a corresponding depth.
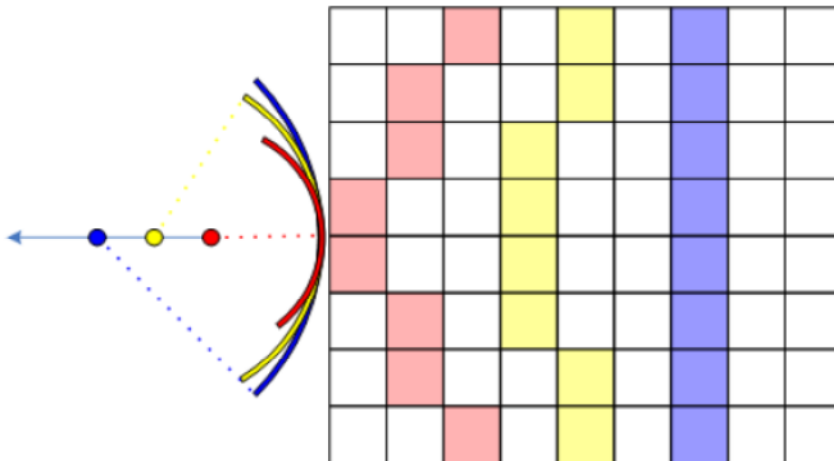

Figure 1.6: Reception dynamic focusing diagram.

1.2.4. Acoustic beam

The acoustic field generated by a transducer in the surrounding space depends on the source geometry. For example, the acoustic beam generated from a circular transducer is reported in Figure 1.7. It can be

divided into two different zones: the first, referred to as *near field* or *Fresnel zone*, shows a constant width; the second, *far field* or *Fraunhofer zone*, is characterized by a diverging beam. The limit between these two zones is placed at a distance from the transducer equal to:

$$z = r^2/\lambda \qquad (1.14)$$

where r is the transducer radius and λ is the transmitted signal's wavelength.

In addition to the main radiation lobe, *side lobes* of lower intensity are present in the acoustic beam. Due to constructive and destructive interferences of the waves generated from each point of the transducer, the origin of these lobes can be demonstrated through the diffraction theory. In the *Fraunhofer zone*, the diffracted beam has approximately the shape of the Fourier transform of the beam on the aperture, i.e. the transducer surface where the beam is originated from. Then, for a finite apertures the beam is a sinc-shaped function showing side lobes of lower intensity that flank the main lobe.
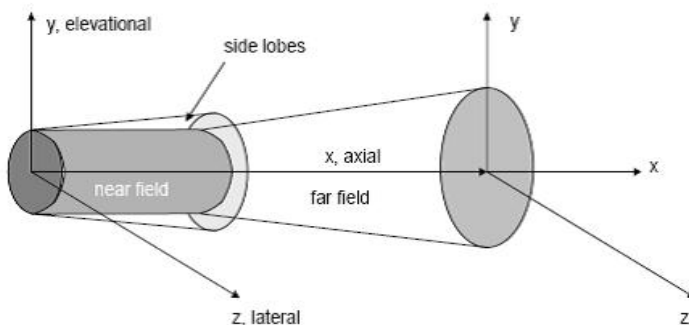
Figure 1.7: Ultrasonic transducer beam field diagram.

Typically, the use of acoustic lens allows the beam field of an ultrasound transducer to be focalized. An acoustic lens is made of a specific material where the ultrasound waves propagate with a different speed compared to that of the tissue to be investigated. Properly designing the lens curvatures, the beam pressure can be maximized at a specific point, i.e. the focus. The transducer sensitivity to the objects close to the focus is then increased with respect to the other objects. Figure 1.8 shows

the simulation of the beam produced by a 5mm radius transducer and focused at 30mm depth.
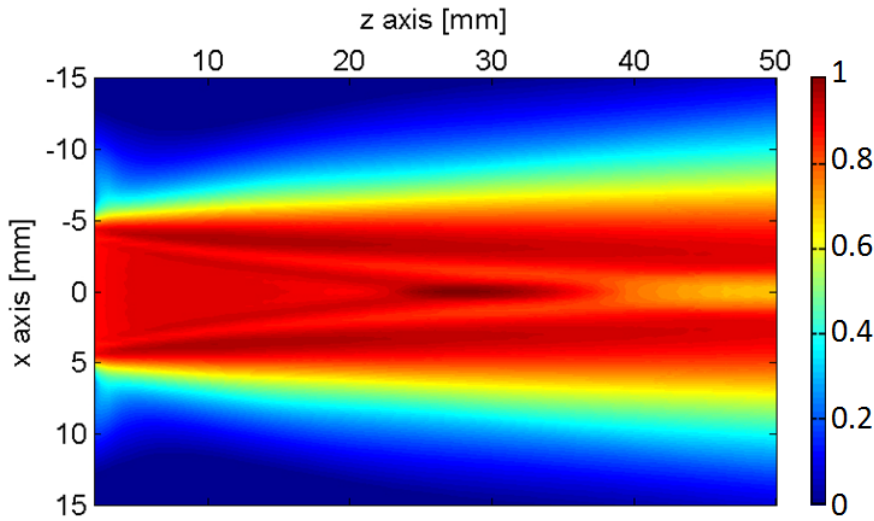
Figure 1.8: Simulated acoustic beam of a 5mm radius transducer focalized at 30mm depth.

1.2.5. System spatial resolution

The system spatial resolution is directly correlated to the transducer characteristics.

The axial resolution indicates the smallest detectable distance between two targets placed on planes that are perpendicular to the ultrasounds propagation direction (z axis in Figure 1.8). This kind of resolution is related to the *sample volume*, i.e. the region of space where the scatterers produce the echo signal received in a time unit. The *sample volume length* (L) is a descending function of both the transmission frequency f_t and the transducer bandwidth B, while its value is bigger for longer transmission bursts. Considering a transmitted burst made of N_c cycles of sinusoid, the length of the sample volume is calculated as follows:

$$L = \left(\frac{N_c}{f_t} + \frac{1}{B}\right) \cdot \frac{c}{2} \qquad (1.15)$$

On the other hand, the lateral resolution indicates the smallest detectable distance between two targets placed on planes that are

orthogonal to the transducer plane (x axis in Figure 1.8). This parameter depends on the focalization, on the transducer geometry and on the transmission frequency.

Actually the system resolution not only depends on the two aforementioned resolutions, but also on the ultrasound beam dimension in the plane orthogonal to the propagation axis (y axis in Figure 1.8). In other words, if the beam width determines the axial and the lateral resolution, the beam thickness determines the elevation resolution, also known as *slice thickness*, that is related to the curvature radius of the acoustic lens positioned over the elements of the transducer.

1.3. The Doppler Effect

In biomedical ultrasound a very important role is played by the so-called *Doppler effect*. The physicist Christian Doppler described the phenomenon that brings his name for the first time in 1842 with a lecture to the Royal Bohemian Society of Science. The work was subsequently published with the title *"On the coloured light of the binary stars and some other stars of the heavens"*.

Let's consider a transmitter, transmitting a wave at f_t frequency, and a receiver in a relative motion one to each other. The *Doppler effect* consists in the variation of the received wave's frequency with respect to f_t.

Let's assume a moving transmitter with respect to a fixed receiver. Let's indicate with v the relative velocity of the transmitter and with θ the angle between the velocity direction and the transmitter-receiver imaginary connecting line. In this case, the relationship between the transmitted and the received frequency, f_t and f_r respectively, is given by the following formula:

$$f_r = \frac{c}{c - v\cos\theta} f_t \qquad (1.16)$$

In case the receiver is moving with respect to a fixed transmitter, the formula becomes as follows:

$$f_r = \frac{c + v\cos\theta}{c} f_t \qquad (1.17)$$

Whether the relative movement is in approaching, an increase, with respect to f_t, in the received frequency will occur. On the other hand, if the transmitter and the receiver are moving away to each other, the received frequency will turn out to be lower than f_t.

Considering the medical applications of ultrasounds, in particular the flowmetric investigations based on the *Doppler effect*, the signal transmitted by the probe is backscattered from the moving red blood cells (*erythrocytes*). Basically they play the role of a moving receiver when the ultrasounds coming from the probe, considered here as a fixed transmitter, "hit" them. At the same time, they act like a moving transmitter when the energy is backscattered toward the probe, now considered as a fixed receiver.

In practice, the received frequency is calculated as a sort of combination of the two aforementioned cases through the following formula:

$$f_r = \frac{c + v \cos \theta}{c - v \cos \theta} f_t \qquad (1.18)$$

The difference between the received and the transmitted frequency is defined as *Doppler Shift* and can be expressed as:

$$f_d = f_r - f_t = \left(\frac{c + v \cos \theta}{c - v \cos \theta} - 1 \right) f_t = \frac{2v \cos \theta}{c - v \cos \theta} f_t \quad (1.19)$$

When the velocity v can be negligible with respect to the speed of sound (c), it can be used the simplified formula:

$$f_d \cong \frac{2v \cos \theta}{c} f_t \qquad (1.20)$$

This is the case of flowmetric investigations in which it is allowed to use the formula (1.20). By measuring the *Doppler Shift* , if the angle θ is known, it is possible to estimate the blood flow velocity through the following formula:

$$v = \frac{c f_d}{2 f_t \cos \theta} \qquad (1.21)$$

1.4. Ultrasound Doppler Systems

Ultrasound systems used for Doppler flowmetric investigations are from two main categories: the *Continuous Wave* (CW) and the *Pulsed Wave* (PW) systems.

Historically first used, CW systems use probe made of two transducers. During the system operation, one of the two transducers continuously transmits acoustic energy toward the target while the other one receives the backscattered signal. In this case the sample volume is localized in the area where the transmission and the reception beams overlap. Unfortunately this technique does not allow for *gating* on the received signal, so that the contributions from different depths cannot be distinguished, but gives a general information about the trend inside the sample volume.

PW systems, instead, use a single transducer that alternatively acts as a transmitter and as a receiver. During the transmission period, the transducer is excited with bursts, i.e. short pulses composed of a predefined number of sinusoidal cycles, that are repeated at a frequency called *Pulse Repetition Frequency* (PRF). The reception phase occurs during the time between two consecutive burst transmissions. Thus, knowing the speed of sound inside the tissue (c) and the time interval (Δt) between the transmission and the reception of an echo, it is possible to recover the depth d at which the echo has been generated:

$$d = \frac{c \cdot \Delta t}{2} \qquad\qquad (1.22)$$

It is clear that, operating a *gating* on the received signal, it is possible to relate each temporal window to a certain depth.

Depending on the number of gates between two consecutive bursts, PW systems are typically classified as *single-gate* or *multi-gate* systems. In single-gate systems it is possible to isolate the echo coming from just one single depth whilst the echoes from different depths can be simultaneously collected in multi-gate systems.

Since characterized by a regular alternation between transmission and reception phases, PW multi-gate systems show a limit for the depth range that can be investigated. In particular, the maximum and minimum

distances are conditioned by factors such as the *burst duration* (D) and the PRF value. Indeed, the reception phase can start only after the transmission is completely done, so for this reason the minimum detectable depth (d_{min}) can be expressed as follows:

$$d_{min} = \frac{c \cdot D}{2}$$
(1.23)

Echoes coming from distances smaller than d_{min} cannot be detected.

Similarly, echoes that, to reach the probe, take a longer time than that between two consecutive bursts cannot be received. This means that the maximum depth that can be investigated (d_{max}) is given by:

$$d_{max} = \frac{c}{2 \cdot PRF}$$
(1.24)

The factor 2 in the denominator of equations (1.23) and (1.24) is due to the fact that the ultrasonic packet travels the distance twice before it can be detected: it goes to the target and then it returns to the probe.

Another limitation of PW systems related to the PRF value has effect on the *maximum detectable Doppler frequency* (f_{max}) and so on the *maximum detectable velocity* (v_{max}). In fact, in order to avoid the *aliasing* phenomenon, f_{max} can be expressed as follows:

$$f_{max} = \frac{PRF}{2}$$
(1.25)

So the maximum velocity detectable can be determined as:

$$v_{max} = \frac{c \cdot PRF}{4 f_t \cos \theta}$$
(1.26)

1.5. *Doppler Signal Bandwidth*

Considering the equation (1.20), we can theoretically assert that the Doppler signal generated from a single scatterer moving at velocity v is made of one single frequency. This would lead us to think about the spectrum as made of just one spectral line.

Actually, the spectrum shows a widening, called *Intrinsic Spectral Broadening* (ISB), due to two main reasons: the *Transit Time Broadening* and the *Geometrical Broadening*.

Transit Time Broadening

A scatterer generates a Doppler signal while it passes through the acoustic beam. This produces a broadening of the spectrum because the signal lasts for a finite time (correlated to scatter velocity and the length travelled inside the beam). Moreover the acoustic energy of the beam is not uniform.

Geometrical Broadening

Since ultrasound transducers has always apertures with finite dimension, the acoustic beam is composed of several rays neither parallel to the transducer axes nor to each other. This gives raise to several Doppler angles that correspond to different frequency components in the echo signal.

Moreover, there is another cause for the spectral broadening due to the fact that the sample volume is populated with several scatterers each one with its own velocity and direction. If the velocity is not uniform, the bigger the sample volume, the bigger the generated broadening.

1.6. Doppler Angle Role in Velocity Assessment

In the paragraph describing the Doppler effect, the equation (1.21) represents the velocity of the red blood cells as a function of the *Doppler shift*. The expression indicates that the velocity is inversely proportional to the cosine of the Doppler angle so it is evident that for an accurate measurement of the velocity, the Doppler angle should be known as well. Unfortunately this is not the case in most of the clinical exams, and large errors are present [4].

When the Doppler angle is unknown, it can be assessed only the axial component of the velocity, i.e. the projection of the velocity vector along the ultrasonic beam direction:

$$v_{axial} = v \cos \theta \qquad (1.27)$$

In *in-vitro* tests this problem is easily overcome by imposing a known angle between the probe and the flow direction. On the other hand, it is

clear that such a solution cannot be used in *in-vivo* acquisitions. Although it is possible to roughly figure out the vessels position inside the tissues, it is impossible to establish their direction *a priori*.

It can be demonstrated that a $\pm\Delta\theta$ error in Doppler angle affects the velocity assessment causing a percentage error equals to:

$$\frac{\Delta v}{v} = \frac{\cos\theta - \cos(\theta + \Delta\theta)}{\cos(\theta + \Delta\theta)} \cdot 100 \tag{1.28}$$

In Figure 1.10 the trend of the percentage error is reported as a function of the Doppler angle parameterized for five values of the relative angle error. As it is shown, the closer the angle is to 90°, the greater the error in the velocity assessment.
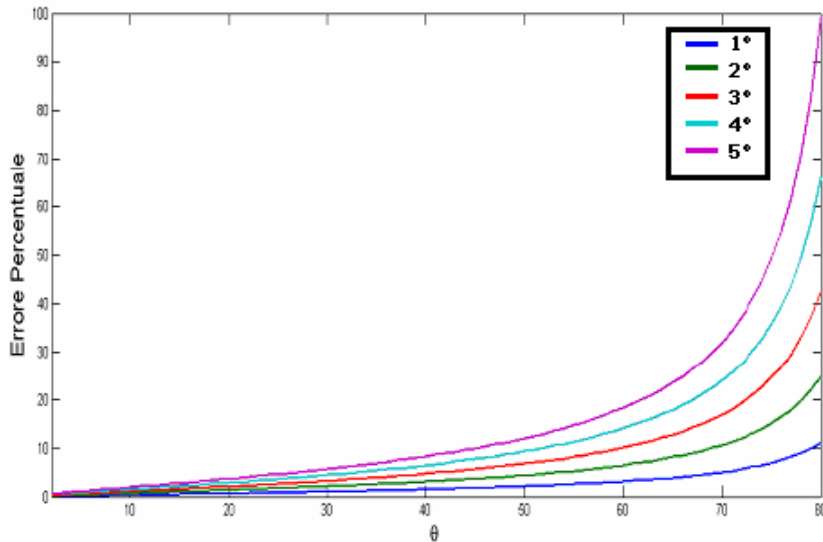
Figure 1.10: Percentage error in velocity assessment reported as a function of the Doppler angle and parameterized for five values of the relative angle error.

1.6.1. *Vector Doppler technique*

A method for obtaining both the modulus and the direction of the velocity vector consists in the simultaneous use of two or more acoustic beams. For example, the use of two beams allows to measure the projection of the velocity vector on the plane where the two beams

overlap. Adding a third beam, not coplanar with the others, all the spatial velocity components can be determined.

For a general explanation, let's firstly consider the situation reported in Figure 1.11, where a PW working modality is considered.

Figure 1.11: PW working modality where an active aperture transmits a plane wave along a direction that forms a θ_t angle with respect to the vertical. At distance d from the surface of the probe, the wave hits a moving target whose velocity forms the angle θ_v with respect to a plane parallel to the probe surface.

An active aperture transmits a plane wave at frequency f_t along a direction that forms a θ_t angle with respect to the vertical. At distance d from the surface of the probe, the wave hits a moving target whose velocity forms the angle θ_v with respect to a plane parallel to the probe surface. In reception, the frequency of the acquired signal can be calculated as follows:

$$f_d = \frac{f_t}{c} v [\cos(\theta_{dt}) + \cos(\theta_{dr})] \qquad (1.29)$$

where:

$$\begin{cases} \theta_{dt} = 90 - \theta_v + \theta_t \\ \theta_{dr} = 90 - \theta_v + \theta_r(d) \end{cases} \qquad (1.30)$$

Substituting the (1.30) in (1.29) and simplifying we have:

$$f_d = \frac{f_t}{c} v \left[\cos(90 - \theta_v + \theta_t) + \cos(90 - \theta_v + \theta_r(d)) \right]$$

$$= -\frac{f_t}{c} v \left[\sin(\theta_t - \theta_v) + \sin(\theta_r(d) - \theta_v) \right] \qquad (1.31)$$

Let's consider now the symmetrical configuration, as reported in Figure 1.12, arguing the same way.
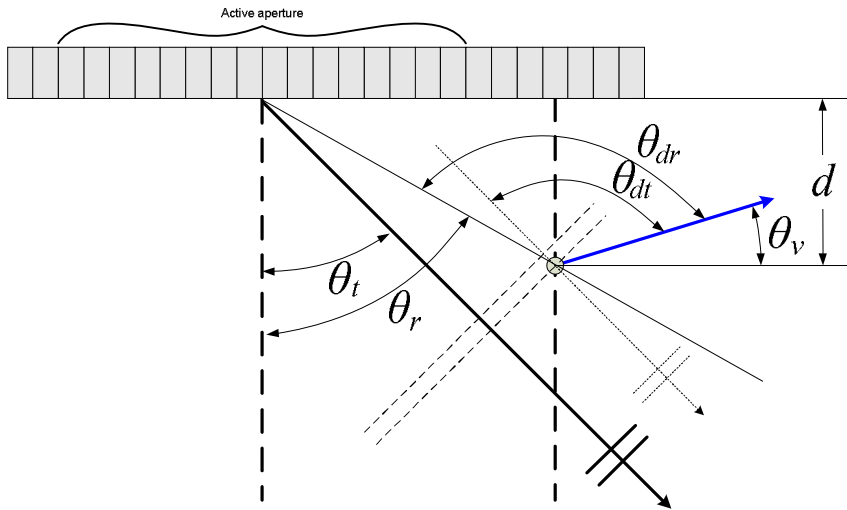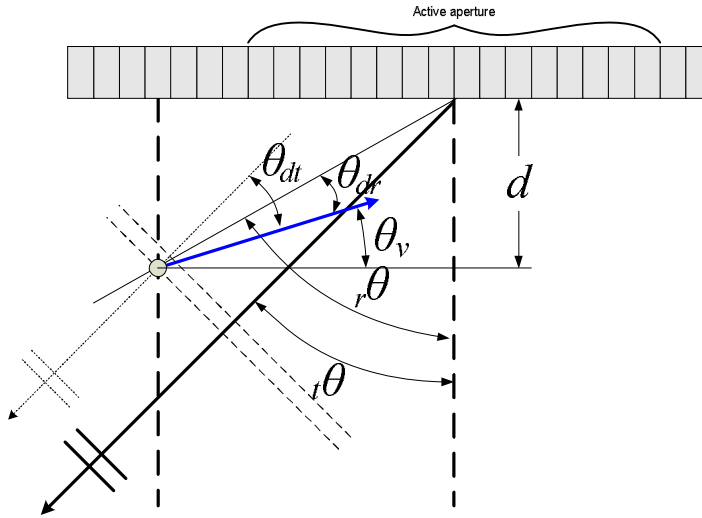

Figure 1.12: PW working modality where an active aperture transmits a plane wave along a direction that forms a θ_t angle with respect to the vertical. At distance d from the surface of the probe, the wave hits a moving target whose velocity forms the angle θ_v with respect to a plane parallel to the probe surface.

The (1.29) is still valid, but in this case we have:

$$\begin{cases} \theta_{dt} = 90 - \theta_v - \theta_t \\ \theta_{dr} = 90 - \theta_v - \theta_r(d) \end{cases} \qquad (1.32)$$

so that, substituting equation (1.32) in equation (1.29), and simplifying, the formula for the received frequency becomes:

$$f_d = \frac{f_t}{c} v[\cos(90 - \theta_v - \theta_t) + \cos(90 - \theta_v - \theta_r(d))]$$
$$= \frac{f_t}{c} v[\sin(\theta_t + \theta_v) + \sin(\theta_r(d) + \theta_v)] \tag{1.33}$$

Thus we have two received frequencies:

$$\begin{cases} f_{d_1} = -\frac{f_t}{c} v[\sin(\theta_t - \theta_v) + \sin(\theta_r(d) - \theta_v)] \\ f_{d_2} = \frac{f_t}{c} v[\sin(\theta_t + \theta_v) + \sin(\theta_r(d) + \theta_v)] \end{cases} \tag{1.33}$$

Summing up the expressions of f_{d_1} and f_{d_2}, we get:

$$\begin{aligned} f_{d_1} + f_{d_2} &= \frac{f_t}{c} v[-\sin(\theta_t - \theta_v) - \sin(\theta_r(d) - \theta_v) \\ &\quad + \sin(\theta_t + \theta_v) + \sin(\theta_r(d) + \theta_v)] \\ &= -\frac{f_t}{c} v[\sin(\theta_t - \theta_v) - \sin(\theta_t + \theta_v) \\ &\quad + \sin(\theta_r(d) - \theta_v) - \sin(\theta_r(d) + \theta_v)] \end{aligned} \tag{1.34}$$

Since:

$$\begin{cases} \sin(\theta_t - \theta_v) - \sin(\theta_t + \theta_v) = -2\cos(\theta_t)\sin(\theta_v) \\ \sin(\theta_r(d) - \theta_v) - \sin(\theta_r(d) + \theta_v) = -2\cos(\theta_r(d))\sin(\theta_v) \end{cases} \tag{1.35}$$

the equation (1.34) can be written out again as follows:

$$f_{d_1} + f_{d_2} = 2\frac{f_t}{c} v[\cos(\theta_t)\sin(\theta_v) + \cos(\theta_r(d))\sin(\theta_v)] \tag{1.36}$$

On the other hand, subtracting the expressions in (1.33) and considering that:

$$\begin{cases} \sin(\theta_t - \theta_v) + \sin(\theta_t + \theta_v) = 2\sin(\theta_t)\cos(\theta_v) \\ \sin(\theta_r(d) - \theta_v) + \sin(\theta_r(d) + \theta_v) = 2\sin(\theta_r(d))\cos(\theta_v) \end{cases} \tag{1.37}$$

we obtain that:

$$f_{d_1} - f_{d_2} = -2\frac{f_t}{c} v[\sin(\theta_t)\cos(\theta_v) + \sin(\theta_r(d))\cos(\theta_v)] \tag{1.38}$$

Since the velocity v can be written as follows:

$$v = \frac{v_x}{\cos(\theta_v)} = \frac{v_z}{\sin(\theta_v)} \tag{1.39}$$

it is possible to write the equations (1.36) and (1.38) in terms of x and z components of the velocity v obtaining:

$$\begin{cases} f_{d_1} + f_{d_2} = 2\dfrac{f_t}{c} v_z \left[\cos(\theta_t) + \cos(\theta_r(d))\right] \\ f_{d_1} - f_{d_2} = -2\dfrac{f_t}{c} v_x \left[\sin(\theta_t) + \sin(\theta_r(d))\right] \end{cases} \tag{1.40}$$

Finally, from equation (1.40) it is possible to calculate the x and z components of the velocity v independently from the Doppler angle:

$$\begin{cases} v_z = \dfrac{c}{2f_t} \left[\dfrac{f_{d_1} + f_{d_2}}{\cos(\theta_t) + \cos(\theta_r(d))} \right] \\ v_x = -\dfrac{c}{2f_t} \left[\dfrac{f_{d_1} - f_{d_2}}{\sin(\theta_t) + \sin(\theta_r(d))} \right] \end{cases} \tag{1.41}$$

Moreover, the θ_v angle that the velocity vector forms with respect to the probe surface is easily obtainable through the following formula:

$$\theta_v = \tan^{-1}\left(\frac{v_z}{v_x}\right) \tag{1.42}$$

1.7. Echo-signal Elaboration

1.7.1. Common scanning techniques

The advent of array transducers fostered the development of new imaging techniques. Indeed, as previously stated, the arrays allow the electronic steering and moving of the ultrasonic beam. Several scanning techniques exist and differ in the geometry of the examined region and in the used probe. An overview of the most used scanning techniques is listed in the following paragraphs; see Figure 1.13 for a diagram.
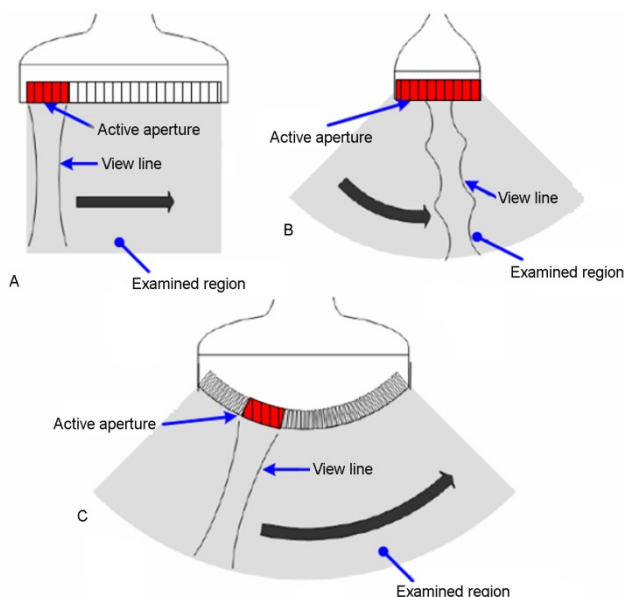
Figure 1.13: Scanning techniques and probes: Linear (A), Phased (B) and Convex (C).

Linear scan

It uses linear array, where the array elements are placed on a straight line. A rectangular region is examined by several parallel view lines. The transmission and reception active aperture is moved covering the entire array aperture. This technique is adopted when a high lines density is necessary and the region of interest is small, e.g. superficial vessels.

Convex scan

In this case the transducer is a convex array, i.e. the elements are placed on a circumference arc. As linear scan, the active aperture is moved covering the whole transducer. The examined region is a circle sector and it is useful for wide regions of interest, e.g. abdomen or internal organs.

Phased scan

It is used with phased array probe which are short linear array having small width elements. All the elements are simultaneously used both in transmission and in reception; the view line is progressively moved with different steering angles covering a sectorial region. Phased scan is

suitable for wide regions of interest when they are hidden by superficial structures, e.g. the heart hidden by the rib cage.

Nowadays the development of modern ultrasound system allows the imaging of three-dimensional regions. Such techniques exploit two-dimensional matrix array probes or mechanically moved linear or convex arrays.

1.7.2. Elaboration modes and display

The echo signals received by the ultrasound probes are processed by the ultrasound system that extracts the information content and displays it in a user-friendly way. The displaying techniques are various and most of them are actually used in medical diagnosis.

Among these techniques, the *M-Mode* (Motion Mode) is based on a single view line in which the intensity of the signal received on consecutive shots are displayed on adjacent positions on a greyscale image. This technique lets the user appreciate the temporal changes in echoes. In fact, the depth of echo-producing interfaces is displayed along one axis and time is displayed along the second axis, recording motion of the interfaces toward and away from the transducer.

The *B-Mode* (Brightness Mode) is the most used diagnostic technique, which allows the user to investigate the morphological structure of tissues. It consists in a two-dimensional presentation of echo-producing interfaces in which the intensity of the echo is represented on a greyscale by modulating the brightness of the spot. The position of the interface is determined from the transit time of the acoustic pulse.

Other modes are employed for Doppler applications using the so-called *spectral analysis* to the received Doppler signals. In practice, every PRI the received echoes are sampled, demodulated in in-phase and quadrature components (I/Q), by multiplying the samples for $\sin(2\pi f_t t)$ and $\cos(2\pi f_t t)$ functions, and low-pass filtered. The resulting complex samples are stored in a matrix whose columns, from left to right, gather data corresponding to successive PRIs (Figure 1.14(a)). This means that each row of the matrix stores the so called *slow-time samples* from a

specific depth. The spectral analysis starts when every row of the matrix is processed through windowing and FFT (*Fast Fourier Transform*) [1] to obtain the spectral matrix (Figure 1.14(b)) which is the same size as the previous one. In the next step the power is calculated (Figure 1.14(c)) and the resulting power spectral matrix, when colour-coded and displayed, shows an intuitive representation of the velocity profile of the flow (Figure 1.14(d)).
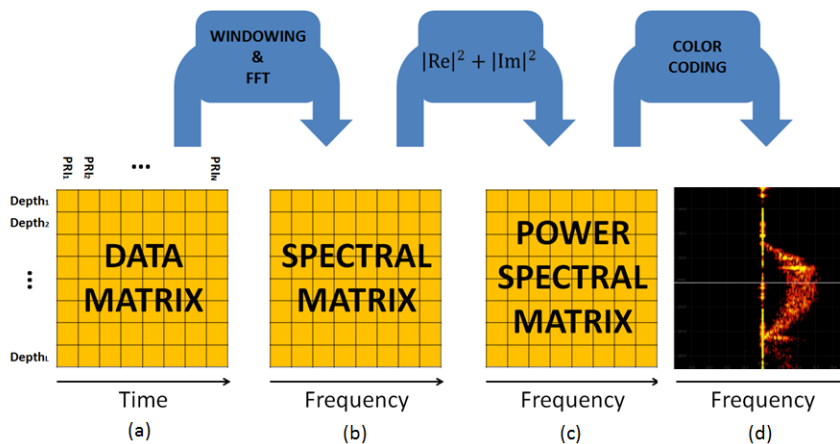
Figure 1.14: Basic steps to get the power spectral matrix with the Doppler shift. Data acquired from each PRI are demodulated and arranged in the columns of data matrix (a). Every row is processed through windowing and FFT (b) and the power is extracted (c). The matrix, color coded, produces a graphical representation of the frequency profile (d).

The elaboration described so far is known as *Multigate-Spectral-Doppler* (MSD-Mode) that allows seeing the flow evolution at each depth along a single view line.

Another most common and used feature is the so-called *spectrogram*, or *sonogram*, which shows the temporal evolution of the flow speed at a single depth.

Figure 1.14: B-Mode (left), MSD-Mode (right) and Spectrogram (bottom) during the investigation of a common carotid artery.

1.8. *Fluid Dynamics: Some Basics*

In this paragraph the notions of fluid dynamics, used in this work, are briefly introduced.

First of all it is worthwhile to notice that in the biomedical field Doppler velocimetry mainly refers to the blood as the fluid to investigate. The blood is a bodily fluid in humans and other animals that delivers necessary sub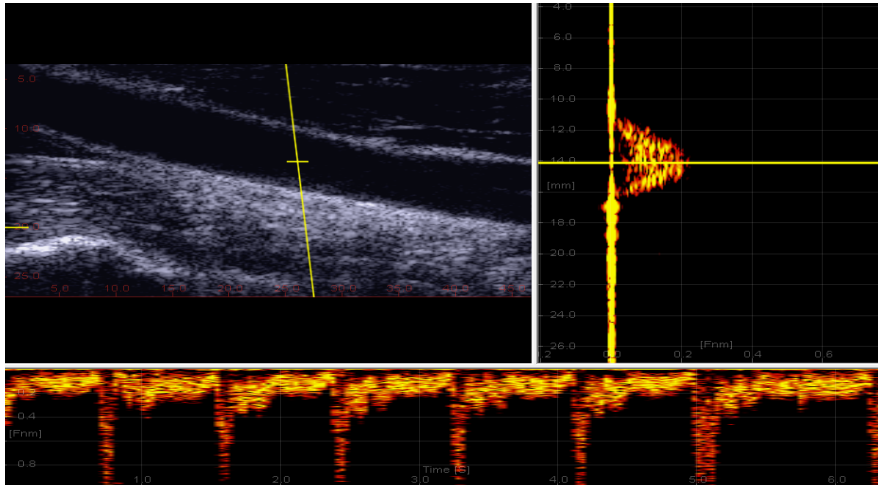stances such as nutrients and oxygen to the cells and transports metabolic waste products away from those same cells. In vertebrates, it is composed of blood cells suspended in blood plasma. Plasma, which constitutes 55% of blood fluid, is mostly water (92% by volume), and contains dissipated proteins, glucose, mineral ions, hormones, carbon dioxide, and blood cells themselves. The blood cells are mainly red blood cells (also called *erythrocytes*), white blood cells (also called *leukocytes*) and platelets. The most abundant cells in vertebrate blood are red blood cells. Blood circulates around the body through blood vessels by the pumping action of the heart. In animals with lungs, arterial blood carries oxygen from inhaled air to the tissues of the body, and venous blood carries carbon dioxide from the tissues to the lungs to be

exhaled. The blood shows *non-Newtonian* characteristics and so its viscosity changes when the fluid velocity changes.

1.8.1. Laminar and turbulent flow

Generally, flow type can be divided in laminar and turbulent. The flow can be considered laminar when the fluid is characterized by smooth and constant fluid motion. In this case viscous forces are dominant and the infinitesimal layers that make up the fluid itself don't mix each other. This means that at each depth of a straight pipe the fluid flows always in the same direction, parallel to the wall of the channel (see Figure 1.15).
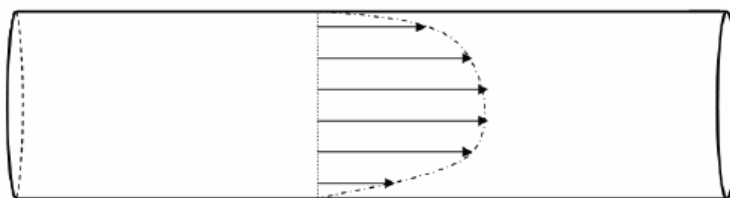
Figure 1.15: Example of a laminar flow.

As the velocity increases, the laminar condition becomes unsteady and degenerates in a turbulent state. Differently from the laminar flow, the turbulent one is dominated by inertial forces, which tend to produce chaotic eddies, vortices and other flow instabilities (see Figure 1.16).
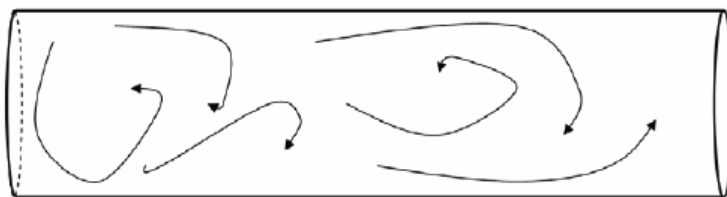
Figure 1.16: Example of turbulent flow.

In fluid dynamics, in order to characterize the two different flow regimes within the same fluid it is used the so called *Reynolds Number* (Re). For flow in a pipe of diameter D, the Reynolds Number is defined as:

$$Re = \frac{\rho \cdot \bar{v} \cdot D}{\eta} = \frac{4 \cdot Q \cdot \rho}{\pi \cdot D \cdot \eta} \qquad\qquad (1.43)$$

where ρ is the fluid density [g/cm^3], $\bar{v}$ is the average velocity within the fluid, η is the viscosity of the fluid [P], and Q is the volume flow in the tube [m^3/s]. Experimental observations show that for "fully developed" flow, laminar flow occurs when the Reynolds Number is less than 2100 and turbulent flow occurs when it is greater than 4000. In the interval between 2300 and 4000, laminar and turbulent flows are possible and are called "transition" flows, depending on other factors, such as pipe roughness and flow uniformity. This result is generalized to non-circular channels using the hydraulic diameter, allowing a *transition Reynolds Number* to be calculated for other shapes of channel. These transition Reynolds numbers are also called *Critical Reynolds Numbers* and are different for every geometry.

1.8.2. Parabolic flow

Let's consider a Newtonian fluid entering in a cylindrical pipe with velocity v. Before its profile could be considered stable, the fluid must travels for a certain distance (see Figure 1.17). This is due to the fact that the viscosity forces are gradually transferred to the centre of the pipe. As consequence, the depth, at which those forces are not conveyed yet, progressively moves toward the centre of the tube.
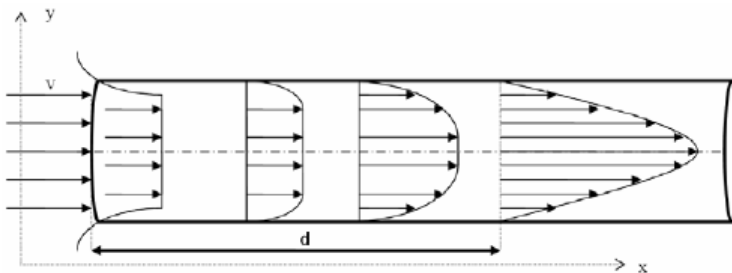

Figure 1.17: Velocity profiles at the inlet of a tube. It can be noticed that the fluid need to travel for a distance d before its profile could be considered parabolic.

Near the inlet, only the fluid close to the wall withstands the viscosity forces and a great transverse velocity gradient can be noticed in this zone. As the flow goes away from the entrance of the pipe this gradient decreases because the region where the fluid layers are subjected to the viscosity forces expands. Since for each pipe section the volume flow must be the same, the fluid at the centre must accelerate to compensate the peripheral deceleration.

The distance d shown in Figure 1.17 is called *inlet distance*. It has been experimentally proved that, for a straight tube of diameter D, the inlet distance can be calculate as follows:

$$d \cong 0.06 \cdot D \cdot Re \qquad (1.44)$$

After this distance, the flow is stable and its velocity profile has the shape of a parabola.

An interesting property of flows showing a parabolic velocity profile consists in a simple formula for the maximum velocity inside the tube. If the flow shows a parabolic velocity profile, its average velocity is given by the following formula:

$$\bar{v} = \frac{v_{max}}{2} \qquad (1.45)$$

where v_{max} is the maximum velocity inside the tube, i.e. the velocity at the centre of the tube. Thus, since the volume flow Q of a pipe with section S is defined as follows:

$$Q = \bar{v} \cdot S \qquad (1.46)$$

using equation (1.45) in (1.46), we easily obtain that:

$$v_{max} = \frac{8 \cdot Q}{\pi \cdot D^2} \qquad (1.47)$$

1.9. ULA-OP System

The lack of flexibility in commercial ultrasound machines makes difficult to perform the experimental test of novel ultrasound investigation methods. In the best case, these only provide beamformed radiofrequency or demodulated echo-signals for acquisition and post-processing. High-level research platforms allow more flexibility, but high cost and unwieldy dimensions typically characterize them. This paragraph presents the powerful but portable ultrasound system, specifically designed for research purpose, named ULA-OP [5], [6].

Acronym of *ULtrasound Advanced-Open Platform*, the ULA-OP is a compact and complete ultrasound system designed and developed at the MSD Laboratory (Department of Information Engineering, DINFO, University of Florence, Italy). In two main boards, an analog board and a digital board, all the electronics necessary to control up to 64 active elements of a 192 array probe are present. The ULA-OP system consists in a metal rack of dimensions 34×23×14cm, connected to a PC where a dedicated software runs (see Figure 1.18). The backplane in the rack integrates the probe connector and routes the signals among the power unit and the two main boards.
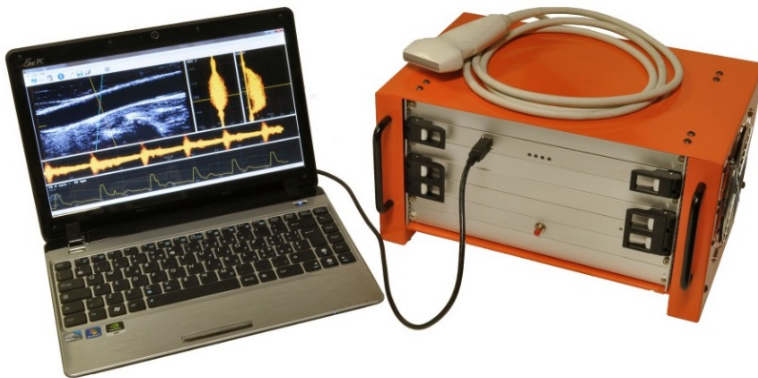

Figure 1.18: ULA-OP system connected to a PC.

The analog board includes the RF front-end while the digital board hosts the devices in charge of numerical signal processing. The modularity

of ULA-OP allows the addition of further boards for possible extension of the system capabilities. Table 1.2 shows the main features of the ULA-OP system.

General Features	Open platform 64 independent TX/RX channels Size: 34×23×14cm; Weight: 5kg Power consumption<90W
Transmitter	64 Arbitrary waveform generators Max output voltage: 24Vpp Frequency: 1 to 16MHz
Receiver	Input Noise: 2nV/√Hz Bandwidth: 1 to 16MHz Analog gain: 6÷46dB with programmable TGC 12bit @ 50MSPS ADCs
Beamformer	Programmable apodization and delays (dynamic focusing)
Processing Modules	Coherent demodulation, band-pass filtering, decimation, B-mode, Multigate Spectral Doppler, Vector Doppler… (open to new, custom modules).
Storage capabilities	Up to 1GB for RF data (pre- or post-beamformed) Up to 512MB for baseband data Fast data streaming toward high capacity storage units (HD)
Software tools	*Beam Planner, Config Editor, Real-time Module, Video Browser, RF viewer*

Table 1.2: ULA-OP main features.

The analog board includes the transducer front-end, with electronics for analog conditioning of the 64 channels, and a programmable switch matrix, necessary to dynamically map each transmission/reception (TX/RX) channel to one transducer element. In Figure 1.19 it is sketched the architecture of ULA-OP data processing chain.
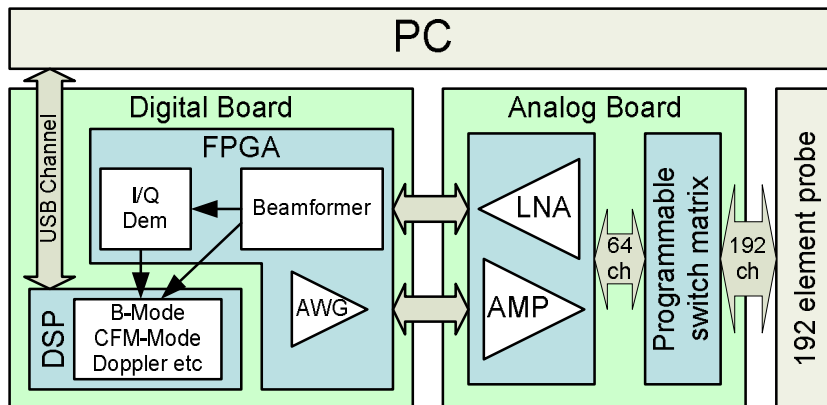
Figure 1.19: Architecture of ULA-OP data processing chain.

The digital board is in charge of synthesizing the TX bursts and beamforming and processing the received echoes in real-time. As shown in Figure 1.20, the radio-frequency (RF) front-end includes 4 identical sections. Each section controls 16 TX/RX channels, including 2 Analog-to-Digital Converters (ADCs) with 8 channels each, a Front-End FPGA (FEFPGA) and 256MB of DDR2 memory. The FEFPGAs communicate with a Master FPGA (MFPGA) that distributes data, commands and settings among the devices and synchronizes the system operations. A Digital Signal Processor (DSP) is connected to the MFPGA for general control and high level data processing. The FPGAs are from Stratix II family (Altera, San Jose, CA, US), and the DSP belongs to the TMS320C64™ family manufactured by Texas Instruments (Texas Instruments Incorporated, Dallas, TX, US). A total of 1.25GB DRAM is distributed on the digital board to store TX sequences, *beamforming* parameters, and acquired data. The MFPGA connects to a USB 2.0 controller, for communication with a host PC where a custom software runs. This software displays the results of real-time processing and presents a user-interface suitable for controlling the system. Different panels show the operating parameters and the graphical output.
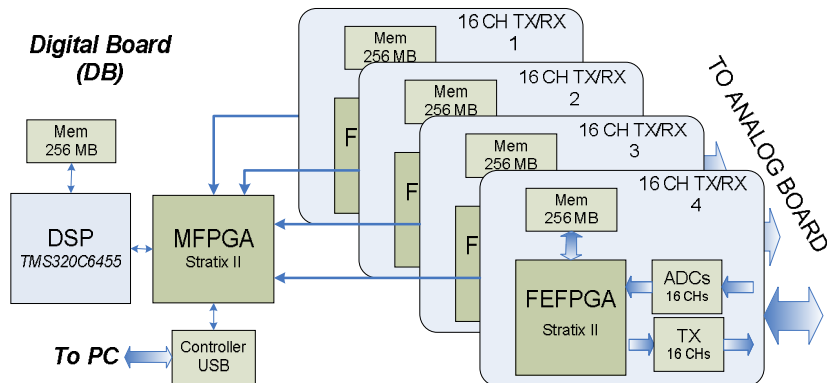
Figure 1.20: ULA-OP digital board architecture.

ULA-OP integrates two DDR2 SDRAM, of 1GB and 256MB size, respectively, managed like circular buffers. The larger buffer is reserved to pre-beamforming RF (raw) data, consisting of 12-bit sample streams at 50MHz rate (Figure 1.21-A). The second buffer is used for RF beamformed (Figure 1.21-B) and/or baseband data (Figure 1.21-C). Here, the throughput rate depends on the *Pulse Repetition Interval* (PRI) and the decimation factor, and it can be low enough so that 256MB of memory can hold several seconds or even minutes of data. The user can stop the scanning at any time and download to a PC file the last data gathered in the circular buffers.
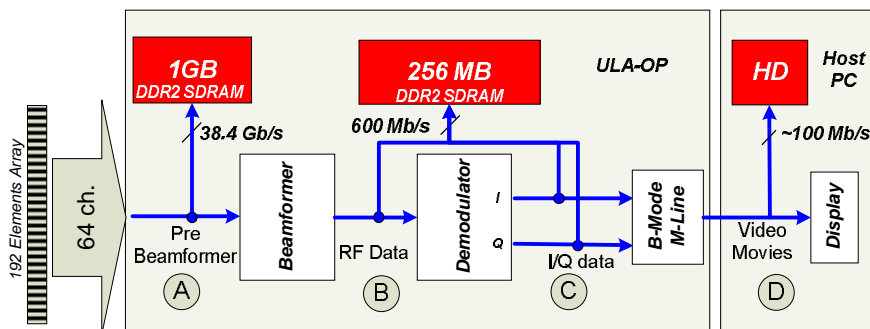
Figure 1.21: Data access. Data at 12-bit, 16-bit and 24-bit are saved in A, B and C section, respectively. Video data (D) are coded at 8-bit/pixel.

Moreover, data obtained after the elaboration made by the DSP can be saved as well. This data typically includes video frames which are ready,

or so, to be displayed (Figure 1.21-D). The real-time PC software allows saving the video data directly to the hard-disk, in-line with the scanning session.

In all of the aforementioned cases, data are saved according to a documented open format, including two files: a small text file containing the parameters describing the acquisition session (e.g. the PRI, TX and RX configuration, TGC setting, dimension and position of the region of interest (ROI), etc) and a larger binary file with the raw data.

All system settings are managed through a configuration file held in the host PC. This includes details about the display parameters, acquisition setting, elaboration module instances and TX/RX signal definitions. Whenever the user wants to implement arbitrary TX/RX schemes and/or use personalized waveforms, ULA-OP needs to be programmed by two additional configuration files. The availability of different configuration files allows the user to quickly switch between predefined settings simply by choosing from a menu. Furthermore, some parameters such as the PRF, focal depth and steering angle are directly editable from the real-time software interface.

Any probe with a maximum number of 192 elements can be associated to ULA-OP through the ITT Cannon DLM5-260P connector. The pin-out is directly compatible with the commercially available linear, phased and convex array probes produced by Esaote Spa (Firenze, Italy). In all of the performed experiments, the commercial linear array probe LA533, having a 7MHz 6dB bandwidth between 3MHz and 13MHz, was used.

1.9.1. SIMAG

In this work the most of ULA-OP configuration files have been created using an ultrasound system simulator called SIMAG [7]. Based on Field II® [8], [9] software, in SIMAG each system parameter and setting, e.g. beamforming or signal generation, is directly and individually computed by its mathematical modules.

SIMAG is characterized by a main interface from which the user can access to other interfaces such as the *Transducers Settings* interface (Figure 1.22) and the *Tx/Rx Settings* interface (Figure 1.23). The former defines all of the transducer properties, i.e. physical properties, electrical

properties and the displacement of the active elements. Arranged in a list, the names of the already set transducers are useful to recall all the transducer properties by a mouse click.
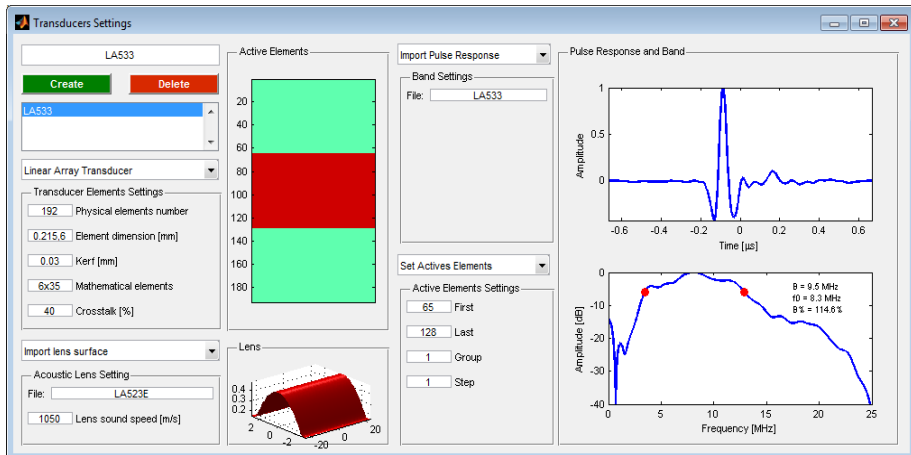
Figure 1.22: Transducer Settings interface.

The *Tx/Rx Settings* interface is used to set the modes of transmission and reception, i.e. the signal to be transmitted, the transmission focusing, the reception beamforming and the demodulation parameters. It is organized in three panels: Mode, Signal and Demodulation, and Tx/Rx Beamforming.

In the Mode panel the user can define what kind of scan is to be performed, i.e. a linear scan, a sector scan, a single-shot or a plane waves scan. Furthermore, the user can select the transmission and the reception transducers. Also in this case the names of the already set modes are arranged in a list to recall all the mode properties by a mouse click.

In the Signal and Demodulation panel, a pop-up menu allows to select among different kind of signals, e.g. sine wave, square wave, etc.. Then the related panel is loaded with the proper forms that have to be filled by the user with the desired signal properties. Defined in the Demodulation settings sub-panel, the demodulation parameters must be set accordingly to the signal. The signal and the demodulation filter response are then plotted in the related graphs.
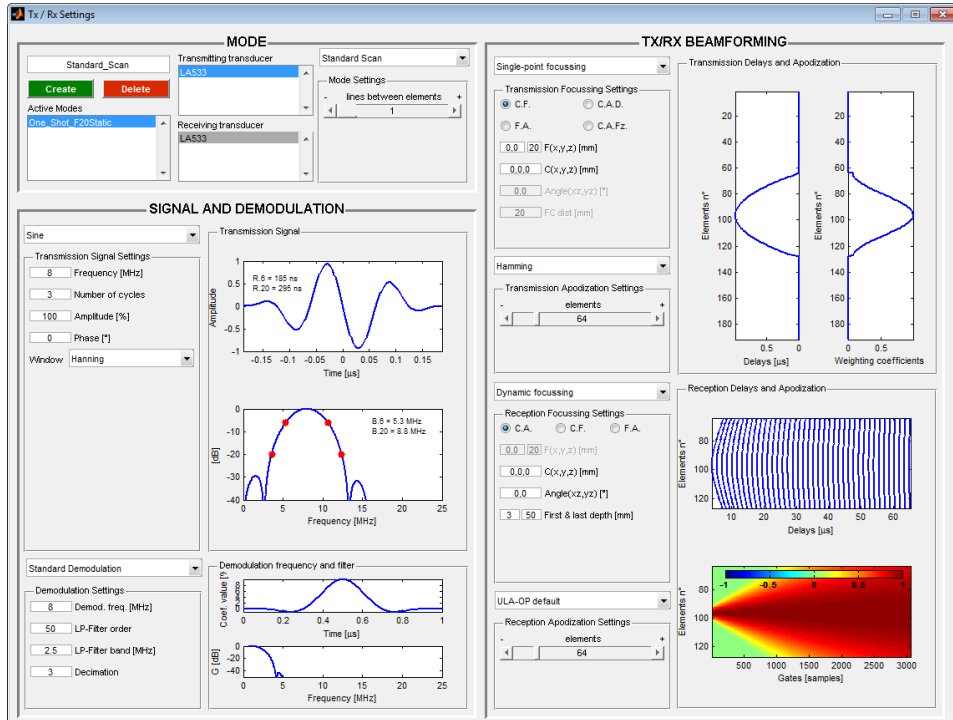
Figure 1.23: Transducer Settings interface.

The Tx/Rx Beamforming panel is employed to set the transmission and reception beamforming schemes. Standard focusing is available but it is even possible to set limited diffraction beams or file imported electronic delays. The transmission *apodization* curve can be selected by a pop-up menu and the aperture width can be modified by a slider control. The reception beamforming can be set, with settings having the same meaning as in transmission, but dynamic focusing and apodization are available.

Chapter 2.   NOVEL METHOD FOR VOLUME FLOW ASSESSMENT

This chapter describes the implementation of a novel volume flow measurement method based on the simultaneous assessment of both the velocity profile and the wall positions. The method has been implemented in a specifically designed signal processing platform.

2.1. Introduction

The typical approach for blood volume flow assessment consists in measuring the blood velocity in a single sample volume placed in the middle of the vessel, estimating the average vessel diameter, and applying a flow model, e.g. the quasi-static Poiseuille parabolic flow distribution [10], for inferring the final estimate. This simple approach is affected by poor accuracy and repeatability for two main reasons: complex flow configurations, usually present in the artery, cannot be taken into account and, moreover, the wall distension, which in important regions like the common carotid artery (CCA) could easily exceed the 10% of the diameter, are ignored.

Using more sophisticated models let to achieve better results even if some limitations remain. For example, the *Womersley model* [11] accounts for blood pulsatility, but its application is limited to straight tubes with rigid walls [12], thus neglecting the flow distortions due to curvatures.

These limitations can be solved by the use of MSD, which allows the measurement of the actual velocity profile across the artery with high temporal resolution [13]. This technique can be exploited to provide an accuracy improvement that is bigger when the real profile differs from the ideal shapes predicted by the aforementioned mathematical models.

Here the implementation of a novel volume flow measurement method based on the simultaneous assessment of the velocity profile, obtained from MSD data, and wall positions, obtained from B-mode data using a wall-tracking algorithm is presented. The method represents an evolution of [14] which was based on a dual-beam custom board [15] with no imaging capabilities. The volume flow assessment application has been implemented on Matlab® (The MathWorks Inc., Natick, MA).

2.1.1. Method

The wall-tracking algorithm employed locates the walls in the B-Mode image by exploiting a detector based on the *First Order Absolute Moment* (FOAM) statistical operator. The detector performs a recursive calculation of the mass centre point of the grey level variability that occurs in a predefined circular area which must include the wall. This procedure

quickly converges towards the edge following the minimum distance direction. The initial circular area is selected by the operator in the first B-Mode frame, then the algorithm automatically tracks the edges in the subsequent frames. The FOAM algorithm was selected because of its good capability of tracking the inner region of the lumen.

The velocity profile is obtained from the PW data according to the MSD technique described in Chapter 1, §1.7.2. The data acquired during each PRI are arranged along a corresponding column of a 512×128 Data Matrix. The Power Spectral Matrix is estimated by processing each row through 128-point FFT, and extracting the corresponding power. The result is log-compressed and arranged in a new 512×128 matrix. After a de-noising process, the power-weighted mean frequency is calculated from each row, and converted to velocity according to the classic Doppler equation (1.20).

2.2. Signal Processing

Implemented as Matlab® (The MathWorks Inc., Natick, MA) classes, a set of functional blocks constitutes the signal processing chain used for the volume flow assessment application. Each block of the signal processing chain performs a specific task and works in cascade with the other blocks. This means that the output of an upstream block is the input for a downstream block. Figure 2.1 shows the flow chart of the main functional blocks used for the volume flow assessment.
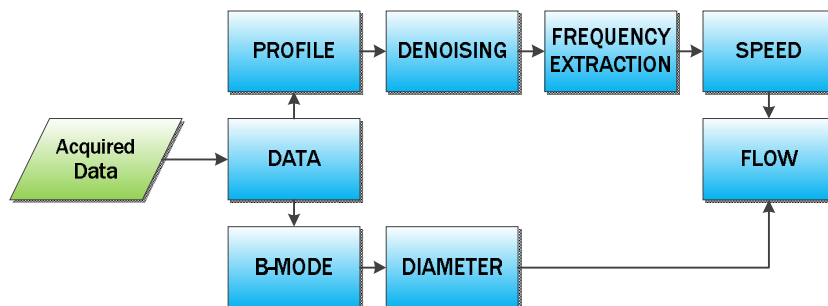

Figure 2.1: Signal processing main blocks.

Working as an interface between the signal processing chain and the ULA-OP system, the *Data class* converts the acquired data, stored in a specific file, into a two dimensional Matlab® matrix. Its output is the input of both the *B-Mode* and the *Profile classes*.

As suggested by the name, the *B-Mode class* implements the B-Mode processing. Data are organized in lines and frames, interpolated along either axial and lateral direction, and filtered both in time and in 2D spatial domain. Furthermore, a logarithmic scale compression is applied and the results converted in a colour scale. The *B-Mode* outcome is further processed by the *Diameter class* which infers the vessel diameter and calculates the position of both near and far walls.

As far as the upper branch of Figure 2.1, the *Profile class* processes the output of *Data class* similarly to the ULA-OP real-time software. Through N-point FFTs, Multigate-Spectral-Doppler (MSD) profiles are reconstructed. High-passed filtered, in order to remove the low frequency spectral components due to the *clutter*, these spectra contain the information about the distribution of blood velocities at different depths. Following, the *Denoising class* applies a threshold to the profile by a recursive estimation of the investigated depth. This allows the *Frequency Extraction class* to extract the corresponding local Doppler mean frequency by a weighted average algorithm. Subsequently, in the *Speed class*, the mean frequency is converted to blood velocity according to the classic Doppler equation (1.20).

The *Flow class* uses the *Speed* and *Diameter* outputs to assess the instantaneous volume flow $Q(t)$ according to the following formula:

$$Q(t) = \pi \int_{-R(t)}^{R(t)} v(r,t) \cdot |r| \cdot \delta r \qquad (2.1)$$

In (2.1) $v(r,t)$ represents the axial velocity profile measured along the vessel diameter at instant t and depth r. Provided that $-R(t)$, $R(t)$ are the wall positions tracked by the FOAM algorithm at instant t.

Figure 2.2 shows the graphic user interface for the volume flow assessment application. On top, from left to right, the *B-Mode*, the *Profile*

and the *Speed* plots. On bottom, the control panel (left side) and the *Flow* (upper right side) and *Diameter* (lower right side) trends.
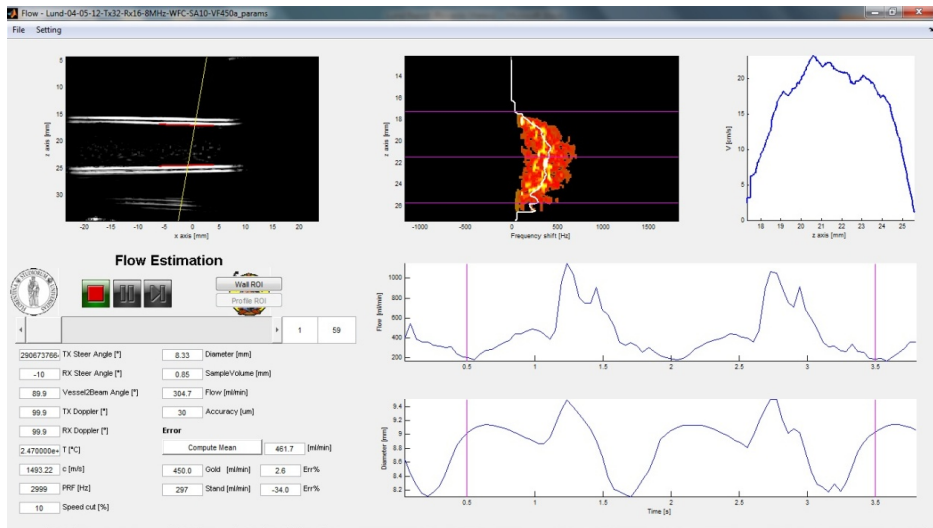
Figure 2.2: View of the signal processing interface for the volume flow assessment application.

2.3. Experiments

2.3.1. Experimental set-up

The proposed method has been tested on flow phantom using the ULA-OP system coupled with the 192-element linear array probe LA523 (Esaote SpA, Florence, Italy). The probe, featuring 6dB-bandwidth between 5.9MHz and 10.6MHz, was excited in duplex mode by 8MHz Hanning windowed bursts of 5 and 3 cycles for PW- and B-Mode, respectively. ULA-OP was configured to show a real-time B-Mode and MSD display windows, useful for probe and PW-lines positioning, and a sonogram (see Figure 2.3).
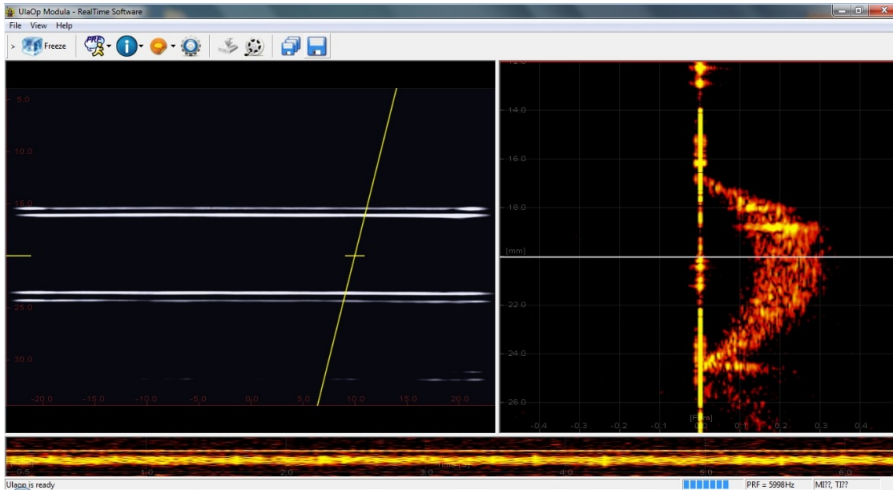
Figure 2.3: View of the ULA-OP real-time software used during data acquisition for volume flow tests.

ULA-OP was configured to save I/Q raw data from both B-Mode and PW-lines down-sampled to 25Msps.

The tests were carried out at Lund University through the experimental set-up depicted in Figure 2.4. A programmable progressive cavity pump [16], controlled by a PC, forced a blood mimicking fluid to flow from a reservoir into a tube immersed in a water tank. Suitable fittings in the measuring site allowed assembling pipes of different materials and dimensions. In the reported experiments rigid plastic and flexible silicon pipes of 8mm diameter were used. The probe, held at the top of the measuring site, was aligned in longitudinal position parallel to the pipe axis.

The blood mimicking fluid was prepared by dissolving 3.4g of Orgasol® (Arkema Inc. Philadelphia, PA) in 2ℓ of demineralised water [17]. The Orgasol® is constituted by 10μm polyamide spherical particles, capable of producing an US backscattering effect similar to that generated by human blood erythrocytes. To support an uniform particle distribution, 1.8g of surface-active agent was also added to the fluid. Finally, to guarantee perfect homogeneity, the solution was mixed for several hours by a magnetic stirrer before and during each experimental session.
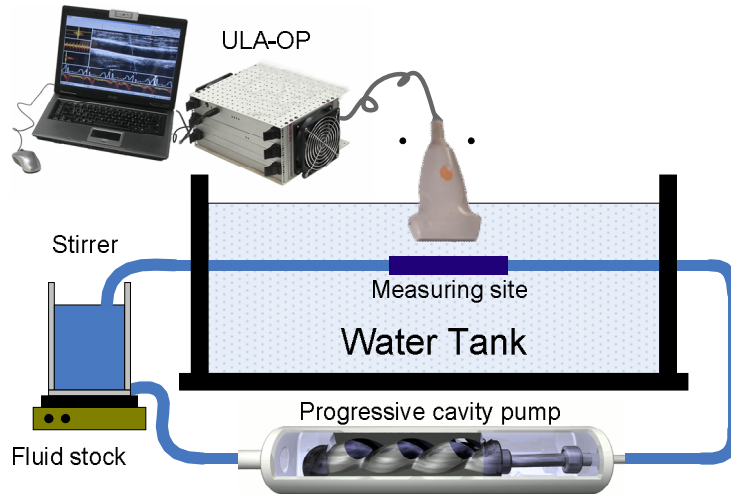
Figure 2.4: Experimental set-up used during the acquisition sessions.

2.3.2. Tests

The new method was tested with more than 1700 experiments carried out in steady, sinusoidal, and pulsatile flow condition. Both rigid and flexible pipes have been used in the experiments. For each flow/pipe combination (see Table 2.1), different steering angles and flow rates were used. For example, with flexible pipe and sinusoidal flow trend, the nominal volume flow was changed in the range 60÷630ml/min in 30ml/min step (19 different rates) and the steering angle in the range 10°÷22° in 2° step (7 different angles). For each configuration 3 measurements of several seconds were performed, for a total of 19×7×3=399 measurements.

For each measurement, about 50MB of I/Q data were saved in both B-Mode and PW-Mode and post-processed through Matlab® software. B-Mode images were re-calculated on 512×192 points, obtaining a frame sequence at 50Hz rate. The edge detector was then applied to the B-Mode sequence and the two points where the investigation line intersects the walls were finely located and tracked. PW data were processed by a 30Hz wall filter and 128-point FFT with 50% overlap. Velocity assessments were produced at 62.5Hz rate. Finally, after interpolating the wall position

measurements in order to match the rate of blood velocity estimation, the instantaneous blood volume flow was calculated by equation (2.1).

Flow/Pipe Condition	Flow Rates	Steering Angles	Total Experiments
Rigid/Constant	60÷750ml/min, step: 30ml/min	10°÷22° step: 2°	504
Rigid/ Sinusoidal	60÷630ml/min, step: 30ml/min	10°÷22° step: 2°	420
Flexible/ Sinusoidal	60÷600ml/min, step 30ml/min	10°÷22° step: 2°	399
Flexible/Pulsed	350÷560ml/min	10°÷22° step: 2°	420
TOTAL EXPERIMENTS			**1743**

Table 2.1: Experimental conditions.

2.4. Results

The measurements were analysed in order to evaluate the accuracy and reproducibility of the proposed method. In particular, the accuracy was assessed by comparing the measurement Q_m to the reference value Q_g produced by the calibrated pump.

The percentage error has been calculated following the formula:

$$Err[\%] = \frac{Q_m - Q_g}{Q_g} \cdot 100 \qquad (2.2)$$

Figure 2.5 reports the histogram of the errors calculated from all measurements. A Gaussian curve is fitted to the histogram for comparison.
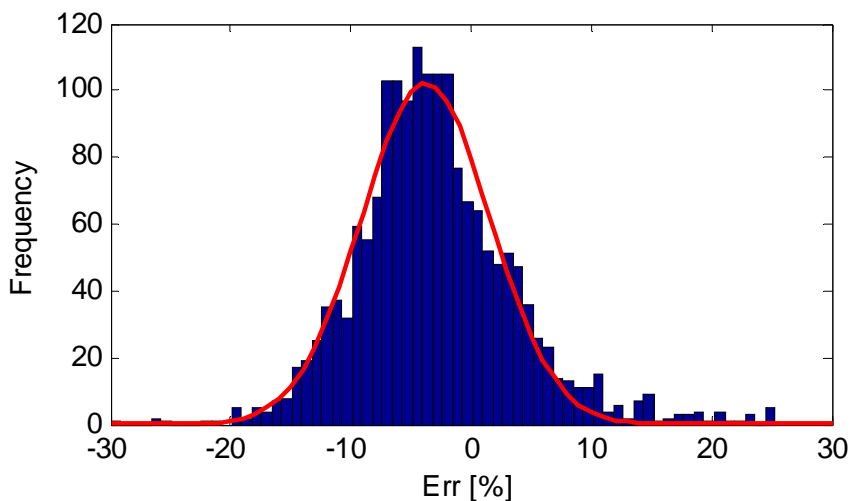
Figure 2.5: Relative error distribution (dark bars) compared to Gaussian (red-line) fitted to relative error values.

The mean and standard deviation (SD), listed in Table 2.2 together with 95% confidence bounds, are −3.7% and 5.3%, respectively. The value of the coefficient of determination of the fitting (R^2) confirms that the percentage error population is well represented by the normal distribution.

	Value	95% Confidence bounds	
Mean	−3.7%	−4.0%	−3.5%
Standard Deviation	5.3%	5.0%	5.6%
Coefficient of Determination R^2	0.96	-	

Table 2.2: Fitting results.

Figure 2.6 shows the comparison between the estimated flow and the reference according to the *Bland-Altman approach* [18]. The vertical axis reports the difference between the data to be compared, normalized to their mean value, which in practice corresponds to the percentage error.

The horizontal axis reports the average of the values to be compared, which can be approximated to the nominal flow.
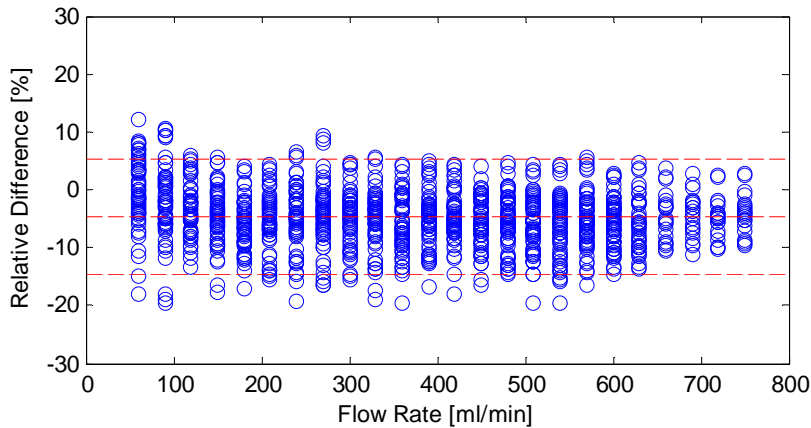
Figure 2.6: Bland-Altman comparison between proposed and reference volume flow measurement methods.

The three horizontal dashed lines show, from top to bottom, the high limit of agreement (+6.1%), the mean value (−3.7%), and the low limit of agreement (−13.5%).

The reproducibility was first qualitatively evaluated by comparing 3 measurements obtained for each flow/pump/pipe configuration. For example, Figure 2.7 reports the measurements obtained for a 420ml/min nominal flow in pulsed conditions at 12° steering angle. The acquisitions were aligned at the first peak for a better comparison.
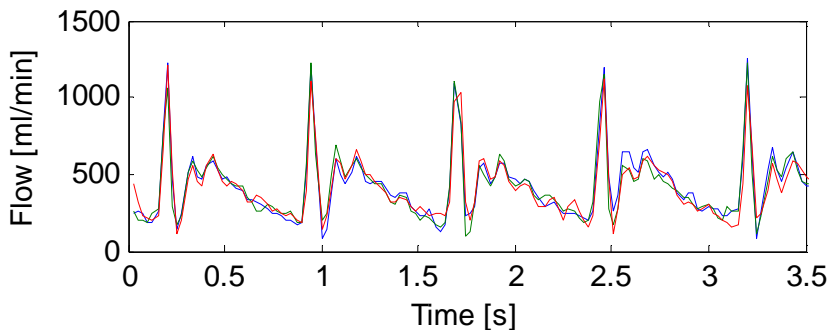
Figure 2.7: Three overlapped measurements obtained with pulsed flow, 12° steering angle, 420ml/min nominal flow.

The repeatability was then quantified by means of the coefficient of variation (CV) [19], which is obtained by the standard deviation (SD) of the repeated measurements divided by their average value. From the 1743 measurements, i.e. 581 triplets, we calculated CVs populations with a 1.7% mean value and 1.7% SD.

Chapter 3. AMPLITUDE AND PHASE ESTIMATORS (APES)

In this chapter unconventional spectral estimators, for producing good quality sonogram with a reduced number of samples with respect to the common method, are presented. In particular two different implementations on a state-of-the-art fixed-point DSP are described.

3.1. Introduction

As previously sketched in Chapter 1, §1.4, in a typical echo-Doppler investigation the flowing blood is periodically insonated by bursts of ultrasound energy transmitted every PRI, which typically ranges between 100μs÷1ms. The echoes backscattered from erythrocytes moving across a selected depth range are received, amplified, and sampled along the depth direction, the so-called *fast-time direction*. The collected data are then arranged in a matrix so that each new column contains the echo gathered from a new pulse. The samples coming from a certain depth, aligned along the so-called *slow-time direction*, are processed to obtain the *Power Spectral Density* (PSD), which accounts for the axial velocity distribution of the insonified scatteres. The PSD evaluated for a single depth, typically located at the middle of the vessel, produces the *spectrogram*, or *sonogram*, [1] widely employed in diagnostic practice (Figure 3.1 shows an example).

The preferred approach for PSD calculation consists of a sequence of moving window *periodograms*, typically obtained through the conventional *Fast Fourier Transform* of a windowed input signal segment. The *Welch method* [20], which consists of averaging a set of partially overlapped *periodograms,* each obtained from the FFT of a windowed segment of the input signal, represents an extension of the basic approach that allows to reduce the Doppler spectral variance.

Although this last method is robust with respect to artifacts and is computational very efficient, the performance required in diagnostic applications are attainable only if no less than 64÷128 samples per estimate are employed. A corresponding number of PRIs are necessary to gathered such an amount of samples.
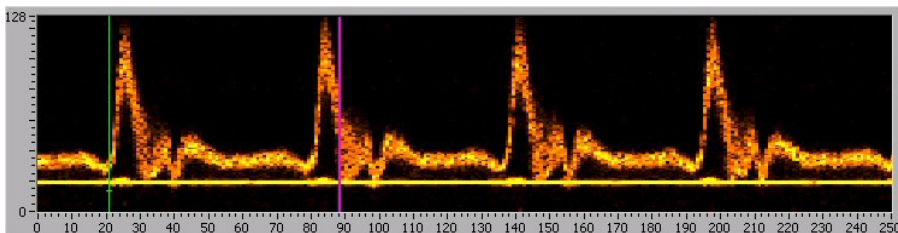

Figure 3.1: Example of spectrogram.

This aspect has effects directly on the performance of the system in terms of *temporal resolution* (t_r) and, in case of duplex working modality, in terms of *frame rate* (FR). Indeed, supposing N is the number of samples necessary for producing the sonogram, the temporal resolution is given by the formula:

$$t_r = \frac{N}{PRF} \qquad (3.1)$$

The smaller the value of t_r, the better the temporal resolution of the system. Considering constant the PRF, it can be noticed as an increase in the value of N determines an increase in the value of t_r, and this leads to a worsening in the temporal resolution of the system. On the other hand, according with the formula (3.2), when working in a duplex mode, if the number of samples N increases, the frame rate decreases and the overall performance of the system lower.

$$FR = \frac{PRF}{2 \cdot N} \qquad (3.2)$$

Recently the application of *Amplitude and Phase EStimators* (APES) [21], typically used in aerospace applications [22], has been proved capable to produce a good quality *sonogram* with a reduced number of transmissions. In particular Gran et al. [23], adapting the APES for medical application, proved that the number of transmissions to be used to get good quality *spectrograms* can be reduced down to 16. Unfortunately APES requires much more calculations than Welch, making its real-time implementation quite challenging, especially in a fixed-point arithmetic environment.

Fixed-point arithmetic is often used in DSP systems due to its simplicity and area-efficiency compared to floating-point arithmetic. The goal is to implement the APES method on the 32-bit fixed-point TMS320C6455-EP™ DSP (Texas Instruments Incorporated, Dallas, TX, US) present on the digital board of the ULA-OP system described in Chapter 1, §1.9. The aforementioned DSP has a single core of the C64x+™ family, running at 1GHz. The core is based on the VelociTI™ very-long-instruction-word (VLIW) architecture and includes 8 parallel calculation units. Up to 2 32×32-bit multiplications (or 4 16×16-bit), 4

summations and 2 32-bit data transfers to/from the cache memory are possible in a single clock cycle [24].

3.2. Method

3.2.1. APES: basics

The APES method can be interpreted like a bank of matched filters. Each filter allows a particular frequency of interest to pass while minimizing the total output power. A detailed explanation of APES can be found in [21], in the following a brief description is reported for reader convenience. Here $\bar{X}$ and $\tilde{X}$ represent a matrix and a vector, while $\bar{X}^T$ and $\bar{X}^H$ represent the transpose and the complex conjugate transpose of $\bar{X}$, respectively.

Let $\tilde{Y}(l)$ be the vector containing the N demodulated elements y_p sampled from a given depth in the *p-th* PRI with p ranging between l and $l + N - 1$:

$$\tilde{Y}(l) = [y_l, y_{l+1}, \dots, y_{l+N-1}]^T \tag{3.3}$$

and

$$\bar{Y} = [\tilde{Y}(l), \tilde{Y}(l+1), \dots \tilde{Y}(l+N+L-1)] \tag{3.4}$$

Let $\tilde{E}_N(\varphi)$ be the *N-point* Fourier column vector:

$$\tilde{E}_N(\varphi) = \left[1, e^{j2\pi \cdot \varphi}, \dots, e^{j2\pi \cdot \varphi \cdot n}, \dots, e^{j2\pi \cdot \varphi(N-1)}\right]^T \tag{3.5}$$

The echo, y_l, generated by a scatterer moving with velocity v toward the transducer, illuminated by a burst of ultrasounds at frequency f_t and repeated at $PRF = 1/PRI$ rate, can be described by the following model [23]:

$$y_l = A \cdot e^{-j \cdot 2\pi \cdot l \cdot \frac{2vf_t}{c \cdot PRF}} = A \cdot e^{-j \cdot 2\pi \cdot l \cdot \varphi} \tag{3.6}$$

The sample y_l is gathered after coherent demodulation in the *l-th* PRI. The constant A accounts for the transmission amplitude, the backscattering properties and the constant phase delay related to the distance from the transducer, while c represents the speed of sound. According to APES, the

PSD is obtained in a three-step process. First, assuming that a normalized Doppler frequency φ is present in the signal $\tilde{Y}(l)$, the vector $\tilde{S}(\varphi)$ is calculated by adding L segments of N samples each, after compensating for the phase shift introduced by the delays among PRIs:

$$\tilde{S}(\varphi) = \sum_{l=0}^{L-1} \tilde{Y}(l) \cdot e^{j \cdot 2 \cdot \pi \cdot \varphi} \tag{3.7}$$

In the second step, the N-*by*-N autocovariance of the noise, i.e. the signal to be rejected by the filter bank, is estimated:

$$\overline{Rs}(\varphi) = \overline{Ry} - \tilde{S}(\varphi) \cdot \tilde{S}^H(\varphi) \tag{3.8}$$

where $\overline{Ry}$ is the autocovariance of the input signal averaged over L segments. In the last step, the PSD at normalized frequency φ is finally calculated, for each of the M desired frequency points:

$$PSD(\varphi) = \left| \frac{1}{L} \left(\frac{\overline{Rs}(\varphi)^{-1} \cdot \tilde{E}_N(\varphi)}{\tilde{E}_N(\varphi)^H \cdot \overline{Rs}(\varphi)^{-1} \cdot \tilde{E}_N(\varphi)} \right)^H \cdot \tilde{S}(\varphi) \right|^2 \tag{3.9}$$

Thus, a complete power spectrum estimate is obtained by evaluating (3.9) in M frequency points φ_0, φ_1,..., φ_{M-1}. The estimate requires $T = N + L - 1$ PRIs (i.e. elements of $\tilde{Y}(l)$): the covariance nucleus, corresponding to N PRIs, affects the spectral and temporal resolution, while the number of averaging segments, L, affects the robustness.

As it can be noticed in (3.9), for a complete PSD assessment it is necessary to invert the autocovariance matrix $\overline{Rs}(\varphi)$ at each frequency point φ. This is a pretty hefty task from the computational point of view since $\overline{Rs}(\varphi)$ is an N-*by*-N complex matrix. This is the main obstacle for a real-time implementation of the method and so it is crucial to find a way for an easier, but at the same time efficient, matrix inversion.

3.2.2. Matrix inversion

Matrix manipulations are widely used in many signal processing, communication and parameter optimization algorithms. More often these algorithms include the problem that we have to cope with: solving a matrix inversion.

Since $\overline{Rs}(\varphi)$ depends on φ, a direct implementation of equation (3.9) would require the calculation of a matrix inversion for each frequency point φ. This excessive load can be avoided applying the *Woodbury matrix identity* [21], also known as *matrix inversion lemma*, to equation (3.8):

$$\overline{Rs}(\varphi)^{-1} = \overline{Ry}^{-1} + \frac{\overline{Ry}^{-1}\tilde{S}(\varphi)\tilde{S}(\varphi)^H\overline{Ry}^{-1}}{1 - \tilde{S}(\varphi)^H\overline{Ry}^{-1}\tilde{S}(\varphi)} \tag{3.10}$$

In (3.10) $\overline{Rs}(\varphi)^{-1}$ is obtained from $\overline{Ry}^{-1}$, which, not depending on φ, can be inverted once and used for PSD computation in all of the M frequency points. Thus the task is now to find an efficient method for inverting the autocovariance of the input signal matrix.

Matrix inversion methods can be divided into two main categories: *iterative* and *direct*. The latter typically computes the solution in a finite number of operations. The iterative methods, in turn, do not find an exact solution in finite time but they converge to a solution asymptotically. Iterative methods require an initial estimate of the solution and subsequent update of the estimate, based on the previous estimated error.

What we did is to investigate these two categories for matrix $\overline{Ry}$ inversion. In particular, we have considered and tested the *Newton's iteration* as iterative methods, while our attention has been addressed to the *Cholesky decomposition* among the direct ones.

Newton's iteration for matrix inversion

The Newton iterative method for matrix inversion [25], [26] is an extension of the Newton method used for locating the roots of a function $f(X)$. According to this procedure, the generic step i of the iterative process is:

$$X_i = X_{i-1} - \frac{f(X_{i-1})}{f'(X_{i-1})} \tag{3.11}$$

Since the inverse of the complex matrix $\bar{A}$ can be expressed as the root of:

$$f(\bar{X}) = \bar{A} - \bar{X}^{-1} \tag{3.12}$$

the generic step i for approximating the inverse of $\bar{A}$ is:

$$\bar{X}_i = \bar{X}_{i-1} \left(2\bar{I} - \bar{A} \cdot \bar{X}_{i-1} \right) \tag{3.13}$$

with $\bar{I}$ denoting the identity matrix. Thus, the generic step i requires 2 matrix multiplications and one subtraction.

An initial matrix $\bar{X}_0$, that somehow approximates the matrix $\bar{A}$, is necessary at the beginning of the iteration. Starting with a reasonable approximation of $\bar{A}^{-1}$ is of great importance, since the method has a fast quadratic convergence if $\|\bar{A} \cdot \bar{X}_0 - \bar{I}\| < 1$, where $\|x\|$ is the norm of x. As proposed in [25], we used:

$$\bar{X}_0 = \frac{\bar{A}^T}{2^{n+1}} \tag{3.14}$$

where 2^n is the number of columns and rows of the square matrix $\bar{A}$. The iteration ends when the $\bar{X}_i$ is a satisfactory approximation of $\bar{A}^{-1}$, i.e. when:

$$\|\bar{A} \cdot \bar{X}_i - \bar{I}\| < Th \tag{3.15}$$

where Th is a suitable threshold.

Cholesky decomposition for matrix inversion

As previously said, the direct methods for matrix inversion include the *Cholesky decomposition* [27].

Any non-singular, symmetric, and positive definite matrix $\bar{A}$ (N-by-N) can be factorized using the *Cholesky decomposition* into the following form:

$$\bar{A} = \bar{L} \cdot \bar{L}^T \tag{3.16}$$

where $\bar{L}$, called the *Cholesky factor of $\bar{A}$*, is a lower-triangular matrix and $\bar{L}^T$ is the transpose of $\bar{L}$. This factorization is sometimes referred to as "*taking the square root*" of the matrix $\bar{A}$. The components of $\bar{L}^T$ are of course related to those of $\bar{L}$ by:

$$l_{ij}^T = l_{ji} \tag{3.17}$$

Writing out equation (3.20) in components, we readily obtain:

$$l_{ii} = \left(a_{ii} - \sum_{k=1}^{i-1} l_{ik}^2 \right)^{1/2} \tag{3.18}$$

and:

$$l_{ji} = \frac{1}{l_{ii}} \left(a_{ij} - \sum_{k=1}^{i-1} l_{ik} l_{jk} \right) \quad j = i+1, i+2, \dots, N \tag{3.19}$$

Further, the inverse matrix of a symmetric and positive definite matrix can be found as follows. After matrix decomposition, we solve the inverse of the lower-triangular matrix $\bar{L}^{-1}$, and finally we compute the inverse of $\bar{A}$ by multiplying:

$$\bar{A}^{-1} = \bar{L}^{-1} \cdot (\bar{L}^{-1})^T \tag{3.20}$$

3.3. DSP implementation

3.3.1. Implementation with the Newton's iteration

As shown in equation (3.10), the autocovariance of the noise can be written in terms of autocovariance of the input signal eliminating the dependency from the frequency φ. An additional step can be done writing the formula (3.10) as follow:

$$\overline{Rs}(\varphi)^{-1} = \overline{Ry}^{-1} + \frac{\overline{Ry}^{-1} \tilde{S}(\varphi) \tilde{S}(\varphi)^H \overline{Ry}^{-1}}{1 - \tilde{S}(\varphi)^H \overline{Ry}^{-1} \tilde{S}(\varphi)} = \overline{Ry}^{-1} + \frac{\bar{P}(\varphi)}{D(\varphi)} \tag{3.21}$$

Since $\|\overline{Ry}^{-1}\| \ll \left\| \frac{\bar{P}(\varphi)}{D(\varphi)} \right\|$, we could further simplify:

$$\overline{Rs}(\varphi)^{-1} \approx \frac{\bar{P}(\varphi)}{D(\varphi)} \tag{3.22}$$

Thus, using (3.22) in (3.9) we finally have:

$$PSD(\varphi) = \left| \frac{1}{L} \left(\frac{\bar{P}(\varphi) \cdot \tilde{E}_N(\varphi)}{\tilde{E}_N(\varphi)^H \cdot \bar{P}(\varphi) \cdot \tilde{E}_N(\varphi)} \right)^H \cdot \tilde{S}(\varphi) \right|^2 \tag{3.23}$$

that can be further rewritten as:

$$PSD(\varphi) = \left| \frac{1}{L} \left(\frac{\widehat{num}(\varphi)}{den(\varphi)} \right)^H \cdot \tilde{S}(\varphi) \right|^2 \tag{3.24}$$

A preliminary study was carried out in Matlab® (The MathWorks Inc., Natick, MA) in order to identify the critical sections of the procedure and to tune the required math dynamics in all the calculation steps. Fundamental for finding the optimum balance between accuracy and speed, this study led to the algorithm shown in Figure 3.2. The input vector $\tilde{Y}$ holds the acquired 16-bit complex samples, that are immediately normalized to exploit the full dynamics. The covariance matrix, $\overline{Ry}$, is estimated performing 16×16-bit multiplications with 32-bit results. Then, the inverse matrix, $\overline{Ry}^{-1}$, is approximated through the Newton's iteration as described in §3.2.2.
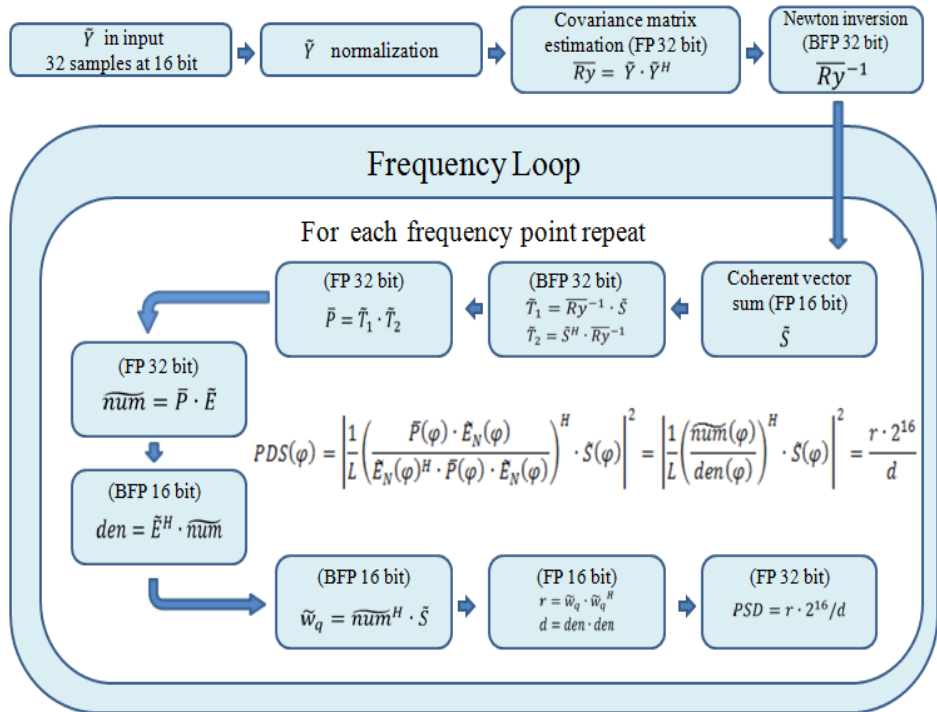

Figure 3.2: The main algorithm steps carried out in Fixed Point (FP) or Block Floating Point (BFP) with the specified number of bits.

We choose a threshold (Th) equal to 0.05 that, on average, produced the convergence in 30 iterations. Block floating point with 32-bit was used here to accommodate the high dynamic generated. Then the loop to be executed for each frequency point φ starts. The coherent vector sum, $\tilde{S}(\varphi)$, is calculated at 16-bit fixed point. Then the matrix $\bar{P}(\varphi)$ is obtained through the 2 intermediate vectors $\tilde{T}_1$ and $\tilde{T}_2$ at 32-bit. The vector $\widetilde{num}$ is obtained at 32-bit, while the scalar den and the vector w_q are calculated in block floating point with 16-bit. The final calculations to obtain the PSD are carried out at fixed point 16-bit.

The APES method has been coded for N=16 and L=17, i.e $L + N-1$=32 PRIs per estimate, and M=128 frequency points linearly distributed in the interval 0÷PRF. This choice, according to previous studies [23], represents the optimal balance between frequency resolution and number of PRIs employed per estimate. In fact a smaller nucleus (lower N) results in an insufficient spectral resolution, while a lower number of averaging segments, L, can produce a non-invertible covariance matrix.

The algorithm has been implemented on the fixed point TMS320C6455-EP™ DSP previously described. The code was written in C and build using the native building tools V.6.031. At each step the assembler generated by the compiler was inspected to verify the effective use of the parallel units of the DSP core. The code was refined until a satisfactory allocation of such units was achieved.

3.3.2. Implementation with the Cholesky decomposition

Let's recall the equation (3.9), here written again for convenience's sake.

$$PSD(\varphi) = \left| \frac{1}{L} \left(\frac{\overline{Rs}(\varphi)^{-1} \cdot \tilde{E}_N(\varphi)}{\tilde{E}_N(\varphi)^H \cdot \overline{Rs}(\varphi)^{-1} \cdot \tilde{E}_N(\varphi)} \right)^H \cdot \tilde{S}(\varphi) \right|^2 \quad (3.9)$$

In §3.2.2 it has been said that the direct implementation of (3.9) is not convenient; moreover, it has been shown how several calculations can be saved by applying the *matrix inversion lemma* (3.10), rewritten below, in order to compute the inversion of the matrix $\overline{Rs}(\varphi)$:

$$\overline{Rs}(\varphi)^{-1} = \overline{Ry}^{-1} + \frac{\overline{Ry}^{-1}\tilde{S}(\varphi)\tilde{S}(\varphi)^{H}\overline{Ry}^{-1}}{1 - \tilde{S}(\varphi)^{H}\overline{Ry}^{-1}\tilde{S}(\varphi)} \qquad (3.10)$$

Let's now use the *Cholesky decomposition* in order to factorize the covariance matrix $\overline{Ry}$ as follows:

$$\overline{Ry} = \bar{P} \cdot \bar{P}^{H} \qquad (3.25)$$

The transpose has been substituted with the *hermitian*, or *conjugate transpose*, since $\overline{Ry}$, and so $\bar{P}$, is a matrix made of complex numbers. We can now impose:

$$\bar{C} = \bar{P}^{-1} \qquad (3.26)$$

so that the inverse of the covariance matrix can be written as follows:

$$\overline{Ry}^{-1} = \bar{C} \cdot \bar{C}^{H} \qquad (3.27)$$

If we define the vectors $\widetilde{Fa}(\varphi)$ and $\widetilde{Fb}(\varphi)$ as follows:

$$\begin{cases} \widetilde{Fa}(\varphi) = \tilde{E}_{N}(\varphi)^{H} \cdot \bar{C} \\ \widetilde{Fb}(\varphi) = \bar{C}^{H} \cdot \bar{Y} \cdot \tilde{E}_{N}(\varphi)^{*} \end{cases} \qquad (3.28)$$

and the scalar quantities:

$$\begin{cases} b(\varphi) = \widetilde{Fa}(\varphi) \cdot \widetilde{Fa}(\varphi)^{H} \\ c(\varphi) = \widetilde{Fa}(\varphi) \cdot \widetilde{Fb}(\varphi) \\ d(\varphi) = \widetilde{Fb}(\varphi) \cdot \widetilde{Fb}(\varphi)^{H} \end{cases} \qquad (3.29)$$

using the factorization (3.27) in equation (3.10) and the result in (3.9), after some computations [22] we obtain:

$$PSD(\varphi) = \left[\frac{c(\varphi)}{b(\varphi) \cdot [L - d(\varphi)] + |c(\varphi)|^{2}} \right]^{2} \qquad (3.30)$$

that is just a different way of writing the Power Spectral Density according to APES method. Hence, after the matrix multiplication $\bar{H} = \bar{C}^{H} \cdot \bar{Y}$, $\widetilde{Fa}(\varphi)$ and $\widetilde{Fb}(\varphi)$ can be efficiently calculated by $2N$ FFT, i.e one for each column of $\bar{C}$ and $\bar{H}$. Thus, according to this approach, APES basically needs a matrix factorization and inversion ($\bar{C}$), a matrix multiplication ($\bar{H}$) and $2N$ FFT at M points.

The APES method obtained as described so far has been coded for $N=L=16$, i.e $L + N - 1 = 31$ PRIs per estimate, and $M=128$ frequency points linearly distributed in the interval $0 \div$ PRF.

According to a preliminary study carried out in Matlab®, the calculations have been implemented in 32-bit fixed-point math, with multiplications and accumulations at 64 bit in almost every step. Figure 3.4 reports the main stages of the procedure.

The input vector $\tilde{Y}$ holds 31 demodulated complex samples represented at 16+16bit. The algorithm starts estimating the 16×16 covariance matrix $\overline{Ry}$, which is saved at 32bit. The *Cholesky decomposition* is then applied to $\overline{Ry}$ in order to obtain the lower triangular matrix $\bar{P}$, stored at 32+32bit. Since several square roots should be calculated for the decomposition, we have coded a specific Newton-based algorithm for square root estimation adjusted to employ divisions with power of 2 divisors only. In the next step $\bar{P}$ is inverted. This is a relatively easy task, being $\bar{P}$ triangular. The resulting matrix $\bar{C}$, represented with 32+32bit, is then multiplied by the matrix $\bar{Y}$ composed by segments of the input signal. The 16 columns of $\bar{C}$ and the 16 columns of $\bar{H}$ are padded with (128–16)=112 zeroes. The 32 padded vectors are processed through 128-point FFTs to obtain $\widetilde{Fa}$ and $\widetilde{Fb}$, saved at 32+32bit and 16+16bit, respectively. An optimized 32+32bit FFT code distributed by Texas Instruments in the DSPLib was used here. In the last step, the coefficients $b(\varphi)$, $c(\varphi)$ and $d(\varphi)$ are calculated at 32+32bit and the PSD is finally obtained.
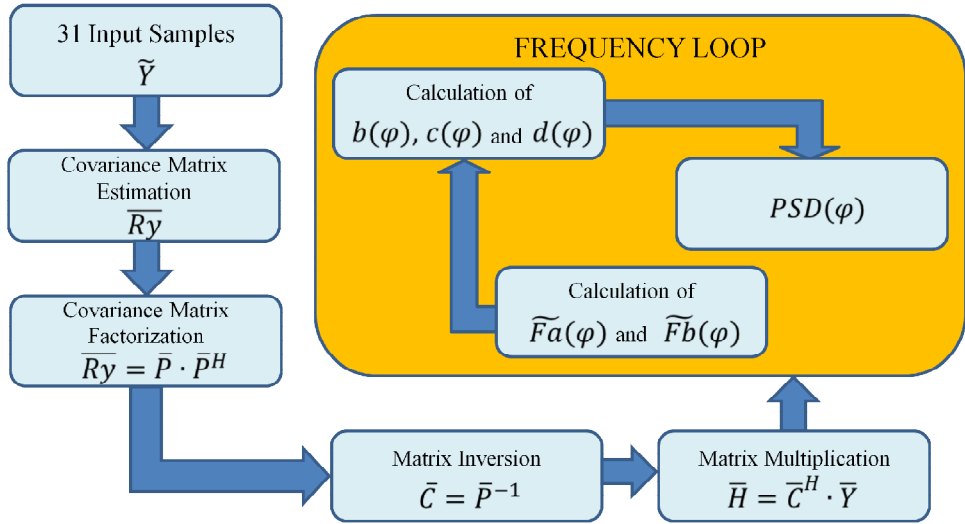
Figure 3.4: The main algorithm steps for the APES implementation on the DSP using the Cholesky decomposition for matrix inversion.

3.4. Results

3.4.1. Implementation with the Newton's iteration

Thanks to the careful code optimization, the most intensive operations like the matrix multiplications are executed by exploiting the DSP parallelism with 7 simultaneous operations per clock cycle on average. This led to the performance listed in Table 3.1. A single iteration of the Newton method runs in about 0.11ms. The matrix inversion, which involves, on average, 30 iterations, occurs in 3.3ms. Since it takes 12µs for a loop iteration necessary to calculate a frequency point, a 128-point spectrum is obtained in 1.5ms. The operations before the frequency loop, e.g. the covariance matrix calculation, have little influence, so that an overall APES spectrum estimate on 128 frequency points is achieved in 3.3ms+1.5ms=4.8ms, which correspond to more than 200fps (*frame per second*).

Operation	Clock	Time [ms]
Single iteration of Newton method	$1.1 \cdot 10^5$	0.11
Matrix inversion (based on 30 iterations)	$3.3 \cdot 10^6$	3.3
Single frequency loop iteration	$1.2 \cdot 10^4$	0.012
128 frequency loop iterations	$1.5 \cdot 10^6$	1.5
PSD calculation on 128 frequency points	$< 5 \cdot 10^6$	**< 5**

Table 3.1: Execution time results.

The proposed method has been tested on data acquired by the ULA-OP research scanner [5], [6] from the common carotid artery of a volunteer. The acquired data were processed both by the DSP, according to the proposed algorithm, and in Matlab® through the floating point APES method using the results of the latter as a reference. Figure 3.3 compares the *spectrograms* calculated by the DSP (top) with the reference (centre). The error, i.e. the absolute difference between the two *spectrograms*, is reported on bottom using a more sensitive scale (–20dB down to –100dB). The mean error is lower than 0.2%.
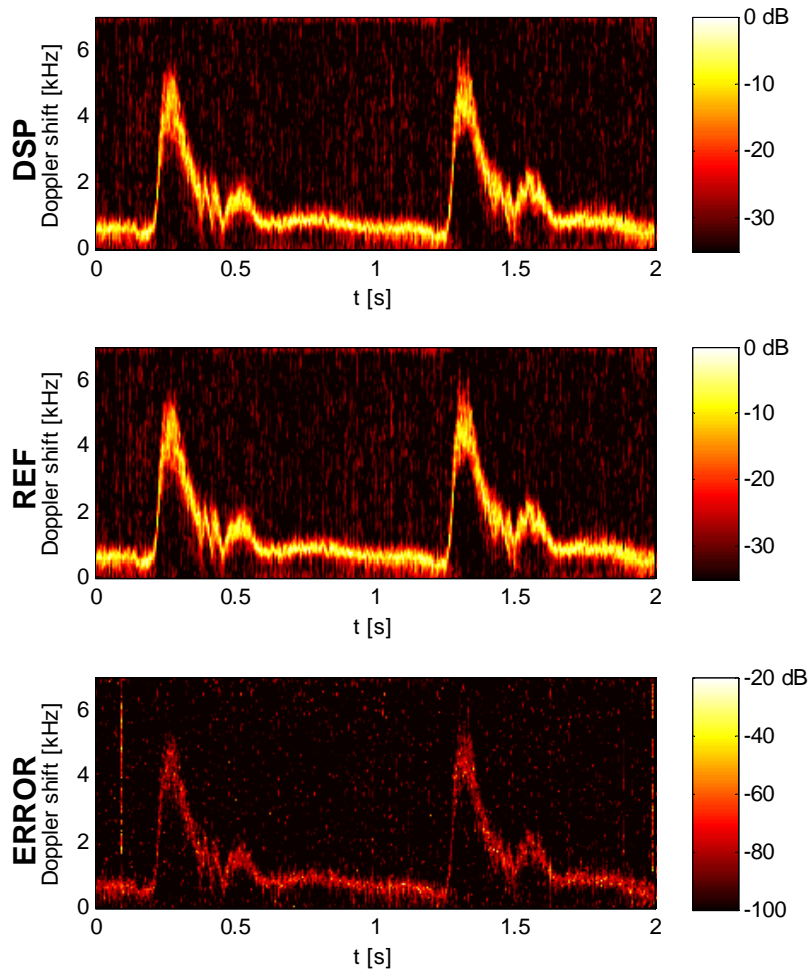
Figure 3.3: Spectograms obtained by investigating the common carotid artery of a volunteer, calculated by the DSP (top) and Matlab® (centre). The absolute difference is reported on bottom on a $-20 \div -100$dB scale.

Thus far we presented an implementation of the APES method on a fixed point DSP that carries out a PSD estimate on 128 frequency-point in less than 5ms. This means that the frame rate attainable in real-time applications is up to 200fps. The availability on the market of DSPs with up to 8 C64x+™ cores used to run the presented implementation allows an 8-fold drop in the time needed for an estimate calculation. In such a case, the real-time application of APES on Multigate-Spectral-Doppler, can be feasible.

The fixed-point math could be an important and potential source of error. In particular we found that a 16-bit fixed point number approximation was not sufficient for accommodating the wide dynamics generated by APES when processing medical signals. The use of 32-bit fixed-point and, when needed, block floating point, allowed to obtain an error lower than 0.2% with respect to the floating point Matlab® reference implementation.

3.4.2. Implementation with the Cholesky decomposition

Thanks to careful code optimization, the most intensive operations are executed with 7 simultaneous operations per clock cycle on average. This leads to the performances listed in Table 3.2. The reported calculation steps have a similar calculation effort, in the order of 10^4 clock cycles per step. An overall APES spectrum estimate on 128 frequency points occurs in less than $12 \cdot 10^4$ clock cycles, corresponding to less than 120µs when the DSP runs at 1GHz.

Operation	Clock	Time [µs]
Covariance estimate	$21 \cdot 10^3$	21
Matrix factorization	$22 \cdot 10^3$	22
Matrix inversion	$7 \cdot 10^3$	7
Matrix multiplication	$15 \cdot 10^3$	15
$\widetilde{Fa}$ and $\widetilde{Fb}$ calculation (32 FFT)	$34 \cdot 10^3$	34
$b(\varphi), c(\varphi), d(\varphi)$ and PSD calculation	$17 \cdot 10^3$	17
PSD calculation on 128 frequency points	**$116 \cdot 10^3$**	**116**

Table 3.2: Execution time results.

The ULA-OP scanner was used to test the proposed implementation. The common carotid artery of a volunteer was investigated with a typical

echo-Doppler set-up. The probe was positioned with the help of the B-Mode imaging and sonograms were displayed in real-time. Several seconds of raw data were saved to be analysed in post-processing.

In the first test, the accuracy attainable by the proposed DSP implementation has been checked by comparing the spectra calculated by the DSP to a reference spectra obtained by processing the same input data in double precision in Matlab®. For example, Figure 3.5 reports, on top, a typical Doppler spectrum calculated by the DSP and, on bottom, the difference with respect to the reference.
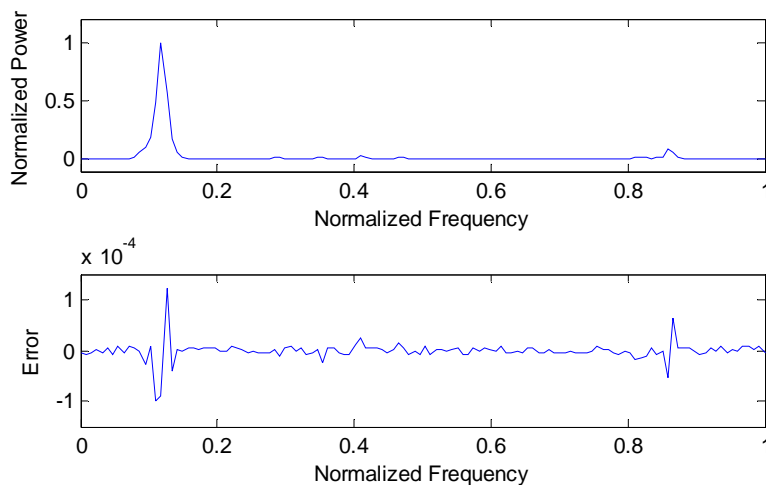
Figure 3.5: Exemple of power spectrum calculated by DSP (top) and its error with respect to the reference calculated in Matlab® (bottom).

The Signal to Noise ratio (S/N), i.e. the ratio between the power of the reference spectra and the power of the error, calculated over more than 3000 spectra, was, on average, S/N=63dB.

In the second test, about 4s of sonogram have been reconstructed in Matlab® from the saved data through the floating-point APES method and compared to the corresponding spectrogram calculated by the DSP. Figure 3.6 compares the spectrograms calculated by the DSP (top) with the reference (centre). The greyscale covers a 35dB dynamic range. Both the implementations produce a high-quality spectrogram and no difference is visible between the two over the reproduced dynamic range.
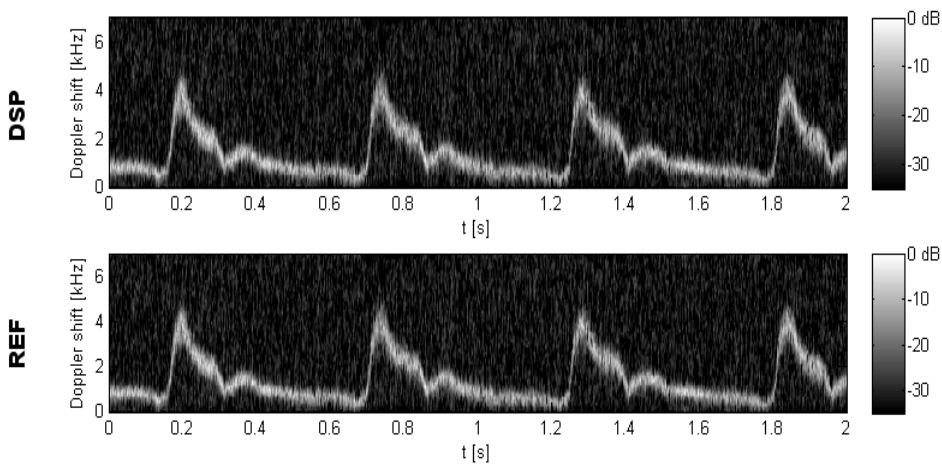
Figure 3.6: Spectrograms obtained by investigating the common carotid artery of a volunteer, calculated by the DSP (top) and Matlab® (bottom).

Figure 3.7, instead, shows the ULA-OP real-time software displaying two spectrograms obtained from the signal coming from the carotid artery of a healthy volunteer.
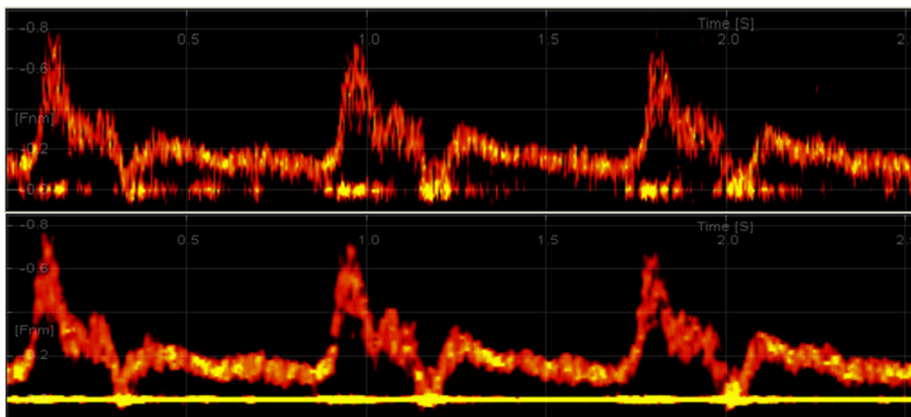
Figure 3.7: ULA-OP real-time software display of two sonograms relating to the signal coming from the carotid artery of a healthy volunteer. On top, the sonogram obtained through the APES method with 31 samples; on bottom, the sonogram obtained through the conventional approach (FFT) using 128 samples.

The figure is arranged so that a visual comparison between the 31-samples-APES spectrogram and the 128-samples-FFT spectrogram can be

done. No substantial differences can be noticed between the two spectrograms except for a smoother appearance in the conventional FFT sonogram. A smaller contribution from the *clutter* can instead be noticed on the APES spectrogram.

3.5. *Results Comparison*

In this chapter an implementation of the APES method on a fixed-point DSP for the real-time elaboration of echo-Doppler biomedical signals has been presented. The DSP is the TMS320C6455-EP™ present on-board of the ULA-OP system. Since the crucial point of the method consists of inverting the complex matrix $\overline{Ry}$, two different techniques for this purpose has been studied and tested.

The implementation of the APES method using the *Newton's iteration* for the inversion of $\overline{Ry}$ produces a PSD estimate on 128 frequency-point in less than 5ms. This means that the frame rate attainable in real-time applications is up to 200fps. The use of 32-bit fixed-point and, when needed, block floating-point, allowed to obtain an error lower than 0.2% with respect to the floating point Matlab® reference implementation.

On the other hand, the code based on the *Cholesky decomposition* for inverting $\overline{Ry}$ and FFT for coefficients calculation can produce a 128-point spectrum estimate in about 120μs. The elaboration of a spectrogram employs, at 100fps, about 1% of the DSP calculation power, leaving wide power for concurrent elaborations like B-mode and/or Color Doppler images. This last implementation features a S/N of 63dB compared to a reference APES elaboration carried out in double precision. The good performance is confirmed by the sonogram comparison reported in Figure 3.6 and Figure 3.7 which shows no visible differences with respect to the reference.

The availability on the market of DSPs with up to 8 C64x+™ cores allows an 8-fold drop in the time needed for an estimate calculation. In such a case, the real-time application of APES based on a reduced number of PRIs, can be valuable for several applications, like, for example, vector Doppler or volume flow assessment.

Chapter 4.   NOVEL DOPPLER METHOD FOR BLOOD PEAK VELOCITY DETECTION

In this chapter a general method for deriving the Doppler power spectrum, limited to the simplest, ideal flow conditions, is presented. The method allows an accurate and easy assessment of the maximum velocity for a laminar flow, independent from noise level and with no need for broadening compensation.

4.1. Introduction

The peak velocity of blood flowing in human arteries has significant importance in the current clinical practice. Knowing the maximum blood velocity is useful for physicians in order to diagnose the potential presence of stenosis and/or thrombus that determines a reduction of the vessel lumen. A prompt diagnosis is important in order to avoid the risk of possible complications, such as ictus or strokes, which in the worst case could be lethal. So the blood peak velocity represents one of the main parameters evaluated to decide about the need of surgery [28].

The echo Doppler ultrasound represents the main investigation method for hemodynamic assessment, but unfortunately, the peak velocity is not easily detectable For example, as explained in Chapter 1, §1.5, the Doppler spectrum of the backscattered signal shows a widening due to the *Intrinsic Spectral Broadening* (ISB), the high-frequency components smeared, so the spectrum slopes down to merge with the noise floor. Thus, which is the Doppler frequency of the spectrum related to the blood peak velocity?

At present, heuristic methods are used to find the crucial highest frequency, usually by choosing the Doppler frequency that crosses a power threshold set in relation to the noise power level, or as a percentage of total spectral power. However, the detected frequency must then be compensated for spectral broadening by a factor that depends on the transducer geometry and the Doppler angle [4], [29], [30], [31]. Such heuristic methods provide peak velocities that vary for differing signal-noise levels and transducer configurations, and therefore provide unreliable velocity determinations [32].

In this chapter a new Doppler method for blood peak velocity detection is presented. Based on a mathematical model for describing the Doppler spectrum, the method predicts the exact location of the Doppler frequency f_{d_P} related to the maximum velocity of the blood (v_P). According to this model, v_P can be directly and accurately calculated without the need of broadening compensation by the Doppler equation (1.21), shown below for convenience's sake:

$$v_P = \frac{c f_{d_P}}{2 f_t \cos \theta} \qquad\qquad (1.21)$$

4.2. Doppler Spectrum Model

The novel method is based on a model that can be applied to both CW and PW Doppler investigations. For simplicity, we first derive the Doppler spectrum for the CW mode, and then we discuss how PW should be implemented for the model to be valid.

Let's consider the configuration shown in Figure 4.1, where a flow with parabolic velocity distribution travels through a vessel of diameter $2R$. A transducer, producing a continuous ultrasound beam of wavelength λ, insonates the aforementioned flow.
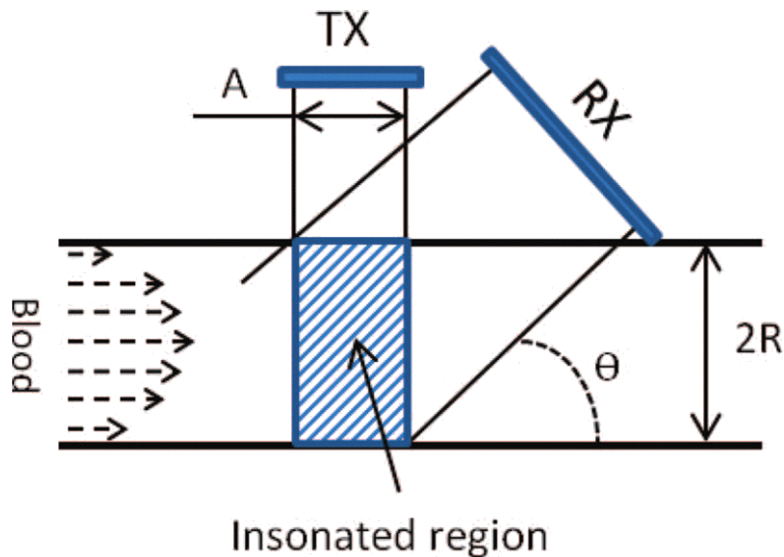
Figure 4.1:Configuration used for determining the Doppler spectrum according to the novel method.

A second transducer, placed at angle θ with respect to the flow direction, receives the echoes from all of the moving scatterers. The transducers are arranged so that all flow components travelling through the cylindrical tube region of length A are insonated, and backscattered signals generated from all of the flow components are received.

71

The received echo signal is processed with the usual Doppler approach [1]; i.e. it is coherently demodulated to in-phase and quadrature (I/Q) components, low-pass filtered, and then sampled at rate f_s. The signal is observed for T_0 seconds, so that $N = T_0 \cdot f_s$ samples are acquired. The Doppler power spectrum, calculated through the classic FFT [1], consists of N bins centred at frequencies $f_n = n \cdot f_s/N = n/T_0$. According to the Doppler equation (1.20), the Doppler spectrum bin-width $(1/T_0)$ corresponds to a velocity resolution v_s defined as follows:

$$v_s = \frac{c \cdot f_s}{f_t \cos \theta} \cdot \frac{1}{N} = \frac{c}{T_0 f_t \cos \theta} = \frac{\lambda}{T_0 \cos \theta} \qquad (4.1)$$

Thus, the velocity quantization is inversely proportional to the observation time T_0 and the angle θ, while it is directly proportional to the wavelength λ.

4.2.1. Quantizing the velocities in the flow

The continuous distribution of velocities present in the flow is approximated by a group of M discrete *shells of fluid*, as shown in Figure 4.2, each having a constant velocity. The velocity quantization step is equal to the Doppler velocity resolution v_s.
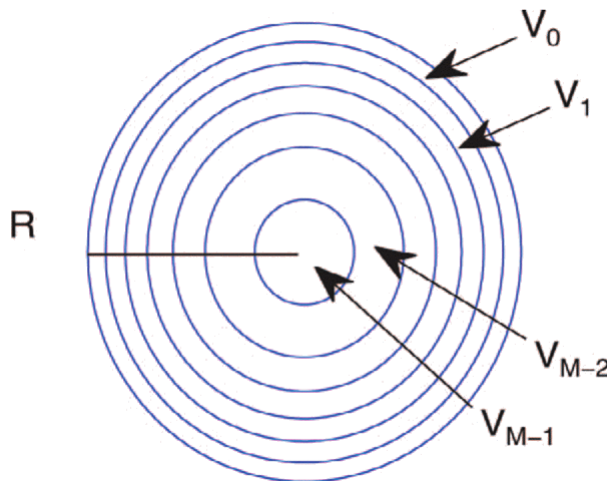

Figure 4.2: The quantization of fluid flow into discrete velocity shells.

The total flow is approximated by the sum of the flows in the M shells of Figure 4.2, where:

$$M = \left\lceil \frac{v_P}{v_s} \right\rceil \tag{4.2}$$

The symbol $\lceil \cdot \rceil$ represents the first integer larger than the argument. The fluid in the m-*th* shell moves at velocity v_m, defined as follows:

$$v_m = (m + 0.5) \cdot v_s \tag{4.3}$$

It should be noticed that M must be less than $N/2$ according to the *Nyquist limit*.

4.2.2. Doppler spectrum from a velocity shell

Considering Figure 4.1, a blood cell moving in the m-*th* shell at velocity v_m is insonified by the ultrasound excitation for as long as it is travelling in the insonified region of length A. During this time, the cell produces a sinusoidal echo burst, A/v_m seconds long, characterized by a frequency shift (f_m). The shift is related to the cell velocity by the Doppler equation:

$$f_m = \frac{v_m \cos\theta}{c} f_t \tag{4.4}$$

This echo is collected by the receiver during the observation time T_0, which is randomly phased with respect to the start of the echo produced by the blood cell. In general, a cell echo received by the receiver for w_m samples, i.e. for time length of w_m/f_s seconds, produces a sinc^2 power spectrum that corresponds to a sinusoidal burst of frequency f_m multiplied by a rectangular window of w_m/f_s length [33]. In particular, the shorter the observation time, the wider the frequency extension of the received pulse. The i-*th* bin of the Fourier transform of the normalized Doppler power produced by that cell, denoted with P_i, is equal to:

$$P_i(f_m, w_m, N) = \left(\frac{w_m}{N}\right)^2 \text{sinc}^2 \left[|f_m - i| \frac{w_m}{N} \pi \right] \tag{4.5}$$

Note that, as previously stated, the spectral contribution is centred on f_m but extends over surrounding frequency bins, depending on the length of the pulse, w_m.

The model for the total Doppler power spectrum is obtained by summing the contributions of the pulses generated by all of the blood cells moving at their quantized velocities in the M velocity shells, as detailed in the next section.

4.2.3. Slow shells and fast shells

In some shells, the velocity is low enough that a portion of that shell's blood cells can remain within the insonated aperture A during the entire observation period T_0. In other words, this happens when the shell velocity is:

$$v_m < \frac{A}{T_0} \qquad (4.6)$$

Shells characterized by a velocity that meets the condition (4.6) are called *slow shells*. On the other hand, those shells in which the blood cells are moving fast enough to traverse the insonated aperture in less than the observation time T_0, i.e. where (4.6) is not met, are called *fast shells*.

Slow blood cells that remain in the insonated area for an interval T_0 (see, for example, the p_{sa} cell in Figure 4.3) produce a pulse of $P(f_m, N, N)$, i.e. a pulse whose width is equal to the observation time.

In the insonated area there are also cells that, despite their low velocity, leave the insonated area, during the observation time T_0. This is because of their position within the aperture when the observation interval begins. An example is given by the p_{sb} cell in Figure 4.3, i.e. a cell near the exit end of the aperture. These cells produce pulses shorter than the observation period.

The cells that are just at the edge of the insonated area will leave during the time from 0 to the first of the N samples, and will therefore generate a Doppler pulse of width 1, i.e. a pulse described as $P(f_m, 1, N)$; the cells slightly further away from the edge will produce a pulse of $P(f_m, 2, N)$, and so on.

Since the flow is assumed continuous, for every cell that exits, another enters; for instance, the cell that was just outside the insonated area at the beginning of the observation period will enter between 0 and the first sample (see, for example, the p_{sc} cell in Figure 4.3) and will generate a

pulse $P(f_m, N-1, N)$. Similarly, a cell slightly farther away from the insonated area will produce a pulse of width $N-2$, and so on. Therefore, cells leaving and cells entering produce complementary pulses.
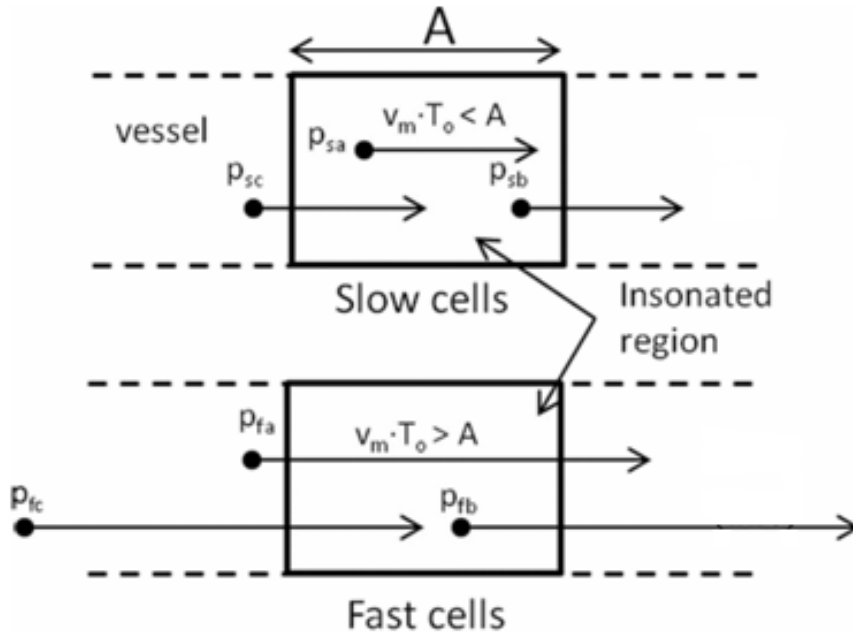
Figure 4.3: Every blood cell (dark circle) crossing the insonated region (boxed area) is considered slow if the distance travelled during the T_0 interval (arrow length) is lower than A (top), otherwise it is fast (bottom). The spectrum is obtained by summing the contributions of: (a) slow cells insonated for the whole T_0 interval (p_{sa}), (b) fast cells insonated for their travelling time (p_{fa}), (c) slow and fast cells which enter and exit the insonated area during T_0 (p_{sb}, p_{sc} and p_{fb}, p_{fc}, respectively).

Denoting the number of blood cells per unit length in the m-*th* shell as ρ_m, the total number of cells in a shell along the aperture A is $\rho_m A$; the number of cells that leave the insonated area, and which also enter, will be $\rho_m \cdot v_m \cdot T_0$. Therefore, for a *slow shell* of index m, the total contribution to the Doppler spectrum from all of its cells is the sum of SS_{a_m} and SS_{b_m}:

$$\begin{cases} SS_{a_m} = \rho_m(A - v_m T_0)P(f_m, N, N) \\ SS_{b_m} = \dfrac{2v_m\rho_m T_0}{N}\displaystyle\sum_{j=1}^{N-1} P(f_m, j, N) \end{cases} \qquad (4.7)$$

The cells that remain in the shell m-*th* for the entire observation period T_0 generate the SS_{a_m} contribution; on the other hand, SS_{b_m} is generated by the cells that leave and enter (see the factor of 2) the insonated area, producing pulses of width ranging from 1 to $N-1$ samples.

A *fast shell*, i.e. in which a cell at the entrance edge of the insonated length will go through the entire insonated area by the end of the observation period, is defined by a velocity $v_m > A/T_0$. We define the transit time for *fast shells* as follows:

$$tt_m = \frac{A}{v_m} \qquad (4.8)$$

Every cell that completely traverses the length A (see, for example, the p_{fa} cell in Figure 4.3) produces a pulse of time duration, in samples, of w_m given by the formula:

$$w_m = tt_m \cdot f_s \qquad (4.9)$$

The number of cells that completely traverse the insonated volume is $\rho_m A[(T_0/tt_m) - 1]$, the -1 arising from cells that were already in the insonated volume during the first transit time. These cells, being partially in the insonated area when the observation period begins (see, for example, p_{fb} in Figure 4.3), produce pulses of length $1, 2, \ldots, w_m - 1$ as they leave the insonated area. Similarly, as the observation period ends, the cells that did not have time to completely traverse the insonated area (see, for example, p_{fc} in Figure 4.3) will produce pulses of length $1, 2, \ldots, w_m - 1$ complementary to those that left the insonated area. Therefore, the Doppler power spectrum from a *fast shell* will be the sum of SF_{a_m} and SF_{b_m}:

$$\begin{cases} SF_{a_m} = \rho_m A \left(\dfrac{T_0}{tt_m} - 1 \right) P(f_m, w_m, N) \\[4mm] SF_{b_m} = \dfrac{2\rho_m A}{w_m} \displaystyle\sum_{j=1}^{w_m-1} P(f_m, j, N) \end{cases} \quad (4.10)$$

where SF_{a_m} are pulses from the cells that completely transit the aperture, and SF_{b_m}, similar to SS_{b_m} of the slow shells, represents the contribution of the cells that did not completely traverse the aperture because they were already in the aperture at the beginning, or entered the aperture before the end of the observation period, so that they did not have time to fully traverse it.

The contribution of the cells in both the *fast* and *slow shells* produces the total spectrum ST:

$$ST = SS_{a_m} + SS_{b_m} + SF_{a_m} + SF_{b_m} \quad (4.11)$$

Defining the *transition shell* between the *slow* and *fast shells*, i.e. the first *fast shell*, as follows:

$$m_t = \frac{A}{T_0} \cdot v_s \quad (4.12)$$

the total Doppler power spectrum can be written as shown below:

$$\begin{aligned} ST = \sum_{m=0}^{m_t-1} & \left[\rho_m (A - v_m T_0) P(f_m, N, N) \right. \\ & \left. + \frac{2v_m \rho_m T_0}{N} \sum_{j=1}^{N-1} P(f_m, j, N) \right] \\ + \sum_{m=m_t}^{M-1} & \left[\rho_m A \left(\frac{T_0}{tt_m} - 1 \right) P(f_m, w_m, N) \right. \\ & \left. + \frac{2\rho_m A}{w_m} \sum_{j=1}^{w_m-1} P(f_m, j, N) \right] \end{aligned} \quad (4.13)$$

Figure 4.4 shows two Doppler power spectra for the assumed parabolic velocity distribution calculated from (4.13) using Matlab® (The MathWorks Inc., Natick, MA).
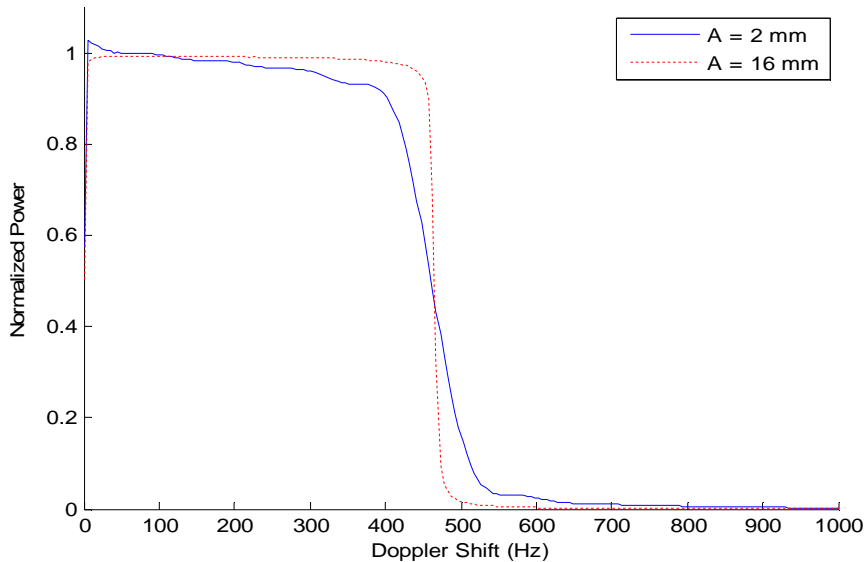

Figure 4.4: Doppler spectra calculated from (4.13) using Matlab® for two different aperture lengths *A*.

The spectra shown in Figure 4.4 have been calculated considering two different values for the length *A*. The other parameters used for the calculation are: λ=0.33mm, *N*=512, f_s=1kHz, θ=46.5°, and T_0=0.5s. The power spectrum shows a *plateau* that extends from lower frequencies to higher frequencies, where a descending slope rapidly leads the spectrum to zero.

Although the model has been derived for CW transmission, its validity is preserved when PW mode is used, provided that the flow is fully insonated. This condition can be obtained by transmitting sufficiently long pulses. For example, 40 cycles at 5MHz cover a region of more than 11mm length, considering *c*=1480m/s. In PW mode, the samples are acquired at the PRF rate, which corresponds to the sampling frequency f_s used in the presented model. The observation window is $T = N/PRF$, where *N* is the number of acquired samples multiplied by the interval

between subsequent transmissions, $1/PRF$. In other words, when the aforementioned conditions are met, CW or PW measurements produce the same Doppler spectrum [34], thus extending the model's validity.

4.3. The Half-power Threshold Rule

The Doppler spectrum expressed by equation (4.13) allows an accurate identification of the threshold to be used for determining the maximum velocity. This threshold is given by the following formula:

$$Th = \frac{ST_P}{ST_F} \tag{4.14}$$

where ST_P is the spectral power in the bin at the frequency corresponding to the peak velocity v_P, and ST_F is the spectral power in the bins in the flat region of the spectrum.

For the assessment of ST_F the following recursive algorithm has been used. An initial power threshold Th_0 is chosen to be above the noise level present at higher frequencies. The spectrum is then scanned from the higher to the lower frequencies until the initial frequency point f_0 is located where the bin power exceeds Th_0. Thereafter, the frequency points f_i and the thresholds Th_i are recursively determined as follows:

$$\begin{cases} f_i = (1 - \alpha) \cdot f_{i-1} \\ Th_i = \frac{1}{f_{i-1} - f_i} \int\limits_{f_i}^{f_{i-1}} S(x)dx \end{cases} \tag{4.15}$$

where Th_i is the average spectral density between the frequency points f_{i-1} and f_i, α is a parameter which affects the dimension of the averaging region, and i is the step index. The procedure quickly converges to the *plateau* level, and stops when $f_i = f_{i-1}$.

Using this procedure, the values of Th have been calculated in Matlab® for different conditions. The parameters tested, listed in Table 4.1, included the insonation length A; the peak velocity v_P, and the observation time T_0. For sake of simplicity, the transmission frequency, $f_t = c/\lambda$, and the Doppler angle θ, were combined into the single parameter k defined as

$k = f_t \cdot \cos\theta$. The number of shells M was selected by equation (4.2), the FFT points, N, was chosen according to the *Nyquist limit*, and the particle density, ρ_m, was normalized to 1.

Parameter	Name	Basic Value	Tested Range
Insonation length	A	10mm	2÷16mm
$f_t \cdot \cos\theta$	k	3.44MHz	1÷10MHz
Peak Velocity	v_P	0.2m/s	0.1÷1m/s
Observation Time	T_0	500ms	10÷1000ms

Table 4.1: Tested parameters.

Each of the parameters listed in Table 4.1 was varied in the range reported in the last column, while the others were held at the constant basic value reported in the third column. Figure 4.5 shows the threshold calculated as the parameters range over the reported intervals. The variation of Th is small and its value is near 0.5 (see red dotted reference line in each sub-pictures) over a large range of parameter variation.
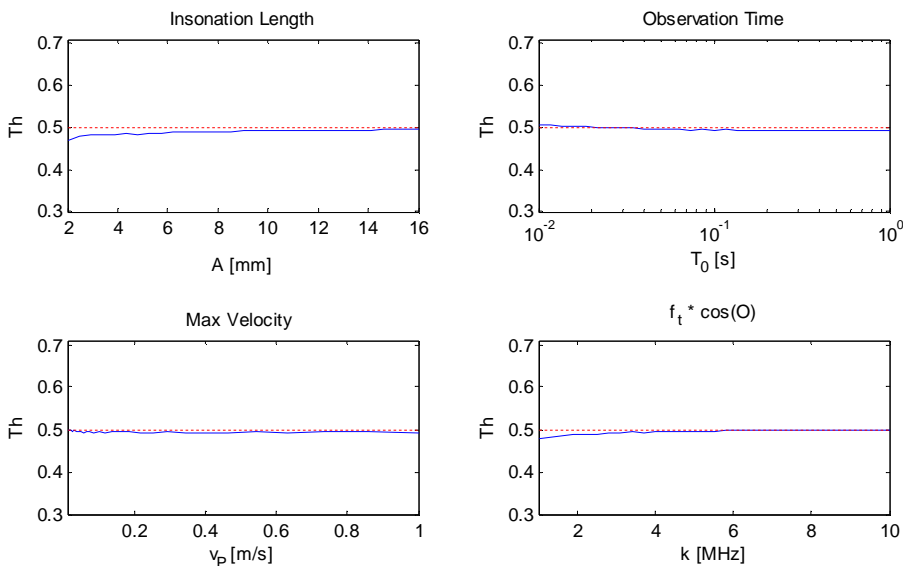

Figure 4.5: Threshold trend (continuous blue line) versus insonation length (top left), observation time (top right), peak velocity (bottom left), and k (bottom right). The red dotted lines represent the 0.5 constant value.

A further confirmation of the validity of the relation between the half-power point and the f_{d_P} is shown in Figure 4.6. It can be noticed how all the modelled spectra derived from the same peak velocity and k, intersect at the half-power point of the slope as the insonation length (Figure 4.6 top) and the observation time change (Figure 4.6 bottom).
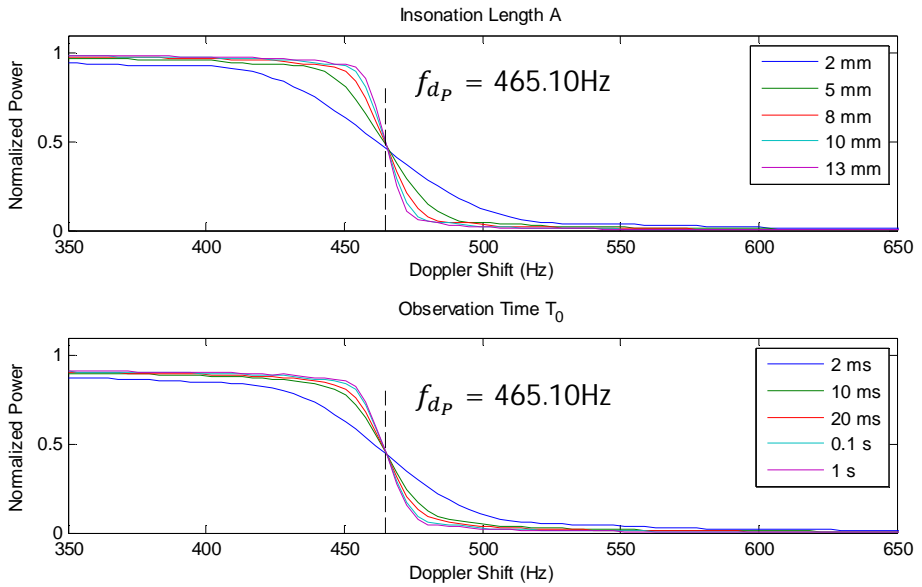
Figure 4.6: Overlapped spectra for insonation length in the range 2÷13mm (top) and observation time in the range 0.002÷1s (bottom). The vertical slashed line represents the Doppler shift.

So we can conclude that, according to the model given by the new method, the threshold Th to be used in order to detect the Doppler frequency related to the peak velocity is equal to 0.5.

4.4. *Experiments*

4.4.1. *Experimental set-up*

The validity of the model has been tested at the MSD Laboratory (Department of Information Engineering, DINFO, University of Florence, Italy) using the set-up depicted in Figure 4.7.

Figure 4.7: Experimental set-up used for validating the method. Hydraulic circuit (a), MCMG board (b), and software management (c).

The hydraulic circuit basically consists of two reservoirs located at different heights and connected by an 8mm-diameter p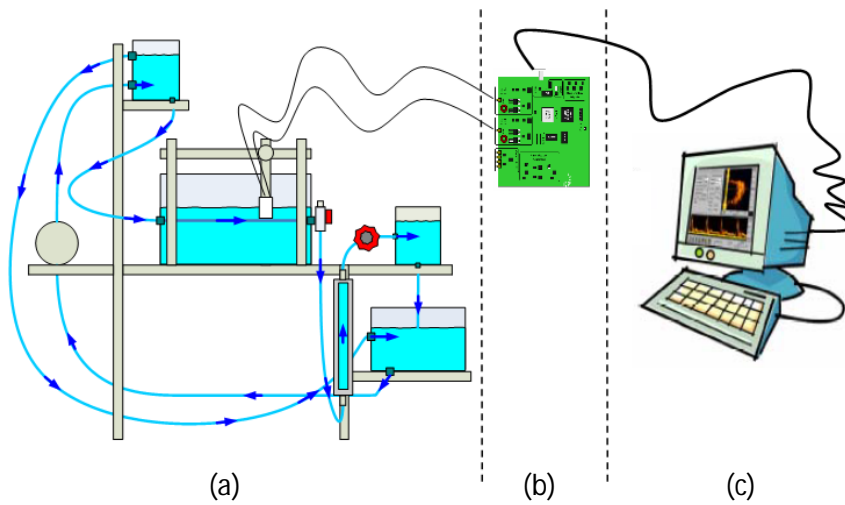ipe (the measuring cell) within which a blood-mimicking fluid, prepared as described in Chapter 2, §2.3.1, flows. A valve is used to regulate the flow and a pump maintains a constant fluid level in the reservoirs. A flowmeter, model E52600 (Asa s.r.l., Sesto S. Giovanni, Italy) with accuracy of ±12ml/min, is also present in the hydraulic circuit for monitoring and annotating the volume flow in each acquisition session.

The experiments were performed using the multigate-multichannel (MCMG) Doppler system [15] connected to a 5MHz probe with a central and three lateral transducers [35]. The MCMG system consists of a digital board specifically designed at the MSD Laboratory for ultrasound research activities, and is capable of controlling two independent ultrasound channels. Each channel could be programmed to work either in standard PW spectral Doppler or in MSD mode. In particular, MSD mode has been used here to check the flow profile and to facilitate coarse probe positioning at the beginning of each measurement session. The MGMG board can process data in real-time and save raw or I/Q demodulated data in a PC file.

The probe, whose configuration is shown in Figure 4.8, features a 14mm-diameter unfocused central element (number 4 in the figure) capable of uniformly insonating the region below for a lateral extension of A=10mm. Three lateral 10×14mm rectangular transducers (indicated with number 1, 2, and 3 in the figure) are placed so that their axes cross the beam produced by the central element at 43.5°. The four beams overlap at 18mm depth in a volume region of about 10×10×10mm.
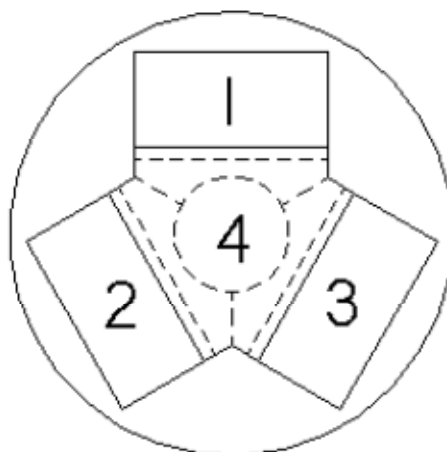
Figure 4.8: Configuration of the probe used for validating the method.

In order to implement the method, only the transmitting central element and, in reception, just one of the three lateral elements have been used. In Figure 4.9 it is sketched this configuration, highlighting the transmission and the reception beams.
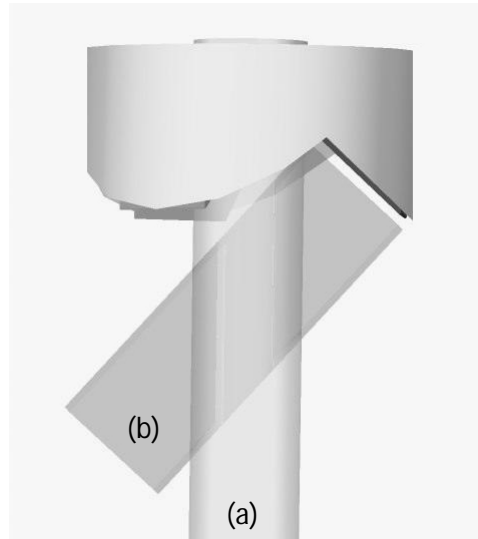
Figure 4.9: Transmission (a) and reception (b) beam for the adopted configuration.

In particular, the central transducer of the probe has been used in PW mode with 500Hz to 2kHz PRF to transmit 40 cycles at 5MHz, so that the generated large sample volume covered the complete pipe diameter, being the corresponding sample volume of about 12mm. In all of the acquisition sessions, the probe has been oriented so that the 8mm-diameter-pipe is aligned with the receiving transducer and perpendicular with respect to the transmitted beam. In this condition, the Doppler angle was 46.5°, corresponding to k=3.44MHz. The probe-pipe distance was regulated so that the pipe crosses the large sample volume generated where the transmitting and the receiving beams overlap.

Moreover, the measuring cell has been calibrated through the equivalent volume of water, described in [36]. In this condition, we estimated an accuracy of the produced reference velocity of about 1%.

A software running on a commercial PC is designated for the management of the multi-gate system. This software, called GASP (*Global Acquisition & Signal Processing*), is made of different modules for the acquisition, the real-time display and the storing of the data coming from the MCMG board. The software, whose main interface is shown in Figure 4.10, lets the user to set parameters like the sampling frequency,

the analog gain, the number of points to be used for calculating the FFT and others.

In each acquisition, about 60s of signal from the angled transducer were acquired, coherently demodulated in complex (I/Q) samples, and saved.
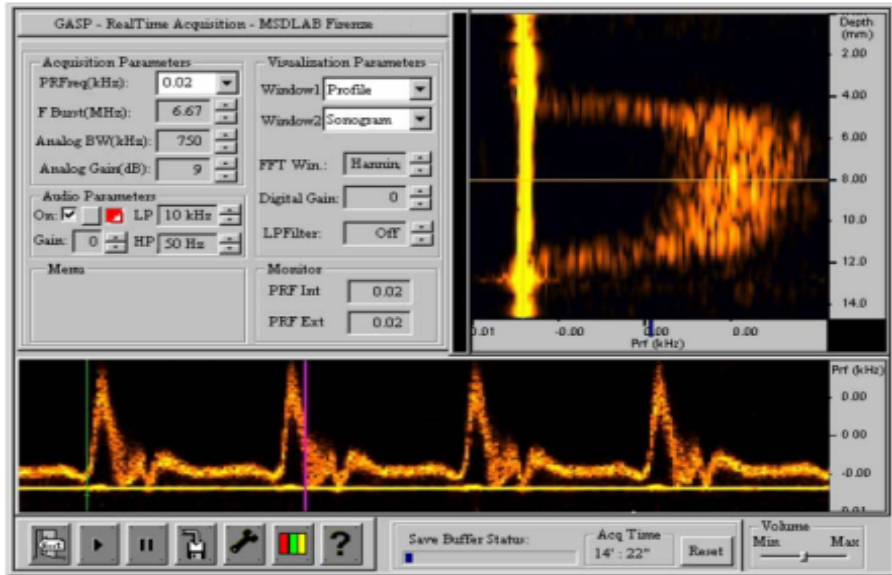
Figure 4.10: GASP software main interface.

4.4.2. Data post-processing

The raw radio-frequency data were coherently demodulated by the MCMG board and the resulting I/Q data were saved in a file and then processed in Matlab® (The MathWorks Inc., Natick, MA). A 50Hz wall filter was first applied and then the power spectral density was estimated according to the *Welch method* [20], as described in Chapter3, §3.1. In this application, a 1024-point FFT, Hanning windowed, with 75% overlap has been used to achieve a spectral resolution of about $1 \div 2$Hz over $1 \div 0.5$s of observation time, respectively. For each flow setting, all spectra obtained from the acquired signal have been averaged. According to the proposed method, ST_P was calculated as $ST_F/2$. A linear interpolation between the 2 FFT bins near ST_P was used to locate the corresponding frequency value f_{d_P}, which was finally converted to the measured peak velocity by the Doppler equation (1.21).

4.5. Results

Figure 4.11 reports an example of spectrum measured in a 200ml/min flow (continuous red line) compared with the model spectrum simulated using the corresponding parameters (dotted blue line). Apart from the wall-filter effects, the main difference between the spectra is in the range 60÷270Hz, where the measured spectrum exhibits lower power density. However, the beginning of the *plateau* in the measured spectrum is easily detectable, and, most important, the spectra overlap almost perfectly in the slope region. The bottom of Figure 4.11 shows a magnification of the slope region to better appreciate the details. The slope region features an extension of only 20Hz, but it is resolved by the high-resolution FFT.
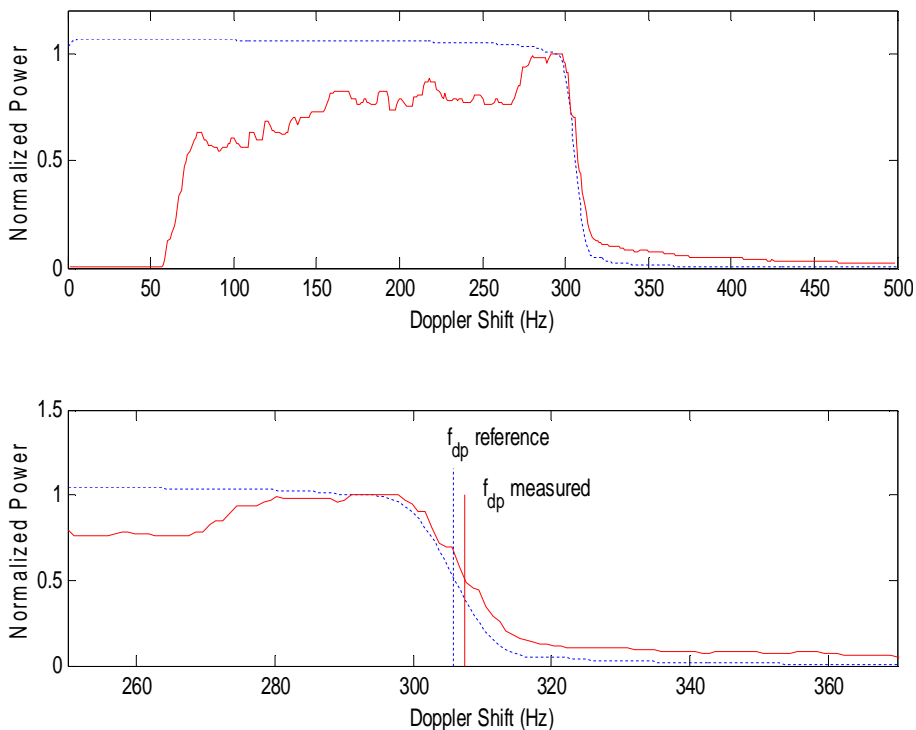
Figure 4.11: Measured Doppler spectrum (continuous red line) compared with the theoretically spectrum (dotted blue line) related to a 200ml/min flow. On bottom, a magnification of the spectra slope zone highlighting the measured and simulated Doppler shifts in continuous red and dotted blue vertical line, respectively.

The measured half-power frequency corresponds to 307.5Hz (continuous red vertical line), to be compared with 305.8Hz corresponding to the reference peak velocity (dotted blue vertical line). The velocity resolution, calculated by equation (4.1) for T_0=1s, is ±0.042cm/s. The result is within the 1% accuracy of the experimental apparatus. For each used flow rate, Q, the measured half-slope frequency was converted to velocity through the classic Doppler equation (1.20) and compared with the reference peak velocity v_P, obtained from equation (1.47).
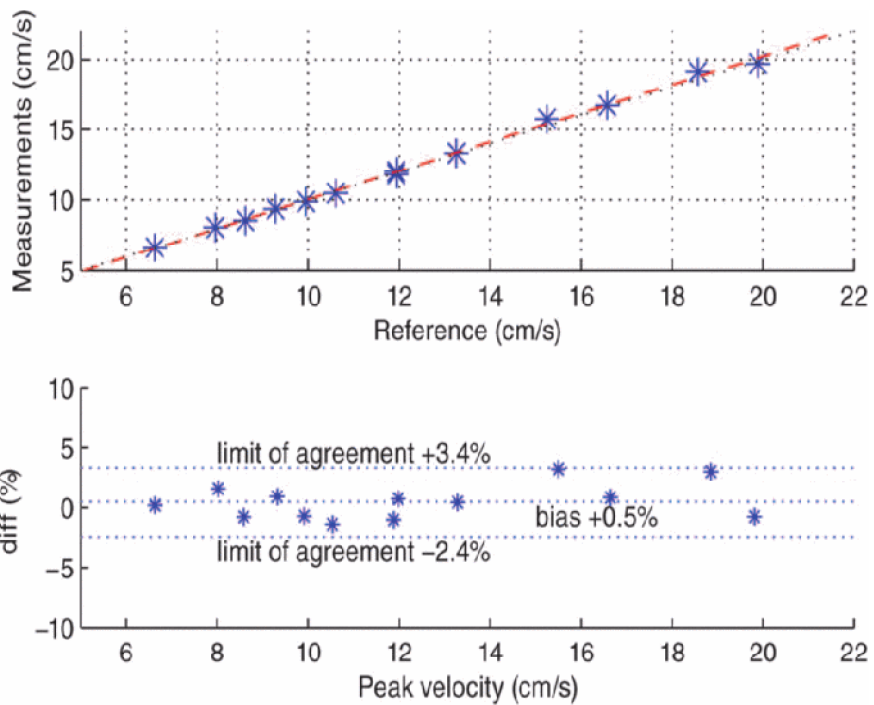
Figure 4.12: Measurements (*) and regression line (red dashed) are compared with identity (black dotted) on top. On bottom, the measurements are compared with the reference with Bland-Altman method.

Figure 4.12 (top) reports the measurements, together with the regression line (dashed red) and the identity line (dotted black). The regression line $a \cdot x + b$, has gain, a, and offset, b, of about 1.04 cm/s and −0.4cm/s, respectively (see Table 4.2).

a	1.021
b	-0.179cm/s
R^2	0.997
Rmse_fit	0.22cm/s
Rmse_fit	0.23cm/s

Table 4.2: Linear regression parameters.

The coefficient of determination, R^2, is very close to 1. *Rmse_fit* and *Rmse_id* represent the root mean square errors (RMSEs) calculated with respect to the regression and identity lines, respectively, and both are quite low. Figure 12 (bottom) reports the *Bland–Altman* [18] analysis of this data. Here, the vertical axis represents the difference between the measurement and the reference, expressed as percentage with respect to the mean value. A +0.5% bias is observed together with the limits of agreement of -2.4%, 3.4%. In these experiments, T_0 was in the range 0.5÷1s, corresponding to a velocity resolution of 0.084÷0.042 cm/s.

The regression analysis highlighted an excellent linearity with practically no slope error ($a\sim1$), whereas *Bland–Altman* analysis reported no error dependence on the flow rate. We found a bias lower than the experimental set-up accuracy ($<1\%$) and all measurement errors were in the range $\pm3\%$.

Chapter 5.   NOVEL METHOD EXTENSION

In this chapter an extension of the model presented in the previous chapter is analysed. The extension, aimed to reproduce a real clinical examination condition, is realized considering non-uniform insonations and non-parabolic flow profiles.

5.1. Introduction

In the previous chapter, it has been presented a general method of deriving the Doppler power spectrum, limited to the simplest, ideal flow conditions. As shown, the method allows an accurate and easy assessment of the maximum velocity for a laminar flow, independent from noise level and with no need for broadening compensation.

Anyway, the theoretical Doppler power spectrum is not consistent with the experiments at all frequencies. The experimental results have shown how the lower frequency portions of the Doppler spectra do not present the full *plateau* visible in the theoretical spectrum. The discrepancy can be mainly attributed to the difficulty in obtaining the full and uniform flow insonation required by the model. The attainable insonation is typically stronger on the central part of the vessel and weaker on the sides, and when the beam axis intercepts the flow axis, this produces lower energy insonating slower scatterers. The result is a reduced amplitude at low frequencies.

Moreover, a typical Doppler ultrasound investigation is carried out in duplex mode using a linear array probe, completely different from the one used for the experiments, longitudinally placed along the vessel [1]. The linear array, through a fixed lens, focalizes the beam in the lateral direction at a static depth, typically in the 15÷25mm range. Thus, the lateral width of the beam is quite narrow and far from being uniform over the vessel lateral extension.

Another critical hypothesis of the model is the parabolic flow. Actual flow in arteries can significantly differ from the ideal parabola [37] showing more complex behaviour like jet and/or helical flow patterns. Moreover, if an artery bends, the central blood flow streams strike the arterial wall resulting in a non-laminar, non-parabolic flow [38].

All this reasons make the model, presented in the previous section, not suitable for the conditions present in a real clinical examination.

We have started from these considerations and have extended the model to the *Gaussian-shaped pressure fields* [39], which can be produced by linear array probes, and to velocity profiles featuring *non-parabolic "power law" shape* [40].

5.2. Doppler Spectrum Extended Model

The extension of the model is obtained from the original theory presented in (4.13) by weighting the contribution of each shell with coefficients P_m and S_m:

$$
\begin{aligned}
ST = \sum_{m=0}^{m_t-1} P_m{}^2 S_m & \left[\rho_m (A - v_m T_0) P(f_m, N, N) \right.\\
& \left. + \frac{2 v_m \rho_m T_0}{N} \sum_{j=1}^{N-1} P(f_m, j, N) \right] \\
+ \sum_{m=m_t}^{M-1} P_m{}^2 S_m & \left[\rho_m A \left(\frac{T_0}{tt_m} - 1 \right) P(f_m, w_m, N) \right.\\
& \left. + \frac{2 \rho_m A}{w_m} \sum_{j=1}^{w_m-1} P(f_m, j, N) \right]
\end{aligned}
\qquad (5.1)
$$

The coefficients P_m and S_m, that we are going to discuss in the following paragraphs, account for non-uniform insonation and for non-parabolic flow, respectively.

5.2.1. Gaussian-shaped insonation

Let's consider a circular vessel, of diameter $2R$, placed in the x, y, z Cartesian system, as shown in Figure 5.1.
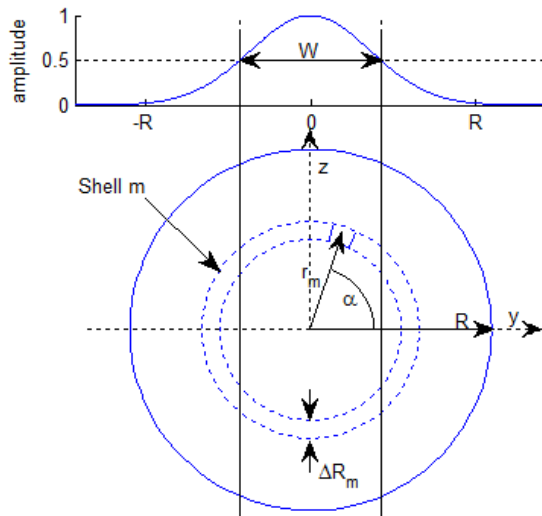
Figure 5.1: A circular vessel of radius R lays with its section in the y-z plane. The flow is divided in shells of constant velocity v_m running in the x direction (perpendicular to the page). The vessel is insonified by a beam that has uniform amplitude in x and z directions and features a Gaussian amplitude of width W along the y direction.

Let's assume that the vessel is insonated by a beam with uniform amplitude along the x and z directions. On the contrary, in the elevation direction y, the beam features the Gaussian profile given by the following formula:

$$G(y) = \exp\left(\frac{-y^2}{2\sigma^2}\right) \tag{5.2}$$

where $\exp(\cdot)$ is the exponent of the Euler's number e. Considering the beam width W, calculated between the half-amplitude points, as shown in Figure 5.1, we have:

$$\sigma^2 = \frac{W^2}{8 \cdot \ln(2)} \tag{5.3}$$

The shell at distance r_m from the vessel axis (x axis) has the height ΔR_m, relatively thin for large value of M, and the infinitesimal slice of the shell positioned at angle α is insonated by the field of amplitude $G(\alpha, r_m)$ defined as follows:

$$G(\alpha, r_m) = \exp\left(\frac{-(r_m \cdot \cos\alpha)^2}{2\sigma^2}\right) \qquad (5.4)$$

Thus, the power pulse produced by the scatterers moving in the *m-th* shell should be weighted by the factor $F(r_m)$ defined as follows:

$$F(r_m) = 2\int_0^\pi G(\alpha, r_m)\, d\alpha \qquad (5.5)$$

where the 2 multiplying the integral accounts for the symmetry around the y axis. Considering equations (5.2) and (5.3), and introducing $W_f = \frac{W}{2R}$, i.e. the relative beam width with respect to the diameter $2R$, we have:

$$F(r_m) = 2\int_0^\pi \exp\left(-\left(\frac{r_m}{R \cdot W_f}\right)^2 \cos^2(\alpha)\ln(2)\right)d\alpha \qquad (5.6)$$

For the final step, the shell radius r_m should be expressed as a function of the scatterer velocity v_m. In the case of a parabolic profile, this is obtained by inverting the parabola equation: $r_m = R\sqrt{1 - \frac{v_m}{v_P}}$. Using this result in equation (5.6) we obtain the weighting factor to be used in (5.1), which should be evaluated for each shell:

$$P_m = 2\int_0^\pi \exp\left(-\frac{1 - \frac{v_m}{v_P}}{W_f^2}\cos^2(\alpha)\ln(2)\right)d\alpha \qquad (5.7)$$

In case the scatterer is affected by the Gaussian field both during transmission and reception, P_m should be squared, like in equation (5.1).

The model (5.1) has been implemented in Matlab® (The MathWorks Inc., Natick, MA) to generate the spectra reported in Figure 5.2. These refer to a parabolic flow profile and the parameters reported in Table 5.1.
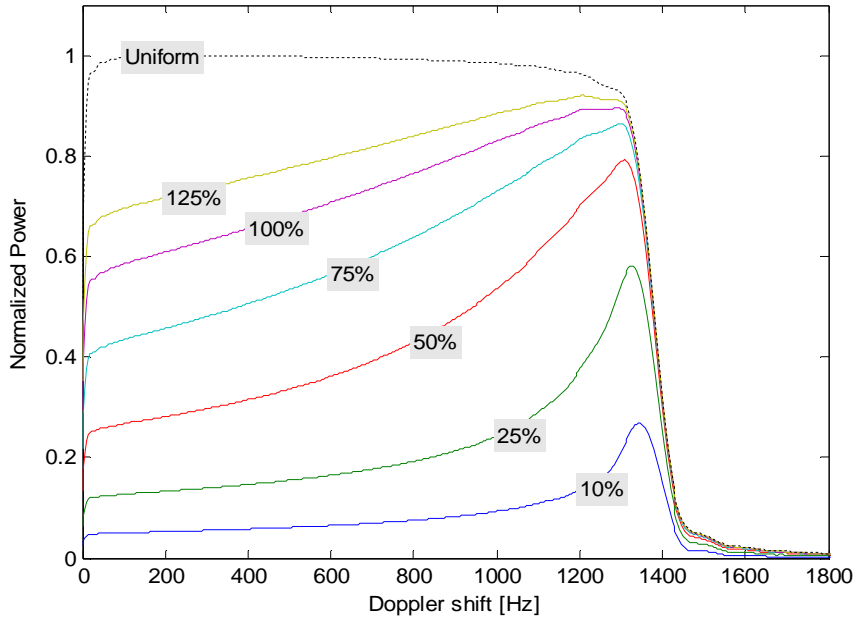
Figure 5.2: Spectra generated by equation (5.1) using the parameters listed in Table 5.1. The relative beam width W_f ranges between 10% (bottom curve) and 125% (second curve from top). Spectra are compared to the spectrum obtained with uniform insonation (top dotted curve).

Parameter	Symbol	Value
Insonation length	A	7.7mm
Transmission frequency	f_t	5MHz
Observation time	T_0	64ms
Peak velocity	v_P	0.8m/s
Doppler angle	θ	75°
PRI length	T_{PRI}	0.5ms

Table 5.1: Parameters used in model study

The top curve, tagged "Uniform", represents the reference spectrum predicted by the original theory with uniform insonation ($P_m = 1 \, \forall \, m$), while the remaining spectra are calculated using (5.7) with W_f in the range 10÷125% (the W_f value is superimposed to the curve it refers to). In particular, the second curve from the top is calculated using W_f=125%, i.e.

a half-amplitude width of the beam wider than the pipe diameter. The pipe is fully insonated, but more power is distributed in the centre of the pipe with respect to the lateral regions. The high velocity components produce a higher contribution, so that the *plateau* shown by the "Uniform" curve is here replaced by a slope slowly degrading towards low frequencies. The situation is similar for W_f=100%, except for a steeper slope; while, for W_f<75%, the curves show a peaked profile. Anyway, all of the spectra show a very similar behaviour in the high-frequency region, provided that W_f<30%.

5.2.2. Non-parabolic flow profile

Since a real blood flow profile can significantly differ from the ideal parabola, it is worth studying the behaviour of non-parabolic flows. We will consider flow profiles expressed by equation (5.8).

$$v_m = v_P \left(1 - \left(\frac{r_m}{R} \right)^{\frac{n+1}{n}} \right) \quad 0 < n \leq 1 \tag{5.8}$$

When n=1, the profile is parabolic, but as n decreases, the profile flattens and approaches a "piston" flow. The effect of a non-parabolic flow can be taken into account by considering the quantity of scatterers in each cylindrical shell. This quantity, given a constant density ρ_m and the insonation length A common to all of the shells, is proportional to the area of the shell section in the z-y plane. Such an area can be approximated as $S_m = 2\pi r_m \Delta R_m$, where ΔR_m is the radial extension of the shell (see Figure 5.1). Inverting equation (5.8), we have:

$$r_m = R \left(1 - \frac{v_m}{v_P} \right)^{\frac{n}{n+1}} \tag{5.9}$$

After differentiating, we obtain:

$$\Delta R_m = \frac{dr_m}{dv_m} \Delta v_m = R \frac{n}{n+1} \left(1 - \frac{v_m}{v_P} \right)^{\frac{-1}{n+1}} \cdot \frac{\Delta v_m}{v_P} \tag{5.10}$$

thus the coefficients S_m can be rewritten as follows:

$$S_m = 2\pi \cdot R^2 \frac{n}{n+1} \left(1 - \frac{v_m}{v_P}\right)^{\frac{n-1}{n+1}} \cdot \frac{\varDelta v_m}{v_P} \qquad (5.11)$$

It should be noted that when the flow is parabolic ($n=1$) S_m is constant, i.e. all the shells hold the same number of scatterers. In this case, the new model (5.1), apart from a multiplying factor, matches the original model.

Spectra predicted by the modified model are shown in Figure 5.3. Normalized with respect to their maximum, the spectra are obtained with the parameters reported in Table 5.1, considering a uniform insonation ($P_m=1$) and n in the range 0.1÷1. As the flow profile flattens, the contribution of the flow components at high velocity increases and the corresponding spectrum assumes a peaked shape.
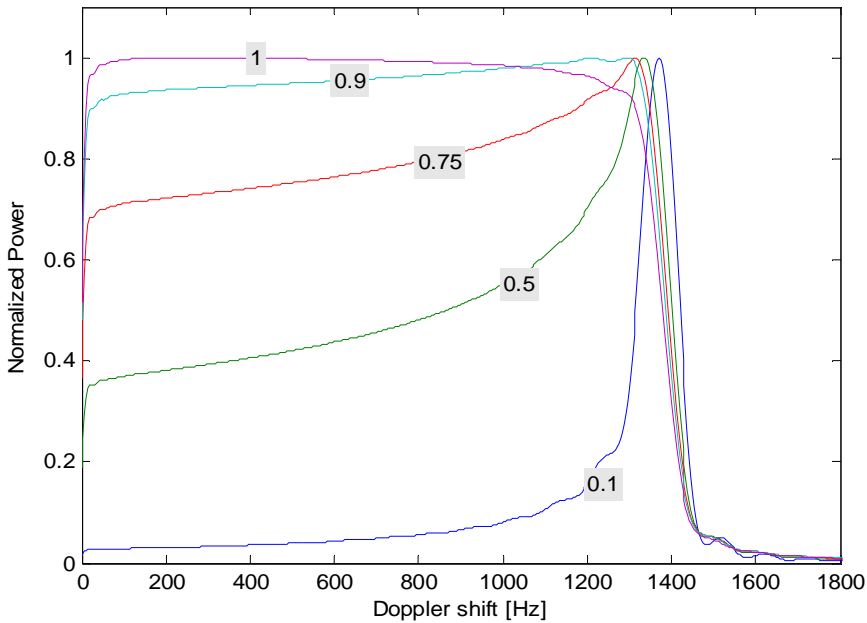

Figure 5.3: Normalized spectra generated with the modified model considering $n = 0.1, 0.5, 0.75, 0.9, 1$.

5.3. A New Threshold Value

As described in Chapter 4, §4.3, for the original, limited to fully-insonated parabolic flows model, the frequency f_{d_P} corresponding to the maximum velocity v_P through the Doppler equation (1.20) is located at half of the slope (Th=0.5). In this paragraph, by using the modified model, we investigate how such a threshold behaves for non-uniform insonation and/or non-parabolic flows.

In a first simulation (Figure 5.4, top panel), several Doppler spectra were generated from the modified model (5.1) using the parameters listed in Table 5.1, considering v_P=0.8m/s, and W_f ranging from 1% to 120%. The threshold was calculated according to its definition, given by the equation (4.14), but, since the spectra do not feature the *plateau* region anymore, the reference is now the spectrum peak. Thus, now ST_F stands for the value of the total spectrum in its peak.

In the second test (Figure 5.4, bottom panel), we analyzed the sensitivity of the threshold to variations in the maximum velocity. In this case, we generated several spectra by varying the velocity v_P in the range 0.1÷1.5m/s, while maintaining the insonation at W_f=30%. The threshold was calculated as described previously.
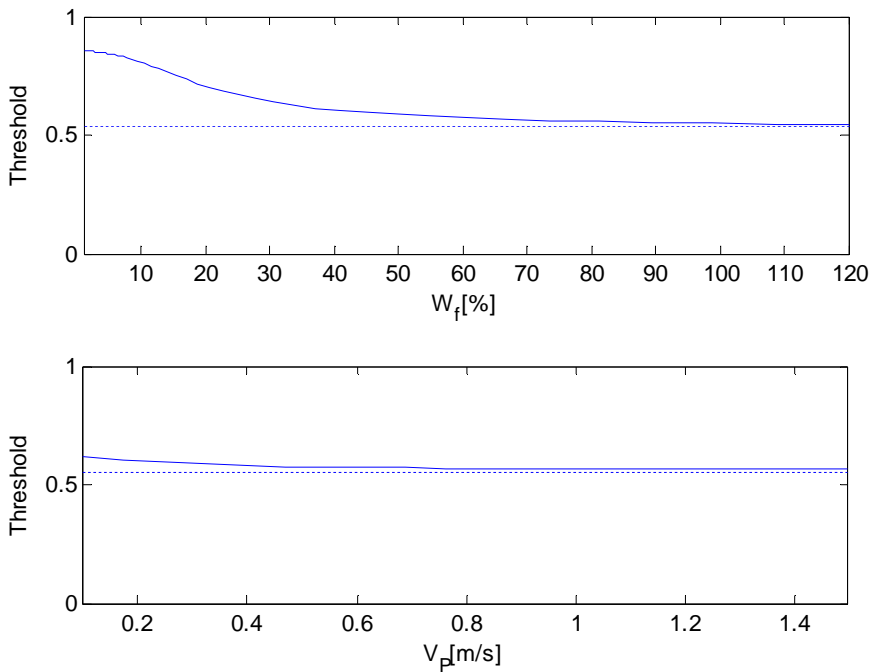
Figure 5.4: Threshold calculated for the parameters listed in Table 5.1 for W_f=1÷120% with v_P=0.8m/s (top) and for W_f=30% with v_P=0.1÷1.5m/s (bottom).

The results suggest that using a threshold of 0.55, instead of 0.5, produce most accurate results over a wide range of beam width and over a wide range of velocities.

The relative error in the maximum velocity measurement obtained using the threshold Th=0.55 was evaluated in the experiment shown in Figure 5.5. Here the insonation ranged from 10% to 100%, and the profile shape changed with values of n from 0.01 to 1. In this case, the peak value ST_F was first detected in each spectrum. Then, the frequency corresponding to $0.55 \cdot ST_F$ was located on the spectrum slope and converted by the Doppler equation (1.21) to the measured peak velocity, v_{PM}. The relative error in the velocity was finally calculated as $(v_{PM} - v_P)/v_P$.
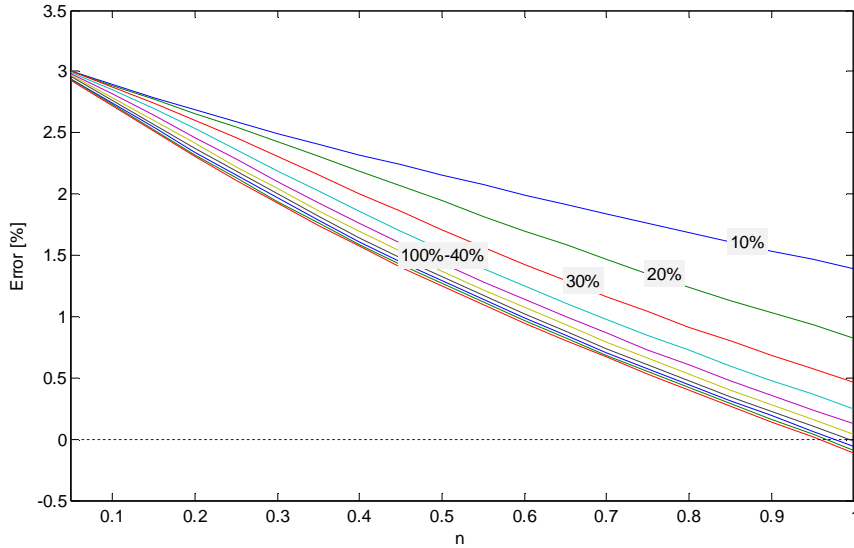
Figure 5.5: Relative errors on the measured peak velocity (v_{PM}) with respect to the reference peak velocity (v_P).

The error presents a roughly linear trend for n between 0.1 and 1. The error is higher for narrower beams (W_f=10%, top blue curve), reduces for W_f=20% and it is rather equivalent, in particular for high values of n, when W_f≥30%. In this last case, the error goes to 0 when n=1, confirming the results reported in Figure 5.4. In any case, provided that the flow is not highly distorted (n>0.5) and W_f≥30%, the theoretical error is lower than 1.5%. This confirms that the threshold Th=0.55 is suitable for all of the considered cases.

5.4. *Experimental Validation*

The modified method has been validated by checking the predicted spectra, obtained with the mathematical simulations, both with Field II® [8], [9] simulations and with phantom experiments. The used parameters and experimental set-up are described below.

5.4.1. Filed II® simulations

Ultrasound simulations have been conducted with the following set-up to validate the model and to perform maximum velocity measurements. A 192-element linear array probe characterized by the parameters listed in Table 5.2 was used, with an active aperture of 54 elements that transmitted a non-focused wave steered by $\delta=15°$ (see Figure 5.6).
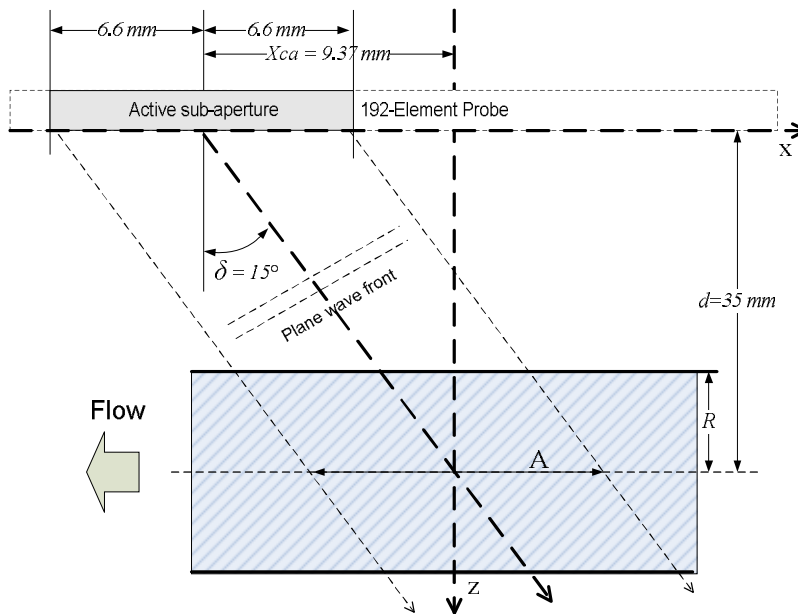
Figure 5.6: Geometry of the simulated set-up. The y-axis is perpendicular to the picture plane.

The active aperture was centred at Xca=9.37mm from the probe centre; thus, the central axis of the wave crossed the probe z-axis at 35mm depth. Bursts composed of 60 cycles at 5MHz, which corresponds to a sample volume with 9mm axial extension, were transmitted every PRI=0.5ms. This sample volume includes vessels with diameters up to 8mm, while the PRI is selected according to the maximum expected frequency. A *Tukey* window was applied to the aperture elements for a better field uniformity along the x direction. A wall-less tube of radius R was located at 35mm depth, with its axis parallel to the probe surface.

Parameter	Symbol	Value
Transducer		
Center frequency	f_0	5Hz
Speed of sound	c	1500m/s
Element pitch		0.245m
Total elements		192
Transmission/Reception		
Aperture elements		54
Sampling frequency	f_s	50MHz
Transmission cycles		60
Aperture center position	Xca	9.37mm
Apodization window		Tukey
Pulse Repetition Frequency	$1/PRI$	2kHz
Steering angle	δ	15°
Phantom		
Vessel radius	R	1, 1.5, 2, 4
Profile shape	n	0.5, 1.0
Flow peak velocity	v_P	0.8m/s
Distance to vessel centre	d	35mm
Insonated length	A	7.7mm

Table 5.2: Parameters used in Field II® simulations.

5.4.2. Phantom experiments

The predicted spectra have been compared to the spectra obtained in a flow phantom experiment by using the configuration reported in Figure 5.9.

The blood-mimicking fluid, prepared as described in Chapter 2, §2.3.1, was moved by a gear pump (Watson-Marlow Fluid Technology Group, Wilmington, MA, USA) and flowed into an open circuit from a main reservoir, where the fluid was continuously stirred, to the measuring cell and then back to the reservoir. The flow oscillations produced by the gear pump were filtered by an expansion tank in the hydraulic circuit. A relief valve is used to remove the air present in the circuit during the initial

phase. The flow in the circuit was measured by a flowmeter (model E52600, Asa s.r.l., Sesto S. Giovanni, Italy) and the reference peak velocity was obtained, according to equation (1.45), assuming a parabolic flow profile. The accuracy of the reference velocity was estimated in ±3.5cm/s.
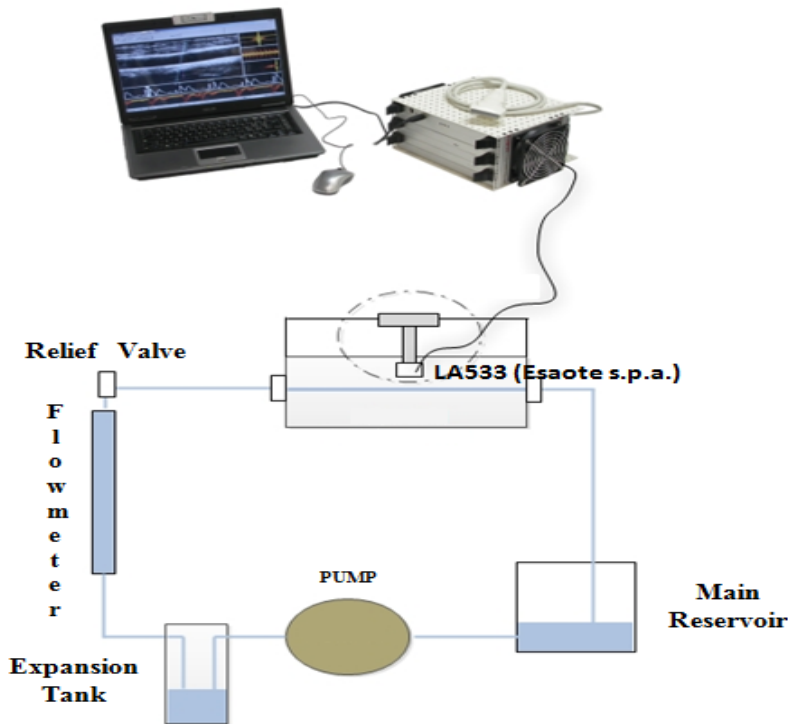
Figure 5.9: Phantom experimental set-up.

The measuring cell, whose geometry is sketched in Figure 5.6, consisted of a 4mm diameter straight tube immersed in a water tank. The linear array probe LA533 (Esaote s.p.a., Firenze, Italy) was held over the tube and connected to ULA-OP. The independent arbitrary wave generators included in the system were programmed to excite a 54-element aperture of the probe with the same pulses as used for the simulations (see Table 5.2). The ULA-OP receiver was programmed for *Tukey* window apodization and non-focused beamforming. The successive data elaboration was the same as used in the simulations, apart from a 150Hz wall filter applied to the phantom data.

5.5. **Results**

5.5.1. Field II® simulations

The measured backscattered echoes were collected by the same aperture used for transmission. The apodization and delay used in transmission were applied, unchanged, to the same element during the signal reception. The x-z and y-z views of the resulting 2-way pressure field, i.e. the field that includes the combined effects of transmission and reception, are shown in greyscale on the top of Figure 5.7. The horizontal dashed line, which is placed at z=35mm, highlights the depth where the tube axis is located. The pressure field at this depth is given in the middle panel of Figure 5.7 for the x and y directions. Along the tube axis (x direction), the field is roughly constant (variation lower than −6dB) for its 7.7mm extension, while in the y direction, it follows a typical bell shape with a −6dB extension of 2.25mm. Along the z direction, i.e. the tube diameter, the field can be approximated as uniform (see Figure 5.7, bottom).
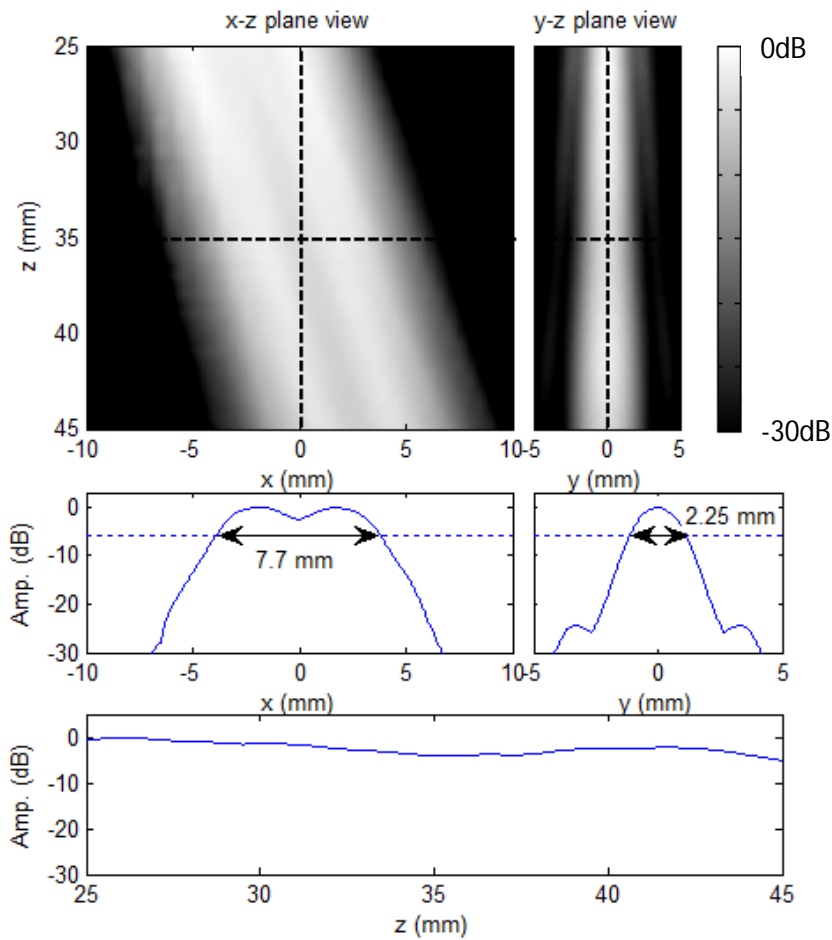
Figure 5.7: Simulated 2-way acoustic field. On top the x-z and y-z views are reported in greyscale with 30dB dynamics. The field profile at 35mm depth (corresponding to the horizontal dashed lines on top) are reported in the centre for x and y axes, respectively. The half-amplitude extension is highlighted by the −6dB dashed lines. The field along the probe axis (x=0, y=0, corresponding to vertical dashed lines on top) is reported in the bottom panel.

Simulations were performed by imposing steady flows (0.8m/s velocity peak) with profile shapes corresponding to n=0.5 and n=1. Tubes with R of 4mm, 2mm, 1.5mm, and 1mm were investigated. This range is representative of vessels of high interest, such as the carotid, brachial, femoral, and uterine arteries. For a beam width of 2.25mm (see Figure

5.7), these radii correspond to W_f=113%, 75%, 56%, and 28%, respectively. By combining two values of n and four different tube radii, simulations with eight different flows/relative beam width configurations were performed. For each set-up, Field II® data were saved for approximately 1200 transmissions. The samples selected from 50% overlapped sliding windows were processed by applying 128-point FFTs, suitable of producing the spectral resolution required in Doppler applications. The corresponding observation time is T_0=128·0.5ms =64ms, where 0.5ms is the Pulse Repetition Interval.
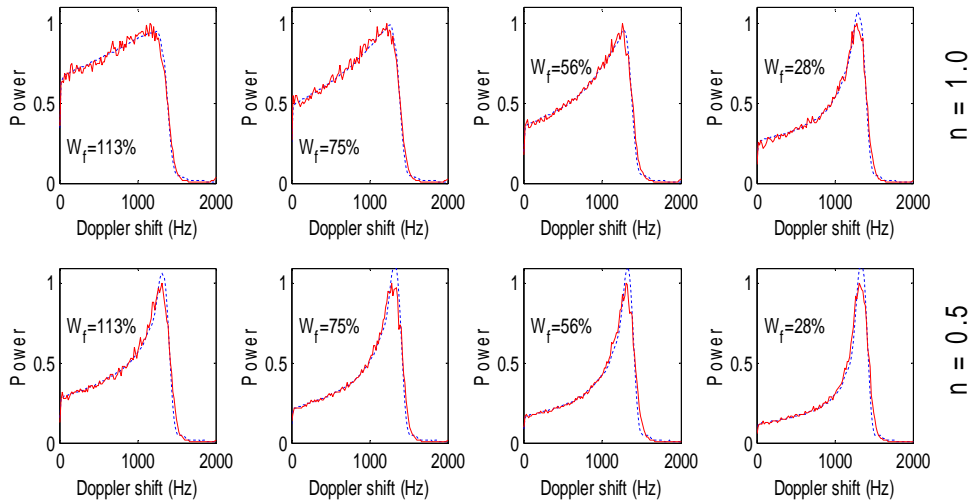
Figure 5.8: Comparison between spectra generated by the model (blue dotted curve) and simulated by Field II® (red continuous curve) with n=1 and n=0.5 (left and right column, respectively) and W_f=28%, 56%, 75%, 110%.

Figure 5.8 compares the spectra predicted by the proposed model to the spectra simulated by Field II® in the set-up described before. The spectra were obtained by using two profile shapes (n=1 for the top row, and n=0.5 for the bottom row) and four insonation configurations (columns).

The accuracy achievable in maximum velocity measurements based on the spectral threshold of 0.55 is evaluated. Table 5.3 lists the errors obtained for all of the investigated cases. A 1.2cm/s mean overestimation with 1.2cm/s standard deviation (SD) was obtained.

	W_f=28%	W_f=56%	W_f=75%	W_f=113%
n=1.0	-0.72cm/s	-0.06cm/s	+0.23cm/s	+1.11cm/s
n=0.5	+1.68cm/s	+2.13cm/s	+2.26cm/s	+2.93cm/s

Table 5.3: Errors for maximum velocity detection in simulated

5.5.2. Phantom experiments

Experiments were performed with physiologically useful maximum velocities ranging from 34cm/s to 82cm/s.
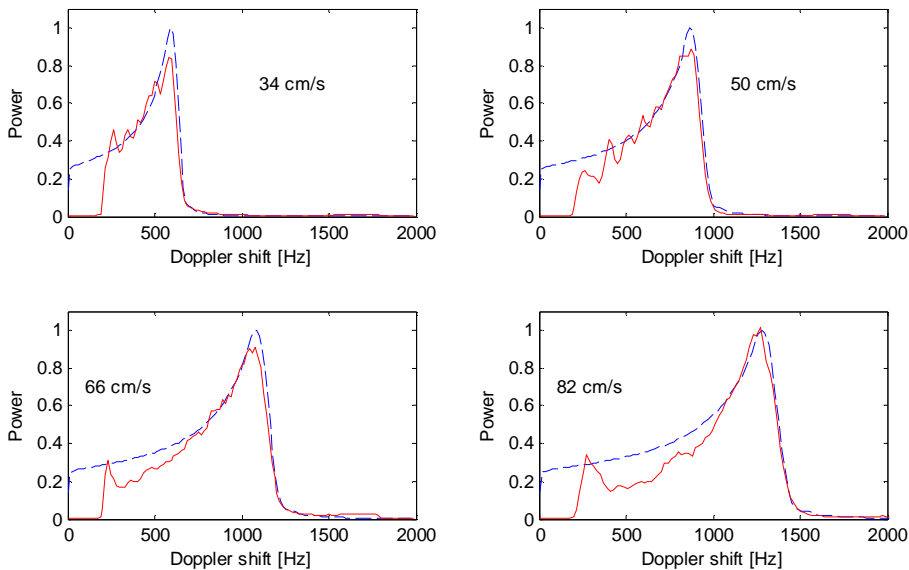
Figure 5.10: Comparison between four spectra generated by the model (blue-dashed curve) and those measured in the experiments (red continuous curve).

Figure 5.10 shows four examples of the experimental spectra measured in the set-up described above (red continuous curves) using velocities of 34cm/s, 50cm/s, 66cm/s, and 82cm/s, as indicated in the figure. The spectra predicted by the model with n=1 and W_f=35% are superimposed (blue-dashed curve).

The accuracy obtainable in maximum velocity measurements has been evaluated. In Figure 5.11 each circle represents the measurement error

with respect to the corresponding reference velocity estimated through the flowmeter. The vertical bars centred on each circle represent the reference velocity uncertainty due to the flowmeter tolerance. An average bias of +1.2cm/s with a SD of 2.5cm/s has been measured. The dashed and dotted horizontal lines in the picture represent the bias and the ±2·SD range, respectively.
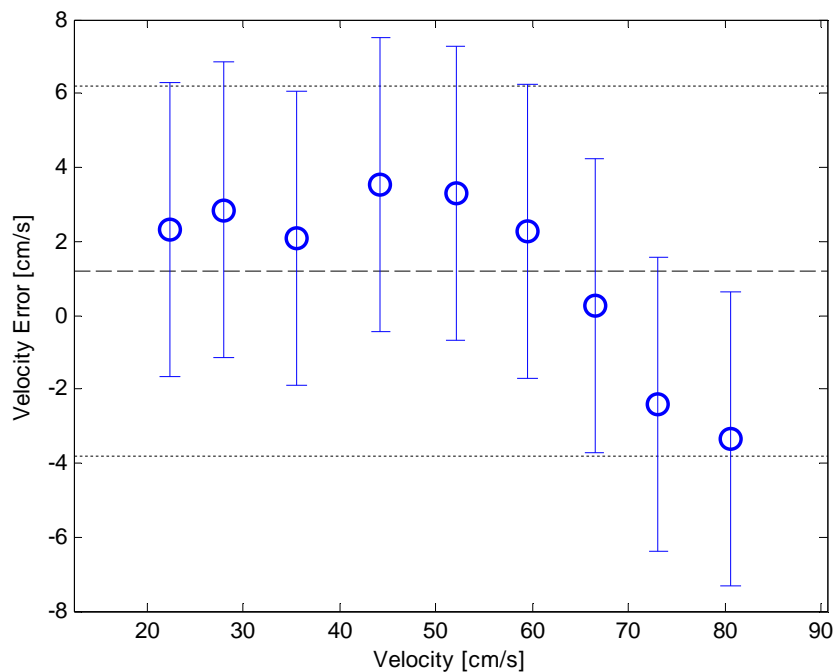
Figure 5.11: Comparison between measured and reference maximum velocities for flow in the range 80÷310ml/min. the dashed horizontal line corresponds to the mean error, while the dotted lines report the ±2·SD range.

Chapter 6. VECTOR BLOOD PEAK VELOCITY DETECTION

The modified model presented in Chapter 5 reproduces a more reaisticl clinical condition when assessing the blood peak velocity, but does not solve the Doppler angle ambiguity. This chapter presents a vector implementation of the modified model that overcomes this limitation.

6.1. Introduction

As described in Chapter 1, §1.6.1, for an accurate measurement of the velocity, the Doppler angle should be known as well. In fact, inaccuracies in determining the Doppler angle represent a well-known source of error in velocity measurement [36], [41]. The effect of an inaccurate Doppler angle determination, being the velocity related to $1/\cos\theta$, is higher as the angle approaches 90°. This condition typically happens, for example, in the carotid artery, where the probe is almost parallel to the vessel and the Doppler angle is determined by the limited steering capability of the probe.

For this reason the method described so far, that gives a robust way for the peak velocity in the flow, has been implemented in a vector Doppler configuration [42].

The proposed vector implementation of the method has been validated through Field II® [8], [9] simulations and phantom experiments using different flow velocities, vessel diameters, and probe-to-flow inclinations. Moreover, a preliminary test on healthy volunteers has been performed.

Finally, thanks to the collaboration with the University of Hong Kong, the method has been tested on an anthropomorphic phantom. The phantom reproduces a human carotid artery with a 50% stenosis in the internal branch. The vector method developed so far, which can be referred to as *method under test* (MUT), has been applied to this phantom comparing the results to those obtained from two techniques already validated and implemented in the ULA-OP scanner. The two methods are the *Multigate-Spectral-Doppler* (MSD) and the *MultiGate-Vecto-Doppler* (MGVD). In MSD the Doppler shift is measured on 512 consecutive points of a standard PW Doppler line placed across the vessel. In each point the velocity is calculated through equation (1.21) by using the Doppler angle evaluated in the B-Mode image. In MGVD two lateral apertures of a linear array probe transmit plane waves and focalize in reception along a line placed across the vessel. In each of the 512 points of this line the right and left Doppler shifts are measured and used to obtain the velocity vector. A more detailed explanation of MSD and MGVD can be found in [5] and [43] respectively.

6.2. *Method*

In Figure 6.1 it is sketched the geometry implemented for the extension of the method to the vector configuration. Every PRI, a central sub-aperture of a linear probe transmits an unfocused beam perpendicular to its surface. Two lateral sub-apertures, symmetrically positioned at distance X_{ca} from the probe z axis, receive the backscattered echoes along the steering directions $\pm \delta$, without receiving focus. The length of the transmitted bursts, the position X_{ca} and the steering angles $\pm \delta$ are set to produce a large rectangular sample volume (represented in light blue in Figure 6.1), which is located at depth d and extends for A and l in the x and z directions, respectively.
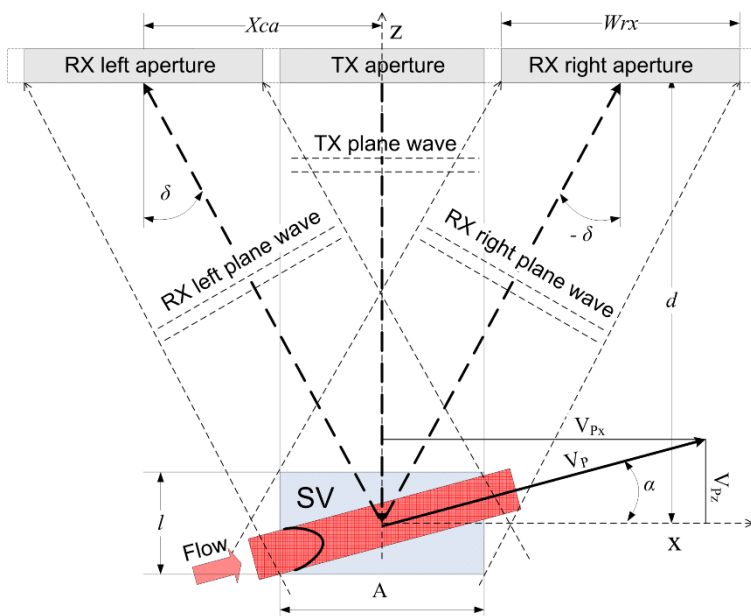
Figure 6.1: A flow moving at angle α with velocity v_P crosses a sample volume (SV) placed at depth d. The SV is insonated by a plane wave transmitted along the z-axis of a linear probe. The backscattered echoes are received by 2 symmetric sub-apertures along the steering angles $\pm \delta$.

The pressure field can be considered uniform in the x and z directions, while it features a Gaussian profile along the y direction, i.e. perpendicular to the plane represented in Figure 6.1. A vessel, positioned

at an angle α with respect to the probe surface, crosses the sample volume so that it is fully insonated for the length A. The echoes are acquired separately from the two lateral sub-apertures for the observation time T_0 and processed through the spectral analysis reported in [1]. The maximum Doppler frequencies, f_{dPl} and f_{dPr}, are located on the left and right spectra generated by the two receiving sub-aperture, respectively, by applying the threshold Th=0.55. According to the theory reported in Chapter 1, §1.6.1, such frequencies are related to the velocity v_P by the following equations:

$$\begin{cases} f_{dPl} = \dfrac{f_t}{c} v_P[\sin(\alpha) + \sin(\alpha - \delta)] \\[2mm] f_{dPr} = \dfrac{f_t}{c} v_P[\sin(\alpha) + \sin(\alpha + \delta)] \end{cases} \qquad (6.1)$$

Following the same steps as shown in §1.6.1, and so by subtracting and adding the expressions in (6.1) and then substituting the velocity components along the x and z axes, according to the equation (1.41), we obtain:

$$\begin{cases} v_{P_x} = \dfrac{c}{2f_t}\left[\dfrac{f_{dPr} - f_{dPl}}{\sin(\delta)}\right] \\[3mm] v_{P_z} = \dfrac{c}{2f_t}\left[\dfrac{f_{dPr} + f_{dPl}}{1 + \cos(\delta)}\right] \end{cases} \qquad (6.2)$$

Thus, the angle corrected peak velocity is given by:

$$|v_P| = \sqrt{v_{P_x}{}^2 + v_{P_z}{}^2} \qquad (6.3)$$

6.3. Experimental set-ups

6.3.1. Field II® set-up

The simulated set-up reproduced the geometry of Figure 6.1 and used the parameters listed in Table 6.1. We simulated a linear array with 192 elements. A central sub-aperture of 45 elements transmitted an unfocused burst composed of 80 cycles at 7MHz. This corresponds to a sample volume axial depth of l=8.8mm, suitable to include large vessels such as the carotid artery. A *Tukey* window was applied to the sub-aperture elements for a better field uniformity along the x direction. In reception, 2 sub-apertures, composed of 64 elements each, were centred at X_{ca}=±9.9mm, and partially overlapped to the transmitting sub-aperture.

Parameter	Symbol	Value
General		
Speed of sound	c	1540m/s
Sampling Frequency	f_c	50MHz
Element pitch		0.245mm
Probe elements		192
Transmission		
Sub-aperture elements		45
Transmission cycles		80
Apodization window		Tukey
Pulse Repetition	f_{PRF}	2kHz
Reception		
Sub-apertures elements		64
Sub-apertures center	X_{ca}	±9.97mm
Sub-apertures extension	W_{rx}	15.68mm
Steering angles	δ	±14°
Apodization window		Tukey

Table 6.1: Parameters used in Field II® simulations.

The two sub-apertures received the echoes with $\delta=\pm14°$ steering angles. *Tukey* apodization and no focusing were used in reception as well. We used Field II® to investigate the 2-way pressure field (i.e. the field that includes the combined effects of transmission and reception). Although the transmitting sub-aperture had an extension of 45×0.245mm=11mm, we verified that the overlap region at depth d=40mm had a −6dB extension A=8mm along the x direction. According to simulations, the 2-way pressure was reasonably uniform in the z and x directions, and it features a Gaussian shape along the y axis. In this direction a −6dB extension of 2.8mm was observed. This is sufficient to cover most of the important large vessels with a ratio between the −6dB beam extension and the vessel diameter higher than 30%, as required by the model [44]

Wall-less tubes with 4mm, 6mm, and 8mm diameter were located at 40mm depth with their axes angled of 0°, 10°, 20°, and 30° with respect to the probe surface. Parabolic flows with steady peak velocities v_P=0.4 m/s, 0.8 m/s, and 1.2m/s were imposed. Scatterers with a density of 30000/cm^3 which scattering strength featured a normal distribution with a mean of 1 and standard deviation of 0.4 were used. The PRI duration was selected according to the expected Doppler shift. A first set of 32 simulations was performed with different combinations of the aforementioned parameters.

A second flow set-up was built to investigate how the measurement of the peak velocity of the main flow is affected by the presence of flows with different velocities and directions in the sample volume (Figure 6.2).
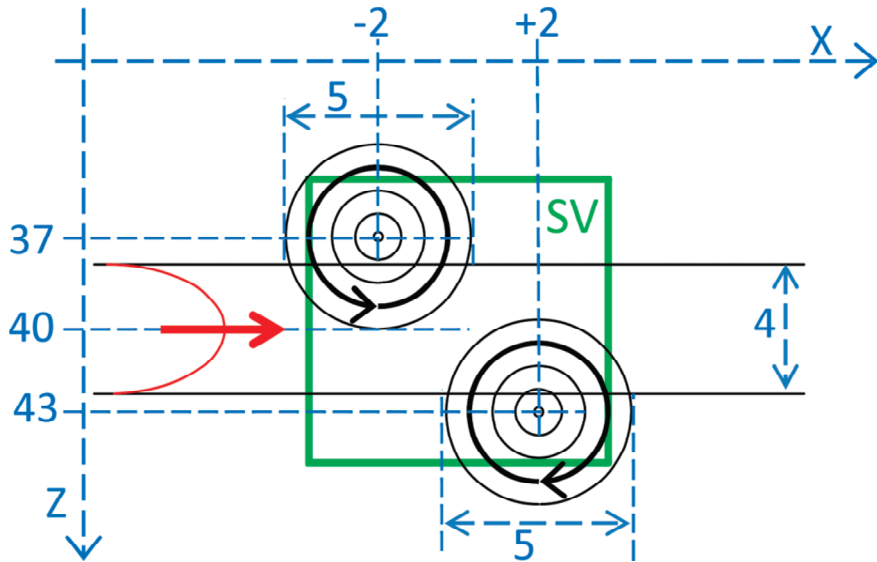
Figure 6.2: A 4mm parabolic flow runs among two vortexes of 5mm diameter placed near the upper-left and bottom-right corners of the sample volume. The flow has a centreline velocity of v_P=1.4m/s, and the vortexes have an angular velocity of 157rad/s, anticlockwise and clockwise, respectively.

In this set-up, a main cylindrical flow of 4mm diameter runs parallel to the probe at 40mm depth with v_P=1.4m/s. At the right side of the sample volume, centred at 43mm depth, a cluster of scatterers, moving along circular trajectories, was placed in the plane of the probe. The vortex has a diameter of 5mm and an angular velocity of 157rad/s, corresponding to velocities between 0cm/s to 40cm/s, spread in all directions. On the left side of the sample volume, centred at 37mm depth, a similar vortex was simulated, but with an opposite angular velocity of −157rad/s. Measurements with and without the disturbing vortexes were compared.

6.3.2. Phantom set-up

Velocity measurements were performed in a flow-phantom similar to that described in Chapter 5, §5.4.2., in both steady and pulsatile conditions. The programmable pump (Watson-Marlow Pumps Group, Falmouth, UK) moved a blood-mimicking fluid in a hydraulic circuit from a reservoir at air pressure, where the fluid was continuously stirred, to the measuring cell and then back to the reservoir. As described in Chapter 2,

§2.3.1, the blood mimicking fluid was prepared by dissolving 3g of Orgasol (Arkema Inc., Philadelphia, PA, USA) particles in 2ℓ of demineralized water [17]. In steady conditions, the flow in the circuit was measured by the flowmeter (model E52600, Asa s.r.l., Sesto S. Giovanni, Italy) present in the circuit. The reference peak velocity was obtained, assuming a parabolic flow profile, as $v_{ref} = 2Q/S$, where Q is the measured flow and S is the tube cross-section. The measuring cell consisted of a water tank where a straight plastic tube with a 1mm-thick wall was immersed. A micromechanical position system held the linear array probe LA533 (Esaote s.p.a., Firenze, Italy), connected to the ULA-OP [5], [6], over the tube, and allowed the probe to be tilted at known angles.

The independent arbitrary wave generators included in the system [45] were programmed to excite a 45-element sub-aperture of the probe with the same pulses as used for the simulations (see Table 6.1). In reception the two 64-element sub-apertures were positioned and steered as reported in Table 6.1. In this case, due to hardware constraints, the PRI sequence was subdivided so that data were acquired alternatively from the right and left sub-aperture, respectively. *Tukey* window apodization and unfocused beamforming were used both in transmission and reception. The successive data elaboration was the same as used in the simulations, except for a 50Hz wall filter added here to cut the clutter produced by the pipe wall.

6.3.3. Healthy volunteers protocol

We tested the proposed method on three healthy volunteers aged 25 to 44 years old. The echograph was set in duplex mode, and the Doppler sequence was the same as described for the phantom experiments. Each volunteer stayed in a comfortable position for 5 minutes before the acquisition phase. An expert sonographer, guided by the B-mode display, positioned the probe so that a longitudinal section of the common carotid artery, located about 1cm from the bifurcation, was completely included in the Doppler sample volume. Data from the left and right sub-apertures were saved for at least 3 heart cycles. For each volunteer, 6 acquisitions were saved, alternating left and right carotids.

6.3.4. Anthropomorphic phantom set-up

The anthropomorphic phantom used in the experiments is shown in the B-Mode scan reported in Figure 6.3. It consists of a wall-less carotid phantom with 50% eccentric stenosis narrowing at the entrance of the internal artery (ICA). The phantom is manufactured at Hong Kong University by exploiting a lost-core casting approach, similar to that described in [46]. Its vessel lumen is of co-planar bifurcation geometry. In particular the diameters for common (CCA), internal (ICA), and external (ECA) carotid artery branches are 6mm, 3mm, and 4mm, respectively. The phantom's tissue mimic material is a polyvinyl alcohol cryogel with 120kPa elastic modulus, 1518m/s sound speed and 0.24dB/(cm·MHz) attenuation.
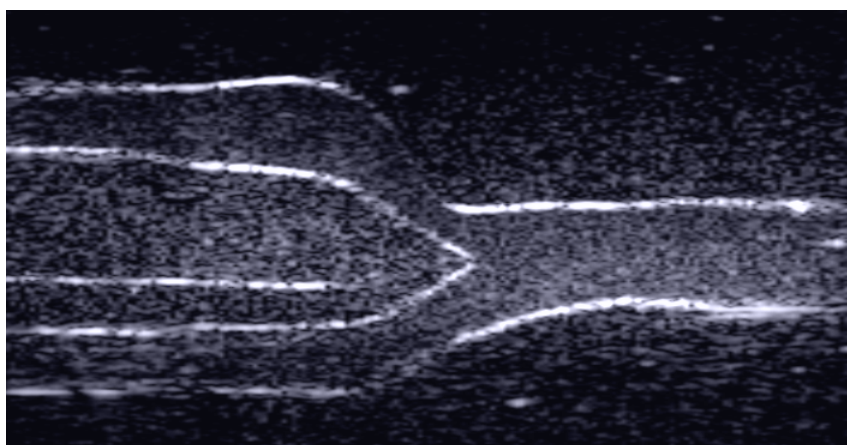
Figure 6.3: B-Mode scan of the carotid phantom used in the experiments

The anthropomorphic phantom was substituted to the pipes inside the hydraulic circuit used in the previous experiments, keeping unchanged the other parts. The linear array probe LA533 (Esaote spa, Florence, Italy) was positioned over the phantom so that the ultrasound beam investigated the bifurcation plane. The probe was connected to the ULA-OP research scanner, which was programmed for generating the transmission and reception sequences for the MUT, MSD and MGVD. Several seconds of received data were acquired and saved in files for post-processing.

Experiments were performed in the CCA, about 1cm before the bifurcation, and in the ICA, about 2÷3mm after the stenosis of the anthropomorphic phantom. In CCA we tested 4 different pump settings with pulsatile trend. Four acquisitions, lasting at least 2 cardiac cycles each, were saved for each of the 3 methods (MUT, MSD, MGVD) and for each pump setting, resulting in a total of 48 experiments. A similar protocol was used for ICA experiments. In this case we tested 3 pump settings, acquiring 4 files for each method, for a total of 36 experiments.

6.4. Results

6.4.1. Field II® simulations

For each experiment, Field II® data were saved for approximately 1200 PRIs. The samples were processed in 50% overlapped sliding windows of N samples, where N was chosen so that the observation time T_0 covered about 50ms. The samples were processed by applying FFTs, with frequency resolution of $1/T_0 \approx 20$Hz. The spectra were averaged and further processed for velocity detection according to the vector implementation of the method. The detected velocity, v_{P_m}, was compared with the reference velocity v_{ref} set in the simulation to obtain the relative error:

$$Err\ [\%] = \frac{v_{P_m} - v_{ref}}{v_r} \cdot 100 \qquad (6.4)$$

Figure 6.4 reports the error distributions calculated from equation (6.4) for peak velocity measurements obtained from the Field II® simulations on steady flows.

The 36 experiments are grouped for reference velocity, tube-to-probe angle, and tube diameter. The error distribution is separately analyzed for each population and reported in the 3 panels. In particular, the extension of the boxes accounts for the 25th and 75th percentiles; the internal horizontal segments report the median value; the outer whiskers are the maximum and minimum errors. No outliers were found. The horizontal dashed line represents the average error calculated on the whole population, which

corresponds to a mean underestimation of −0.13%. The standard deviation of the error was 0.8%.
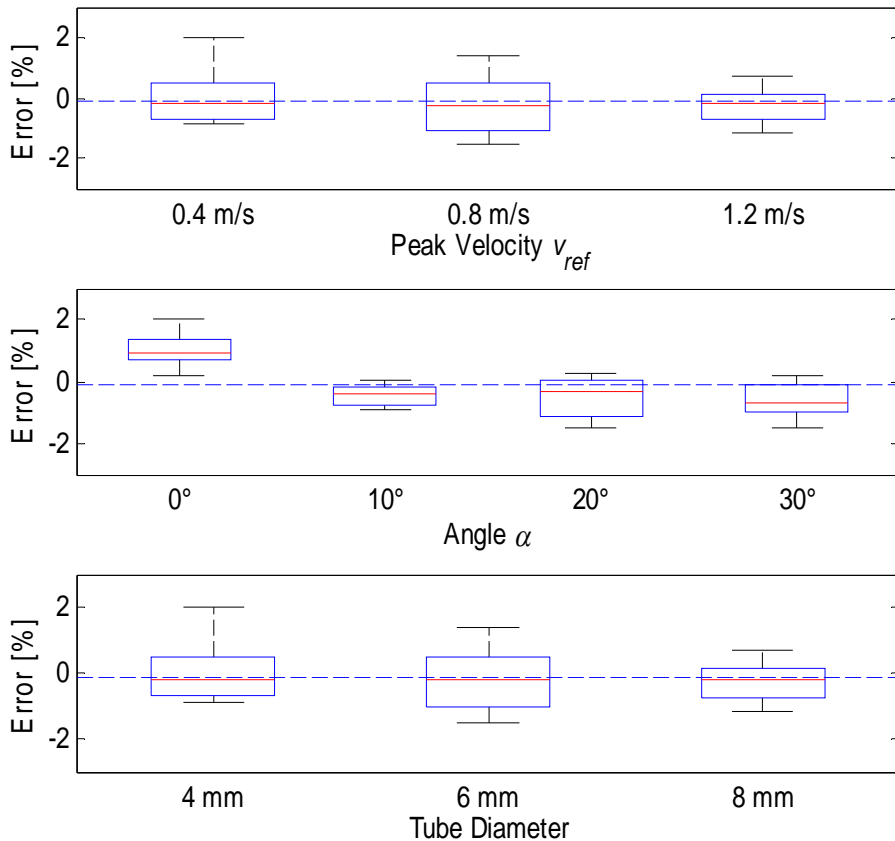
Figure 6.4: The velocity error observed in Field II® simulations is reported for different velocities, v_{ref}; probe-to-tube angles, α; and tube diameters (top to bottom). The box edges account for 25th and 75th percentile, the inner segments and the whiskers are the median and the outermost values. The horizontal dashed line represents the average error.

The spectra measured in the second flow set-up (see Figure 6.2) are reported in Figure 6.5. The top row shows the left and right spectra obtained from the flow with v_P=1.40m/s. In this example, the actual measurement is v_{P_m}=1.42m/s, which corresponds to a 1.5% overestimation. The bottom row of the figure shows how the spectra

change when the vortexes are added. In this condition, the measurement is v_{P_m}=1.43m/s (i.e. a 2.1% error).
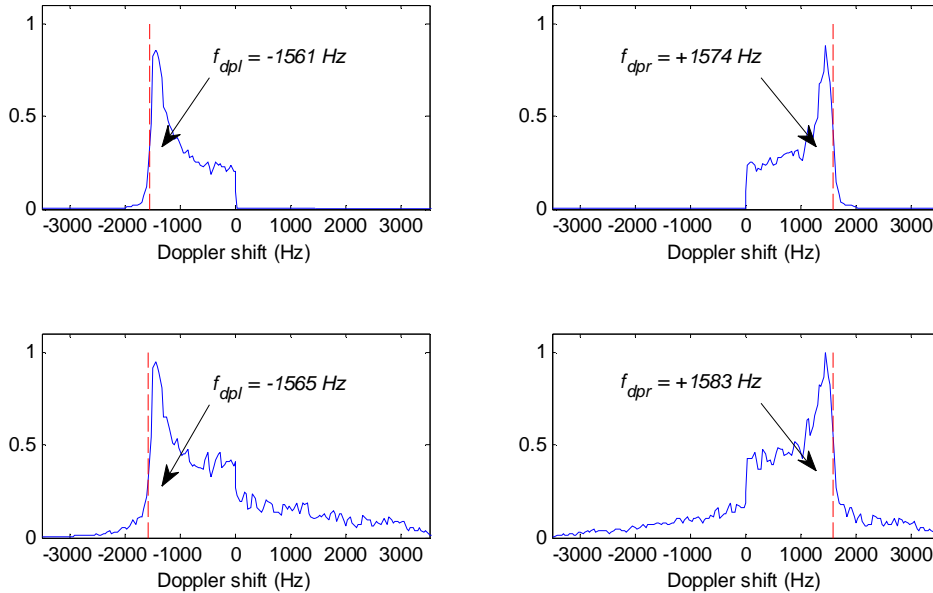
Figure 6.5: Left (left column) and right (right column) spectra generated by a v_P=1.4m/s jet flow without and with disturbing vortexes (top and bottom rows, respectively). The detected $f_{d_p l}$ and $f_{d_p r}$ frequencies are marked by vertical dashed lines.

The error obtained in Field II® simulations shows a regular trend for different velocities, probe orientations, and pipe diameters. A very low bias has been measured (-0.13%) and the error was always lower than $\pm 2\%$. The vortexes added in the second set-up generated a visible noise in both the positive and the negative spectra. However, the peak and downslope regions produced by the main flow were basically unaffected, and the accuracy of the peak velocity measurement deteriorates by less than 1%.

6.4.2. Phantom experiments

Experiments in steady flow conditions were performed with maximum velocities ranging from 10cm/s to 110cm/s, angles between tube and probe surface of 0°, 7°, 14°, and 21°, and tube diameters of 4mm and 6mm, for a total of 256 measurements. Experiments in pulsatile conditions were

performed in a 6mm-diameter tube, angles of 0°, 7°, 14°, and 21°, and 3 different waveforms with peak velocities in the range 45cm/s to 70cm/s. For each flow condition and angle, 4 acquisitions, each including about 3 systolic peaks, were saved, for a total of 48 acquisitions. Each measurement was obtained by averaging the velocities detected for the 3 peaks present in each file.

Figure 6.6 reports the measurements together with the regression line (dashed-red) and the identity line (dotted-black).
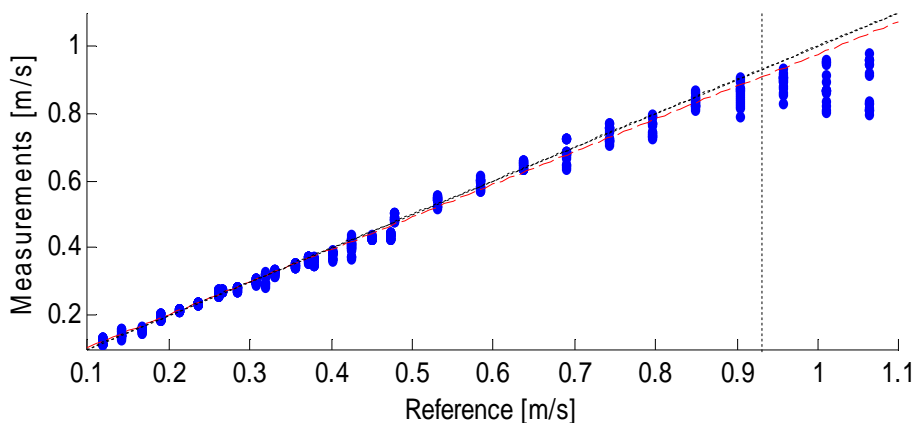
Figure 6.6: Measurements (•) and regression line (red-dashed) are compared to identity (black-dotted). Measurements higher than 0.95 m/s (dotted vertical line) are not included in regression analysis.

The regression line, $y = ax + b$, was calculated by excluding the velocities over 0.95m/s (see vertical dotted line). A gain and offset of about a=0.96 and b=0.085cm/s was found (see Table 6.2). The coefficient of determination, R^2, was very close to 1. The root mean square error (Rmse), calculated between the measurements and the regression line, is quite low.

a	0.967
b	0.08469cm/s
R^2	0.9921
Rmse	0.184cm/s

Table 6.2: Linear regression parameters

The statistics of the difference between measurements and flowmeter readings were tested for normal distribution by the *Student's t-test* [47], which produced a positive result with $p=0.93$, a mean $\mu=-0.8\%$, and a standard deviation $\sigma=2.6\%$.

In Figure 6.7 the measurements are compared with flowmeter readings for the 4mm and 6mm pipes, top and bottom panels respectively. According to the *Bland-Altman* [18] representation in abscissa and ordinate the mean velocity, i.e. $(v_{P_m} + v_{ref})/2$, and the difference, i.e. $(v_{P_m} - v_{ref})$, are reported. The horizontal dotted lines show the mean bias and the limits of agreement, whereas the continuous red lines represent the accuracy of the flowmeter that, for 4mm and 6mm diameter pipes, corresponds to ±3.2cm/s and ±1.4cm/s, respectively.
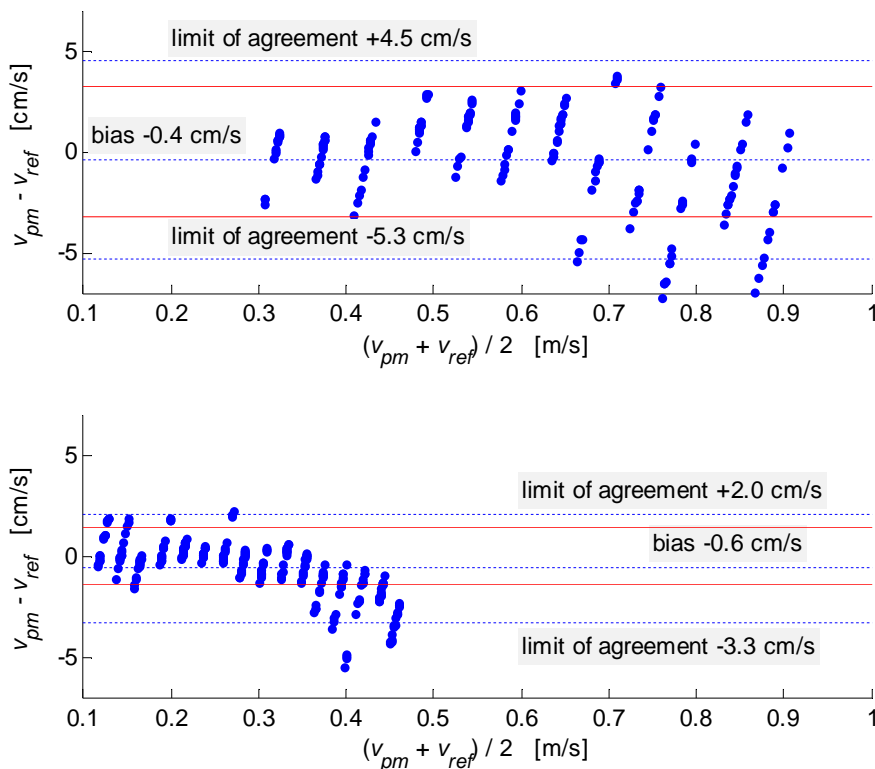

Figure 6.7: Measurements (•) are compared to the flowmeter readings with Bland-Altman method for 4mm and 6 mm pipe (top and bottom panel, respectively). Dotted horizontal lines show the bias, limits of agreement, and flowmeter accuracy.

As far as the measurements with pulsatile flow conditions, the measurements were divided in 3 groups (G_1, G_2, and G_3), one for each waveform generated by the pump. Each group included 16 measurements, obtained from the 4 acquisitions gathered at each of 4 different angles. Figure 4.31 shows, for example, the spectra measured with the waveform G_3 at $\alpha=21°$. In this condition, both the left and right spectra extend in the positive side of the frequency range. The frequencies detected in the downslope region are $f_{d_P l}=1534$Hz and $f_{d_P r}=3047$Hz, corresponding to $v_{P_m}=70$cm/s and $\alpha=20.4°$. The SNR was calculated as the ratio between the power peak and the noise level. For example, in the spectrum of Figure 6.8 top, the peak is normalized at 1, whereas the noise level, averaged in the region $2000<f<3000$, corresponds to a SNR of 28dB. The mean peak velocity and the coefficient of variation (CV), i.e. the ratio between the standard deviation and the mean, are reported in Table 6.3 separately for the 3 groups.
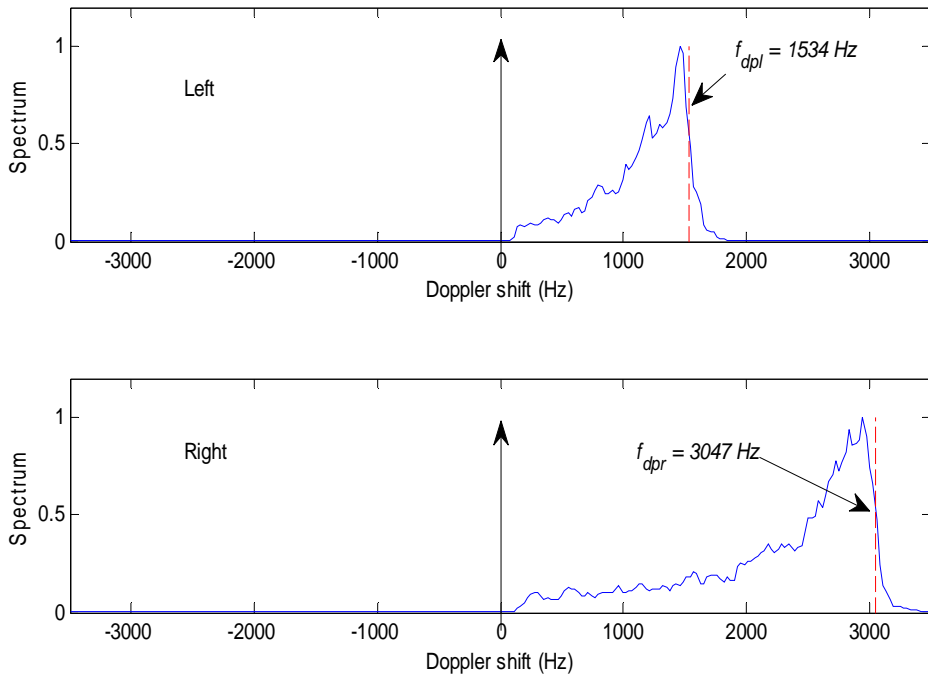

Figure 6.8: Example of spectra obtained during the systole in a phantom experiment with pulsatile flow and $\alpha=21°$. The dashed vertical lines show the detected $f_{d_P l}$ and $f_{d_P r}$.

	G_1	G_2	G_3
Peak Velocity [m/s]	0.47	0.53	0.67
CV [%]	2.9	5.3	31

Table 6.3: Measurements in pulsatile flow conditions

The results obtained on phantom experiments basically confirmed the Field II® simulations outcomes. Figure 6.6 shows a very good agreement between measurements and flowmeter readings, in particular for velocities lower than 0.95m/s. For higher velocities, an increasing underestimation was found. This behaviour could be due to the error that affects the reference velocity. The *Reynold number* (Chapter 1, §1.8.1) for a 0.95m/s flow in a 6mm-diameter pipe is about 2700, which indicates the transition state between laminar and turbulence condition. The profile starts to flatten and the relation $v_{ref} = 2Q/S$, valid for a laminar flow, overestimates the reference peak velocity.

According to *Student's t-test* [47], the measurement error features a physiological Gaussian distribution that confirms the random structure of the sources of noise. From the Gaussian distribution, the probability of the error being within a specific range can be quantified by using mean (μ) and standard deviation (σ). For example, the error of a random measurement has a 95% probability of being within the range $-6 \div +4.4\%$ ($\mu \pm 2\sigma$). The *Bland-Altman analysis* [18] (Figure 6.7, top and bottom panels) confirms that the difference between the Doppler measurements and the flowmeter readings is not dependent on the velocity and the bias is lower than the flowmeter accuracy. Moreover, the limits of agreement are only slightly higher than the flowmeter accuracy, suggesting that the proposed method and flowmeter accuracy are comparable.

A good repeatability of the proposed method is confirmed in pulsatile experiments (see Table 6.3) where a mean CV of 3.8% was observed.

6.4.3. Healthy volunteers

The measurements were grouped for volunteer (V_1, V_2, and V_3) and left/right carotid. The 3 measurements included in each of the 6 groups

were processed for extracting the mean peak velocities and the CVs, which are reported in Table 6.4 together with the heart rate. Figure 6.9 shows, for example, the maximum velocity trend detected in the left carotid of volunteer V_3. In this case, the systolic peak, averaged over the 4 available cycles, was 69cm/s. The SNR of the measured spectra was 19dB.

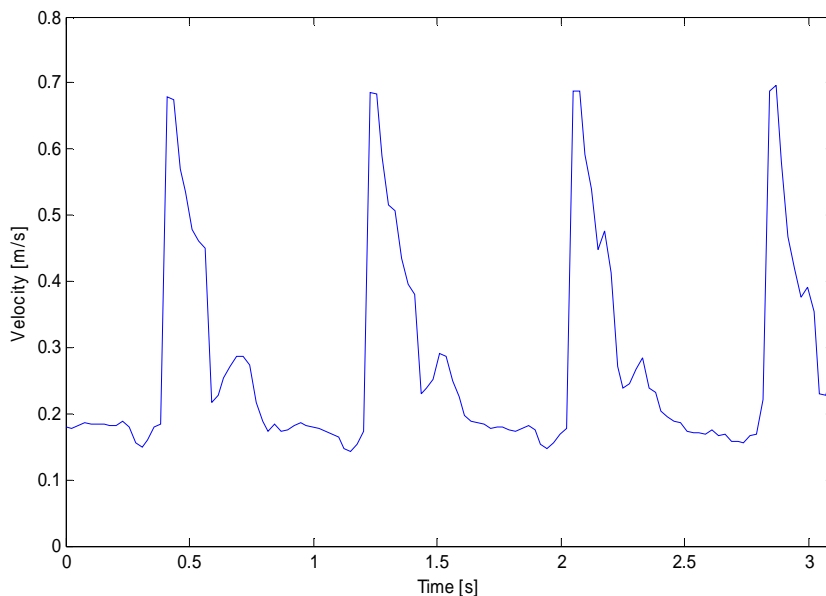|		V_1	V_2	V_3
Peak Velocity [cm/s]	Left	84	120	78
	Right	91	114	86
CV [%]	Left	6.5	2.0	9.9
	Right	5.4	4.2	0.4
Heart rate [bpm]		74	66	73

Table 6.4: Measurements on volunteers.

Figure 6.9: Example of velocity measurement in left carotid artery of volunteer V_3. The systolic peak velocity, averaged over 4 available peaks, is 0.69ms.

Like in pulsatile conditions in phantom experiments, the proposed method shows a good repeatability in tests on volunteers too. Indeed, data collected in Table 6.4 give a mean CV equal to 4.7%.

6.4.4. Anthropomorphic phantom experments

Table 6.5 shows the peak velocity measurements obtained in both the CCA (pump settings P1÷P4) and ICA (pump settings P5÷P7) anthropomorphic phantom experiments. The saved data were elaborated in Matlab® (The MathWorks Inc., Natick, MA) processing each acquisition according to the corresponding method. In particular, for MSD technique the depth along the diameter corresponding to the peak velocity was selected, and the velocity was corrected for the Doppler angle manually estimated in the B-Mode scan. In MGVD method, similarly to MSD, the depth corresponding to the peak velocity was selected, but no angle compensation was needed. Neither depth selection nor angle compensation are required by the MUT. After this process, the time trend of the peak velocity was available for each of the 48+36 experiments. For example, Figure 6.10 shows the peak velocity measured for the 3 methods along 2 cardiac cycles in CCA, considering the P3 pump setting.

		MUT		MSD		MGVD	
		$v_{P_{m_1}}$ [cm/s]	CV_1 [%]	$v_{P_{m_2}}$ [cm/s]	CV_2 [%]	$v_{P_{m_3}}$ [cm/s]	CV_3 [%]
CCA	P1	69	1.7	57	2.9	59	0.4
	P2	85	1.4	72	2.9	75	2.0
	P3	83	0.4	81	0.8	81	0.9
	P4	77	0.4	74	1.2	75	0.3
ICA	P5	63	2.1	52	0.2	63	0.4
	P6	58	1.3	45	0.8	49	0.6
	P7	53	2.5	37	0.7	35	0.4

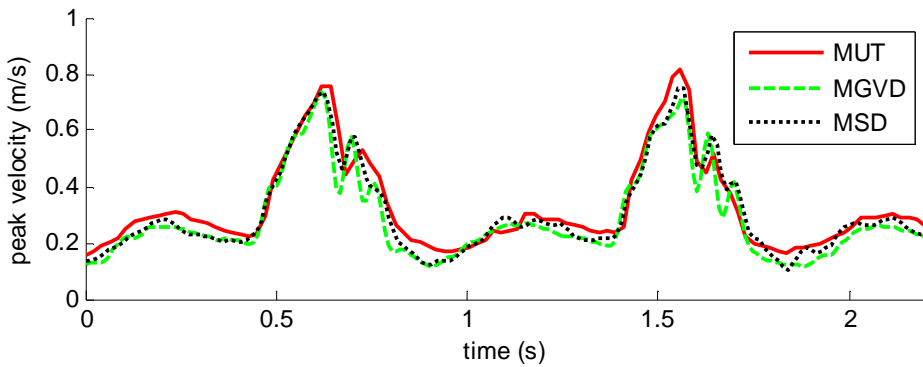Table 6.5: Peak velocity measurements.

Figure 6.10: Comparison between the time trend of peak velocity acquired with the 3 methods (MUT: red continuous; MGVD: green dashed; MSD: black dotted) by investigating the CCA section of the phantom with the P3 pump setting (see Table 6.2).

The peak velocity trends obtained for the 3 methods were further processed by detecting and averaging the systolic peaks. This produced a single measurement from each of the 48+36 experiments. The 4 measurements referring to the same pump setting and method were averaged. The results are reported in the columns of Table 6.5 as $v_{P_{m_1}}$, $v_{P_{m_2}}$, and $v_{P_{m_3}}$, for the 3 methods MUT, MSD, MGVD, respectively. The top 4 rows refers to acquisitions in CCA (P1÷P4), the bottom 3 rows list the measurements from ICA (P5÷P7). The mean peak velocities measured by MUT ($v_{P_{m_1}}$) are higher than the corresponding values measured by MSD and MGVD ($v_{P_{m_2}}$ and $v_{P_{m_3}}$, respectively) in all of the tested pump conditions (P1÷P7), as reported in Table 6.5.

The 4 measurements referring to the same pump setting and method were further analyzed for repeatability by calculating the coefficient of variation (CV), i.e. the standard deviation of the 4 measurements normalized with respect to their average. The calculated CVs are reported in Table 6.5 (CV_1, CV_2, CV_3) on the right of the corresponding mean velocities. The new method features a good repeatability as demonstrated by the CVs, which are always lower than 3% with an average of 1.4%. Moreover, the CVs measured for MUT are similar to those obtained by MSD and MGVD methods in the same conditions, which are 1.3% and 0.7% in average, respectively.

127

The accuracy was evaluated by considering, for each pump setting, the difference between the measurement and the reference velocity, normalized with respect to the reference. The reference velocity was calculated as the average of the measurements obtained with the already validated methods, i.e. MSD and MGVD. The results are reported in Table 6.6, where MSD and MGVD feature anti-symmetric errors due to the method used for reference calculation.

		MUT	**MSD**	**MGVD**
CCA	P1	+19.0%	−1.9%	+1.9%
	P2	+15.7%	−2.0%	+2.0%
	P3	+03.1%	−0.9%	+0.9%
	P4	+02.7%	+0.4%	−0.4%
	TOT	+10.1%	−1.1%	+1.1%
ICA	P5	+10.0%	−9.1%	+9.1%
	P6	+22.6%	−3.1%	+3.1%
	P7	+45.5%	+2.9%	−2.9%
	TOT	+26.0%	−3.1%	+3.1%

Table 6.6: Peak velocity measurements errors

The overestimation produced by MUT is confirmed by the errors detailed in Table 6.7. In particular a 45% overestimation is found in ICA. This can be explained by the presence of complex flow configurations, like possible helical flow trajectories [48], which are included in the large sample volume used by MUT.

		MUT vs. MSD	**MUT vs. MGVD**	**MGVD vs. MSD**
CCA	μ	+9.3cm/s	+6.5cm/s	+3.0cm/s
	σ	+6.5cm/s	+4.0cm/s	+3.4cm/s
	$\mu - 1.96 \cdot \sigma$	−3.4cm/s	−1.4cm/s	−3.7cm/s
	$\mu + 1.96 \cdot \sigma$	+22.1cm/s	+14.4cm/s	+9.6cm/s
ICA	μ	+12.9cm/s	+9.1cm/s	+3.8cm/s
	σ	+2.3cm/s	+8.5cm/s	+6.3cm/s
	$\mu - 1.96 \cdot \sigma$	+8.4cm/s	−7.6cm/s	−8.7cm/s
	$\mu + 1.96 \cdot \sigma$	+17.4cm/s	+25.8cm/s	+16.3cm/s

Table 6.7: Limits of agreement.

The 3 methods (MUT, MSD, MGVD) were finally compared in pairs, extracting the difference of the measured peak velocities for each pump setting and method couple. The mean μ and standard deviation σ of the differences were calculated and reported in Table 6.7 together with the limits of agreements ($\mu \pm 1.96 \cdot \sigma$). The results are distinguished for CCA and ICA (top and bottom rows, respectively).

The tests proved that the proposed method features good repeatability in all of the tested experimental conditions, good accuracy in CCA but a high overestimation in ICA. This is probably due to the interference of complex flow included in the large sample volume provided by the proposed method.

Contributions

Journal Papers

S. Ricci, R. Matera, P. Tortoli, "An Improved Doppler Model for Obtaining Accurate Maximum Blood Velocities", Elsevier, Ultrasonics, Vol. 54, n° 7, pp. 2006-2014, 2014

S. Ricci, D. Vilkomerson, R. Matera, P. Tortoli, "Accurate Blood Peak Velocity Estimation Using Spectral Models and Vector Doppler", IEEE TUFFC, Vol. 62, n° 4, pp. 686-696, April 2015

Conference Proceedings

S. Ricci, R. Matera, A. Dallai, "Amplitude And Phase Estimator for Real-Time Biomedical Spectral Doppler Applications", Acoustics, Speech and Signal Processing (ICASSP), 2014 IEEE International Conference, pp 5149-5152

S. Ricci, R. Matera, P. Tortoli, "Real Time BAPES Implementation for Fast Spectral Doppler Estimation", Ultrasonic Symposium (IUS), 2013 IEEE International, 2013, pp. 899-902

S. Ricci, R. Matera, "A Doppler Spectrum Model For Improved Ultrasound Assessment of Maximum Velocity In Blood Flow", 7th World Congress of Biomechanics (WCB2014), Boston, USA, Luglio 2014

S. Ricci, M. Cinthio, M. Lenge, R. Matera, J. Albinsson, P. Tortoli, "Volume Flow Assessment through Simultaneous B-Mode and Multigate Doppler", Ultrasonic Symposium (IUS), 2012 IEEE International, 2012, pp. 1588-1591

S. Ricci, D. Vilkomerson, R. Matera, P. Tortoli, "An Improved Method of Determining Peak Blood Velocity", Ultrasonic Symposium (IUS), 2014 IEEE International, 2014, pp. 2245-2248

E. Boni, L Bassi, A. Dallai, G. Giannini, F. Guidi, V. Meacci, R. Matera, A. Ramalli, M. Scaringella,J. Viti, S. Ricci, P. Tortoli, "ULA-OP 256: a Portable High Performance Research Scanner", Ultrasonic Symposium (IUS), 2015 IEEE International, 2015

R. Matera, S. Ricci, A.C.H. Yu, B.Y.S. Yiu, P. Tortoli, "Validation of a Novel Vector Method for Blood Peak Velocity Detection in an Anthropomorphic Phantom", Ultrasonic Symposium (IUS), 2015 IEEE International, 2015

Bibliography

[1] D. Evans and W. McDicken, Doppler Ultrasound: Physics, Instrumentation and Signal Processing, Chichester: Wiley, 2000.

[2] K. Shapoori, J. Sadler, E. Malyarenko, F. Seviaryn, E. Boni, A. Ramalli, P. Tortoli and R. G. Maev, "Adaptive beamforming for ultrasonic phased array focusing through layered," in *IEEE Ultrasonics Symposium (IUS)*, San Diego, California, USA, 2010.

[3] K. Shapoori, J. Sadler, E. Malyarenko, F. Seviaryn, E. Maeva, E. Boni, A. Ramalli, P. Tortoli and R. G. Maev, "Transmission mode adaptvie beamforming through a human skull," *Acoustical Imaging,* vol. 31, 2011.

[4] A. Steinman, J. Tavakkoli, J. Myers, R. Cobbold and K. Johnston, "Sources of Error in Maximum Velocity Estimation Using Linear Phased-Array Doppler Systems with Steady Flow," *Ultrasound Med. Biol.,* vol. 27, no. 5, pp. 655-664, 2001.

[5] E. Boni, L. Bassi, A. Dallai, F. Guidi, A. Ramalli, S. Ricci, J. Housden and P. Tortoli, "A Reconfigurable and Programmable FPGA-based System for Nonstandard Ultrasound Methods," *IEEE Trans. Ultrason. Ferroelectr. Freq. Control,* vol. 59, no. 7, pp. 1378-1385, 2012.

[6] P. Tortoli, L. Bassi, E. Boni, A. Dallai, F. Guidi and S. Ricci, "ULA-OP: An Advanced Open Platform for ULtrasound Research," *IEEE Trans. Ultrason. Ferroelectr. Freq. Control,* vol. 56, no. 10, p. 2207–2216, 2009.

[7] A. Ramalli, Development of Novel Ultrasound Techniques for Imaging and Elastography : From Simulation to Real-Time Implementation, Firenze: Firenze University Press, 2013.

[8] J. Jensen and N. Svendsen, "Calculation of Pressure Fields from

Arbitrarily Shaped, Apodized, and Excited Ultrasound Transducers," *IEEE Trans. Ultrason. Ferroelectr. Freq. Control,* vol. 39, no. 2, p. 262–267, 1992.

[9]   J. Jensen, "Field: A Program for Simulating Ultrasound Systems," *Med. Biol. Eng. Comput.,* Vols. 34, Suppl. 1, pt. 1, p. 351–353, 1996.

[10] J. Doucette, P. Corl, H. Payne and al., "Validation of a Doppler Guide Wire for Intravascular Measurement of Coronary Artery Flow Velocity," *Circulation,* vol. 85, no. 5, p. 1899–1911, 1992.

[11] J. Womersley, "An Elastic Tube Theory of Pulse Transmission and Oscillatory Flow in Mammalian Arteries," WADC-TR-56-614, Wright Air Development Center, 1957.

[12] C. Leguy, E. Bosboom, A. Hoeks and F. v. d. Vosse, "Model-based Assessment of Dynamic Arterial Blood Volume Flow from Ultrasound Measurements," *Med. Biol. Eng. Comput.,* vol. 47, p. 641–648, 2009.

[13] R. Krams, G. Bambi, F. Guidi, F. Helderman, A. V. D. Steen and P. Tortoli, "Effect of Vessel Curvature on Doppler Derived Velocity Profiles and Fluid Flow," *Ultrasound in Medicine and Biology,* vol. 31, no. 5, pp. 663-671, 2005.

[14] S. Ricci, M. Cinthio, L. Francalanci and P. Tortoli, "Volumetric Blood Flow Assessment through Multigate Spectral Doppler," in *IEEE Ultrasonics Symposium (IUS), pp.570-573*, Roma, Italy, 2009.

[15] S. Ricci, E. Boni, F. Guidi, T. Morganti and P. Tortoli, "A Programmable Real-Time System for Development and Test of New Ultrasound investigation Methods," *IEEE Trans. Ultrason., Ferroelect., Freq. Contr., Special Issue,* vol. 53, no. 10, pp. pp 1813-1819, 2006.

[16] A. Eriksson, H. Persson and K. Lindström, "A computer-controlled Arbitrary Flow Waveform Generator for Physiological Studies,"

Review of Scientific Instruments, vol. 71, no. 1, pp. 235-242, 2000.

[17] K. Ramnarine, D. Nassiri, P. Hoskins and J. Lubbers, "Validation of a New Blood-mimicking Fluid for Use in Doppler Flow Test Objects," *Ultras. in Med. & Biol,* vol. 24, no. 3, pp. 451-459, 1998.

[18] J. Bland and D. Altman, "Statistical Methods for Assessing Agreement Between Two Methods of Clinical Measurement," *The Lancet,* vol. 1, pp. 307-310, 1986.

[19] B. S. I. (BSI), "Precision of Test Methods, Guide for the Determination of Repeatability and Reproducibility for a Standard Test Method by Inter-laboratory Tests," 1979.

[20] P. Welch, "The use of fast Fourier transform for the estimation of power spectra: A Method Based on Time Averaging Over Short, Modified Periodograms," *IEEE Trans. Audio Electroacoust.,* vol. 15, no. 2, p. 70–73, 1967.

[21] J. Li and P. Stoica, "An Adaptive Filtering Approach to Spectral Estimation and SAR Imaging," *IEEE Trans. Signal Processing,* vol. 44, no. 6, pp. 1469-1484, 1996.

[22] Z. Liu, L.Hongbin and L. Jian, "Efficient Implementation of Capon and APES for Spectral Estimation," *IEEE Trans. on Aerospace and Electronic Systems,* vol. 34, no. 4, p. 1314 – 1319, 1998.

[23] F. Gran, A. Jakobsson and J. Jensen, "Adaptive Spectral Doppler Estimation," *IEEE Trans. Ultrason., Ferroelect., Freq. Contr.,* vol. 56, no. 4, p. 700–713, 2009.

[24] datasheet, "TMS320C6455 Fixed-Point Digital Signal Processor," *http://focus.ti.com/lit/ds/symlink/tms320c6455.pdf.*

[25] M. Ylinen, A. Burian and J. Takala, "Direct Versus Iterative Methods for Fixed-point Implementation of Matrix Inversion," *Proceedings of the 2004 International Symposium on Circuits and Systems (ISCAS),*

vol. 3, pp. 225-228, 2004.

[26] V. Pan and R. Schreiber, "An Improved Newton Iteration for the Generalized Inverse of a Matrix, with Applications," *SIAM J. Sci. and Stat. Comput.,* vol. 12, no. 5, p. 1109–1130, 1991.

[27] W. Press, B. Flannery, S. Teukolsky, W.T. and Vetterling, Numerical Recipes in C: The Art of Scientific Computing, Cambridge: Cambridge University Press, 1992.

[28] E. Grant, C. Benson, G. Moneta, A. Alexandrov, J. Baker, E. Bluth and al., "Carotid Artery Stenosis: Gray-Scale and Doppler US Diagnosis," *Radiology,* vol. 229, no. 2, pp. 340-346, 2003.

[29] P. Tortoli, G. Guidi and V. Newhouse, "Improved Blood Velocity Estimation Using the Maximum Doppler Frequency," *Ultrasound Med. Biol.,* vol. 21, no. 4, p. 527–532, 1995.

[30] M. Bakircioglu and B. Ramamurthy, "Automatic Optimization Methods and Systems for Doppler Ultrasound Imaging," *U.S. Patent 6 733 454,* 11 May 2004.

[31] J. Bang and C. Kim, "Ultrasound Diagnostic Apparatus and Method for Measuring Blood Flow Velocity Using Doppler Effect," *U.S. Patent 6 530 890,* 11 March 2003.

[32] K. Marasek and A. Nowicki, "Comparison of the Performance of Three Maximum Doppler Frequency Estimators Coupled With Different Spectral Estimation Methods," *Ultrasound Med. Biol.,* vol. 20, no. 7, p. 629–638, 1994.

[33] A. Papoulis, The Fourier Integral and Its Applications, New York, NY: McGraw-Hill, 1962, p. 20.

[34] L. Mo and R. Cobbold, "A Nonstationary Signal Simulation Model for Continuous Wave and Pulsed Doppler Ultrasound," *IEEE Trans. Ultrason. Ferroelectr. Freq. Control,* vol. 36, no. 5, p. 522–530,

1989.

[35] D. Vilkomerson, T. Chilipka and P. Domagala, "Easy-to-use, Low-cost Blood Velocity Measurement," *Proceedings IEEE 28th Annu. Northeast Bioengineering Conf.,* p. 255–256, 2002.

[36] S. Ricci, S. Diciotti, L. Francalanci and P. Tortoli, "Accuracy and Reproducibility of a Novel Dual-beam Vector Doppler Method," *Ultrasound Med. Biol.,* vol. 35, no. 5, p. 829–838, 2009.

[37] F. Glor, Q. Long, A. Hughes and al., "Reproducibility Study of Magnetic Resonance Image-based Computational Fluid Ddynamics Prediction of Carotid Bifurcation Flow," *Ann. Biomed. Eng.,* vol. 31, no. 2, pp. 142-151, 2003.

[38] C. Kerber and C. Heilman, "Flow Dynamics in the Human Carotid Artery: I. Preliminary Observations Using a Transparent Elastic Model," *AJNR Am J Neuroradiol,* 1992.

[39] C. Bastos, P. Fish, R.Steel and F. Vaza, "Doppler Power Spectrum from a Gaussian Sample Volume," *Ultrasonics,* vol. 37, no. 9, p. 623–632, 2000.

[40] J. Pearson and P. Tardy, "Models for Flow of Non-Newtonian and Complex Fluids Through Porous Media," *J. Non-Newton. Fluid,* vol. 102, no. 2, pp. 447-473, 2002.

[41] R. Hoskins, "A Comparison of Single- and Dual-beam Methods for Maximum Velocity Estimation," *Ultrasound Med. Biol.,* vol. 25, no. 4, p. 583–592, 1999.

[42] M. Fox, "Multiple Crossed-beam Ultrasound Doppler Velocimetry," *IEEE Trans. Sonics Ultrason.,* vol. 25, no. 5, p. 281–286, 1978.

[43] S. Ricci, L. Bassi and P. Tortoli, "Real Time Vector Velocity Imaging through Multigate Doppler and Plane Waves," *IEEE Trans. Ultrason. Ferroelectr. Freq. Contr.,* vol. 62, no. 2, pp. 314-324, 2014.

[44] S. Ricci, R. Matera and P. Tortoli, "An Improved Doppler Model for Obtaining Accurate Maximum Blood Velocities," *Ultrasonics,* vol. 54, no. 7, p. 2006–2014, 2014.

[45] S. Ricci, L. Bassi, E. Boni, A. Dallai and P. Tortoli, "Multichannel FPGA-based Arbitrary Waveform Generator for Medical Ultrasound," *Electron. Lett.,* vol. 43, no. 24, p. 1335–1336, 2007.

[46] S. Lai, B. Yiu, A. Poon and A. Yu, "Design of Anthropomorphic Flow Phantoms Based on Rapid Prototyping of Compliant Vessel Geometries," *Ultrasound Med. Biol.,* vol. 39, no. 9, p. 1654–1664, 2013.

[47] R. Mankiewicz, The Story of Mathematics, Princeton, NJ: Princeton University Press, 2004, p. p. 158.

[48] S. Kefayati, D. Holdsworth and T. Poepping, "Turbulence Intensity Measurements Using Particle Image Velocimetry in Diseased Carotid Artery Models: Effect of Stenosis Severity, Plaque," *J. Biomech.,* vol. 47, no. 1, p. 253–263, 2014.